

# **Gamma-Gamma Angular Correlation Measurements With GRIFFIN**

by

**Andrew Dale MacLean**

A Thesis

Presented to

The University of Guelph

In partial fulfilment of requirements

for the degree of

Masters of Science

in

Physics

Guelph, Ontario, Canada

©Andrew Dale MacLean, March, 2016

## ABSTRACT

### Gamma-Gamma Angular Correlation Measurements With GRIFFIN

Andrew Dale MacLean  
University of Guelph, 2016

Advisor:  
Professor Carl E. Svensson

When an excited nuclear state emits successive  $\gamma$ -rays in a  $\gamma - \gamma$  cascade, an anisotropy is generally found in the spatial distribution of the second  $\gamma$ -ray,  $\gamma_2$ , with respect to the first,  $\gamma_1$ . By defining the direction of  $\gamma_1$  to be the z-axis, the intermediate level, in general will have an uneven distribution of m-states. This causes an anisotropy in the angular correlation of the second  $\gamma$ -ray with respect to the first.

Angular correlation measurements can be used for the assignment of spins and parities to the nuclear states, and thus provide a powerful means to elucidate the structure of nuclei away from stability through  $\beta - \gamma - \gamma$  coincidence measurements. In order to explore the sensitivity of the new 16 high-purity germanium (HPGe) clover-detector Gamma-Ray Infrastructure For Fundamental Investigations of Nuclei (GRIFFIN) at TRIUMF-ISAC, a series of measurements were taken to establish a methodology for such  $\gamma - \gamma$  angular correlations.

The first case studied to test the performance of GRIFFIN for these measurements was the well-known  $4^+ \rightarrow 2^+ \rightarrow 0^+$   $\gamma - \gamma$  cascade from  $^{60}\text{Co}$   $\beta^-$  decay. Geant4 simulated experiments and experimental source data were collected and analyzed as the primary test of GRIFFIN. The next case studied was a  $^{66}\text{Ga}$  beam implanted in the centre of the array. With  $^{66}\text{Ga}$ , three cascades were examined to analyze the  $\gamma - \gamma$  angular correlations. The first angular correlation being a  $2^+ \rightarrow 2^+ \rightarrow 0^+$  cascade of 833-1039 keV  $\gamma$ -rays with a known mixing ratio of  $\delta = -1.9(3)$ . Next was a known  $0^+ \rightarrow 2^+ \rightarrow 0^+$  cascade with the  $\gamma$ -ray energies in

coincidence being 1333-1039 *keV*. The final correlation for this nucleus was a  $1^+ \rightarrow 2^+ \rightarrow 0^+$  cascade of 2752-1039 *keV*  $\gamma$ -rays with a mixing ratio of -0.12(2). The next nucleus studied was the  $\beta^+$  decay of  $^{62}\text{Ga}$ , which is a superallowed Fermi  $\beta$  emitter. This nucleus was a first attempt to discern a recently challenged spin assignment to the 2.34 *MeV* excited state. The labelling of this state as a  $2^+$  or a  $0^+$  has effects on the isospin symmetry breaking correction factor used for calculating  $\mathcal{F}t$  values.

For the  $^{60}\text{Co}$  measurements the spin assignments were fully consistent with a  $4^+ \rightarrow 2^+ \rightarrow 0^+$  cascade, but due to the similarity of the  $2^+ \rightarrow 2^+ \rightarrow 0^+$  with a mixing ratio of  $\delta = 0.18(1)$  which gives a nearly identical angular correlation and was indistinguishable. Also in  $^{66}\text{Ga}$  decay, the precision of the mixing ratio for the  $2^+ \rightarrow 2^+ \rightarrow 0^+$  cascade involving the 833-1039 *keV*  $\gamma$ -rays was improved giving a value of  $\delta = -2.1(2)$ . Finally, the mixing ratio for the  $1^+ \rightarrow 2^+ \rightarrow 0^+$  cascade involving the 2752-1039 *keV*  $\gamma$ -rays was determined to be  $\delta = -0.08(3)$ . This measurement was completed without realizing the value was known and is in complete agreement with the previous measurement. In the  $^{62}\text{Ga}$  measurement the assignment of the spin of the 2.34 *MeV* excited state was unable to be discerned due to reduced statistics from a faulty extraction electrode. The measurement seemed to favour the assignment as a  $0^+$  state but additional statistics are required for a definitive assignment.

# Acknowledgements

Firstly, I would like to thank my supervisor Carl Svensson. The opportunity to contribute to the high-quality research has been a great experience and it would not have been possible without the amazing personalities involved. Your continual strive for knowledge and ability to clarify concepts has inspired me to develop my capacity as a scientist. I would also like to give a special thanks to Paul Garrett, with a fundamental comprehension in so many areas you have educated me to appreciate the importance of even the smallest technical details.

To all of the fellow post-docs, graduate and undergraduate students I appreciate you all for your kindness and words of wisdom along the way. With your friendship I always felt welcomed like I was home. Thank you for the great memories we have shared so far, I know many more will come in the future.

For the many collaborators in the GRIFFIN collaboration that have assisted in this work I would like to offer my thanks. Without your constant cooperation and assistance this work would not have been accomplished as easily.

Finally, I would like to thank my family. With your love and support you have given me the opportunity to strive for further education and become the person I am today. To my parents, thank you for your kind words and for always being an ear when I needed you. To my sister, thanks for always being able to make me smile no matter what mood I am in, “A



is for...”. I love you all.

# Contents

<b>Acknowledgements</b>	<b>iv</b>
<b>1 Introduction</b>	<b>1</b>
1.1 Nuclear Structure and the Shell Model . . . . .	1
1.2 Radioactive Decay . . . . .	7
1.2.1 Radioactive Decay Law . . . . .	9
1.3 Theory of $\gamma$ Decay . . . . .	10
1.4 Weisskopf Estimates . . . . .	16
1.5 Mixing Ratios . . . . .	17
1.6 Angular Correlations . . . . .	18
1.7 Experimental Angular Correlation Measurements and Spin Assignments . . .	26
1.7.1 Direct Correlation Coefficient Measurements . . . . .	27
1.7.2 Ellipse Comparisons . . . . .	28
1.7.3 Goodness-Of-Fit vs. Mixing Ratio . . . . .	29
1.8 Methodology for Spin Assignments Via Angular Correlations Measurements	
With GRIFFIN . . . . .	30
<b>2 Experiment</b>	<b>33</b>

2.1	TRIUMF . . . . .	33
2.1.1	ISAC . . . . .	33
2.2	Gamma-Ray Interactions in Germanium Detectors . . . . .	35
2.2.1	Photoelectric Absorption . . . . .	37
2.2.2	Compton Scattering . . . . .	38
2.2.3	Pair Production . . . . .	40
2.2.4	Semiconductor Diode Detectors . . . . .	41
2.3	The GRIFFIN Spectrometer . . . . .	44
2.3.1	Angular Properties of GRIFFIN . . . . .	48
2.3.2	Auxiliary Detectors . . . . .	51
<b>3</b>	<b>Analysis</b>	<b>55</b>
3.1	Simulations and Data Corrections . . . . .	55
3.1.1	Generating GRIFFIN Maps . . . . .	56
3.1.2	Angular Correlation Simulation Package . . . . .	58
3.1.3	Crystal Efficiency and Corrections . . . . .	60
3.1.4	Background Subtractions . . . . .	63
3.1.5	Event Mixing Technique . . . . .	66
3.1.6	Angular Correlations and Templates . . . . .	68
3.1.7	Cobalt-60 Simulations . . . . .	70
3.1.8	Addback . . . . .	77
3.1.9	Spin Assignments . . . . .	80
3.2	Experimental Data . . . . .	83
3.2.1	Gain Matching . . . . .	84

3.2.2	$^{60}\text{Co}$ Source Data . . . . .	86
3.2.3	$^{66}\text{Ga}$ Source Data . . . . .	90
3.2.4	$^{62}\text{Ga}$ Data . . . . .	101
<b>4</b>	<b>Conclusions</b>	<b>113</b>
4.1	Future Work . . . . .	115
	<b>Bibliography</b>	<b>117</b>

# List of Tables

1.1	Magic numbers for a spherical harmonic oscillator potential . . . . .	4
1.2	Dipole and quadrupole directional dependences according to m-state population.	19
1.3	Table of the first five Legendre polynomials. . . . .	21
1.4	Theoretical coefficients of cascades with different values of nuclear spins . . .	25
2.1	Angular positions of the GRIFFIN array . . . . .	48
2.2	The 52 unique opening angles between HPGe crystals in the GRIFFIN geometry	49
2.3	Angles in GRIFFIN geometry after grouping and folding . . . . .	50
3.1	Comparison of theoretical to simulated coefficients with Geant4 simulation .	59
3.2	Tables of sources and energies used to find the efficiencies of GRIFFIN . . .	61
3.3	Limit on counts in the 2342 <i>keV</i> transition in $^{62}\text{Ga}$ as a function of the assumed centroid position. . . . .	106

# List of Figures

1.1	Ionization energies of neutral atoms of the elements. . . . .	2
1.2	Two neutron and two proton separation energies . . . . .	3
1.3	A plot of the Wood-Saxon potential and the spin-orbit coupling . . . . .	5
1.4	Single particle energy levels for the harmonic oscillator and Wood-Saxon potentials with spin-orbit . . . . .	6
1.5	The chart of nuclides . . . . .	7
1.6	Representation of an excited state $\gamma$ decay to a lower energy state . . . . .	12
1.7	Anisotropic distributions for single m-states and sum of all m-states . . . . .	19
1.8	Possible transitions for a $0 \rightarrow 2 \rightarrow 0$ cascade . . . . .	20
1.9	Angular correlations for a variety of nuclear cascades . . . . .	26
1.10	The angular correlation for the 1182.5 keV and 986.1 keV transitions in $^{93}\text{Sr}$ . . . . .	27
1.11	Theoretical $a_2$ versus $a_4$ ellipses for a variety of cascades . . . . .	28
1.12	Chi squared values for an experimentally measured $\gamma$ ray cascade . . . . .	30
1.13	Angular correlation template for the $4^+ \rightarrow 2^+ \rightarrow 0^+$ cascade in $^{60}\text{Co}$ decay . . . . .	31
2.1	Layout of the ISAC facility at TRIUMF . . . . .	34
2.2	A comparison of CdTe, HPGe and NaI detectors used for $\gamma$ -ray spectroscopy . . . . .	36
2.3	Plot of $\gamma$ -ray linear attenuation coefficients . . . . .	37

2.4	Schematic of Compton scattering . . . . .	39
2.5	Schematic of pair-production . . . . .	40
2.6	Band structure for conducting, semiconducting and insulating materials. . .	42
2.7	Band structure for semiconducting materials . . . . .	43
2.8	Image of the GRIFFIN spectrometer . . . . .	45
2.9	A Geant4 simulated image of GRIFFIN detectors with detector faces visible.	45
2.10	Image of the four crystals in each GRIFFIN detector . . . . .	46
2.11	Simulated efficiencies of GRIFFIN using Geant4 . . . . .	47
2.12	Image of half of the SCEPTAR array . . . . .	51
2.13	Image of the DESCANT array . . . . .	52
2.14	Image of the Zero degree scintillator . . . . .	53
2.15	Image of the PACES array . . . . .	54
3.1	Energy dependence of GRIFFIN opening angles . . . . .	57
3.2	Theta distribution for 200 <i>keV</i> $\gamma$ -rays in GRIFFIN . . . . .	58
3.3	Simulated $4^+ \rightarrow 2^+ \rightarrow 0^+$ angular correlation . . . . .	59
3.4	Absolute efficiency plot for GRIFFIN . . . . .	62
3.5	Absolutely efficiency of each crystal in GRIFFIN for $^{60}\text{Co}$ $\gamma$ -rays . . . . .	63
3.6	Efficiency corrections for all 51 angles in the GRIFFIN geometry . . . . .	64
3.7	Efficiency correction for grouped and folded angles in GRFFIN . . . . .	64
3.8	Plot of photopeak and Compton background gates . . . . .	65
3.9	Plot of coincidence and background timing gates . . . . .	66
3.10	Theoretical $a_2$ and $a_4$ as a function of the mixing ratio, $\delta$ , for a $2^+ \rightarrow 2^+ \rightarrow 0^+$	69
3.11	Plot of $a_2$ against $a_4$ for a $2^+ \rightarrow 2^+ \rightarrow 0^+$ cascade . . . . .	70

3.12	Example decay of $^{60}\text{Co}$ to $^{60}\text{Ni}$ . . . . .	71
3.13	$\gamma$ -ray spectrum measured with individual GRIFFIN crystals with $^{60}\text{Co}$ . . .	71
3.14	$\gamma$ - $\gamma$ coincidence matrix for $^{60}\text{Co}$ with GRIFFIN in single crystal mode . . . .	72
3.15	3D $\gamma$ - $\gamma$ matrix with the z-axis being the opening angles . . . . .	73
3.16	$\gamma$ -ray spectrum gated on the 1.33 <i>MeV</i> $\gamma$ -ray in $^{60}\text{Co}$ decay . . . . .	74
3.17	Angular correlation of the $4^+ \rightarrow 2^+ \rightarrow 0^+$ cascade in $^{60}\text{Co}$ . . . . .	74
3.18	Folded angular correlation of the $4^+ \rightarrow 2^+ \rightarrow 0^+$ cascade in $^{60}\text{Co}$ . . . . .	75
3.19	Template for a hypothetical $2^+ \rightarrow 2^+ \rightarrow 0^+$ cascade in $^{60}\text{Co}$ decay with $\delta = -10$	76
3.20	Template for a hypothetical $2^+ \rightarrow 2^+ \rightarrow 0^+$ cascade in $^{60}\text{Co}$ decay with $\delta = 0.2$	76
3.21	Template for a hypothetical $2^+ \rightarrow 2^+ \rightarrow 0^+$ cascade in $^{60}\text{Co}$ decay with $\delta = 1$	77
3.22	$\gamma$ -ray spectrum from $^{60}\text{Co}$ decay . . . . .	78
3.23	1332 <i>keV</i> photopeak for addback and single crystal methods . . . . .	79
3.24	Experimental $\gamma$ - $\gamma$ coincidence matrix for $^{60}\text{Co}$ decay with clover addback . .	79
3.25	3D histogram using clover addback . . . . .	80
3.26	Angular correlation using single crystal method . . . . .	81
3.27	Angular correlation using clover addback method . . . . .	82
3.28	$\chi^2/\nu$ versus $\text{atan}(\delta)$ with Geant4 simulation data . . . . .	83
3.29	$^{60}\text{Co}$ data not gain matched . . . . .	85
3.30	$^{60}\text{Co}$ data gain matched . . . . .	85
3.31	$\gamma$ -ray spectrum for a $^{60}\text{Co}$ source inside GRIFFIN. . . . .	86
3.32	$\gamma$ - $\gamma$ matrix for a $^{60}\text{Co}$ source inside GRIFFIN. . . . .	87
3.33	Background and uncorrelated mixed event spectrum for $^{60}\text{Co}$ . . . . .	88
3.34	Angular correlation from the event-mixed data . . . . .	88
3.35	Angular correlations for $^{60}\text{Co}$ . . . . .	89



3.36 $\chi^2/\nu$ versus $\text{atan}(\delta)$ for experimental $^{60}\text{Co}$ data . . . . .	90
3.37 Image of levels studied in the decay of $^{66}\text{Ga}$ to $^{66}\text{Zn}$ . . . . .	91
3.38 $\gamma$ -ray spectrum from $^{66}\text{Ga}$ decay . . . . .	92
3.39 $\gamma - \gamma$ matrix for $^{66}\text{Ga}$ decay . . . . .	93
3.40 Projection of the $^{66}\text{Ga}$ $\gamma - \gamma$ matrix gated on the 833 <i>keV</i> photopeak. . . .	94
3.41 Angular correlation measured for the 833-1039 <i>keV</i> $\gamma - \gamma$ cascade . . . . .	94
3.42 $\chi^2/\nu$ versus $\text{atan}(\delta)$ for 833-1039 <i>keV</i> cascade in $^{66}\text{Ga}$ . . . . .	95
3.43 $^{66}\text{Ga}$ $\gamma - \gamma$ matrix gated on the 1333 <i>keV</i> photopeak . . . . .	95
3.44 Angular correlation for the 1333-1039 <i>keV</i> cascade in $^{66}\text{Zn}$ . . . . .	96
3.45 $\chi^2/\nu$ versus $\text{atan}(\delta)$ for the 1333-1039 <i>keV</i> cascade in $^{66}\text{Zn}$ . . . . .	97
3.46 $^{66}\text{Ga}$ $\gamma - \gamma$ matrix gated on the 2752 <i>keV</i> photopeak . . . . .	98
3.47 Angular correlation for the 2752-1039 <i>keV</i> cascade . . . . .	98
3.48 $\chi^2/\nu$ versus $\text{atan}(\delta)$ for 2752-1039 <i>keV</i> cascade in $^{66}\text{Ga}$ . . . . .	99
3.49 3791 <i>keV</i> transition in $^{66}\text{Zn}$ decay . . . . .	100
3.50 Level scheme of $^{62}\text{Zn}$ populated by the $\beta$ decay of $^{62}\text{Ga}$ . . . . .	102
3.51 Comparison of $^{62}\text{Ga}$ spectra collected with the $8\pi$ and GRIFFIN . . . . .	104
3.52 $\beta - \gamma$ spectrum for $^{62}\text{Ga}$ decay . . . . .	105
3.53 Fit to a 2342.2 <i>keV</i> peak in $^{62}\text{Ga}$ decay . . . . .	105
3.54 Angular correlation using all angles for the 1388-954 <i>keV</i> cascade in $^{62}\text{Zn}$ . .	107
3.55 Angular correlation for the 1388-954 <i>keV</i> cascade in $^{62}\text{Zn}$ with angles grouped	108
3.56 Angular correlation for the 1388-954 <i>keV</i> cascade in $^{62}\text{Zn}$ folded and grouped	109
3.57 $\chi^2/\nu$ vs $\text{atan}(\delta)$ for the 1388-954 <i>keV</i> cascade in $^{62}\text{Zn}$ decay with 51 angles .	109
3.58 $\chi^2/\nu$ vs $\text{atan}(\delta)$ for the 1388-954 <i>keV</i> cascade in $^{62}\text{Ga}$ decay with 20 angles .	110
3.59 $\chi^2/\nu$ vs $\text{atan}(\delta)$ for the 1388-954 <i>keV</i> cascade in $^{62}\text{Ga}$ decay with 11 angles .	110

3.60 $\chi^2/\nu$ versus number of simulated events for the $^{62}\text{Ga}$ decay . . . . .	111
--	-----

# Chapter 1

## Introduction

### 1.1 Nuclear Structure and the Shell Model

In order to comprehend many characteristics observed in nuclear structure, models are used to describe experimental phenomena. One of the models is the nuclear shell model, which is used to describe individual nucleon motion in an average one-body potential that is produced by all the other nucleons in the nucleus [1]. The shell model is among the most successful models and is used extensively in many areas of nuclear physics. Making a comparison to atomic physics, electrons in quantized energy levels are bound in the field of the nucleus. Electrons interact with the protons via the Coulomb field and, if they have a low enough kinetic energy, they are in a bound state. The ionization energy, i.e. the energy to remove an electron from the atom, plotted as a function of proton number,  $Z$ , has distinct discontinuities at specific atomic numbers. These jumps are caused by electrons being organized into shells, which produce a clear set of “magic numbers” when shells are filled. The magic numbers for atomic physics are 2, 10, 18, 36, 54 and 86, corresponding to

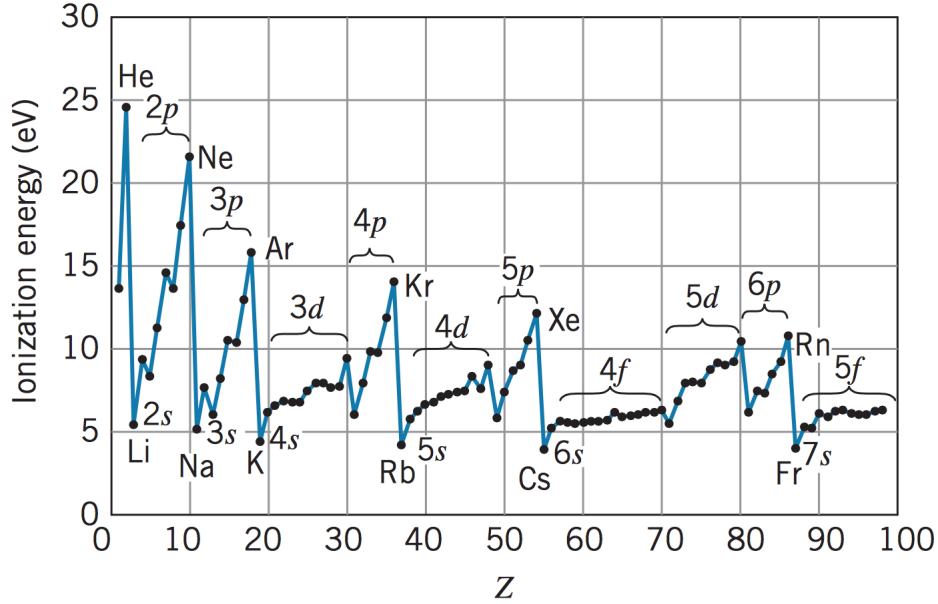


Figure 1.1: Ionization energies of neutral atoms of the elements [2].

the noble gasses, and are easily identified by their increased ionization energy.

There is a similar phenomenon in the nucleus. Through different experiments, magic numbers for a nuclear shell model have been found for nuclei near stability. The interactions in the nucleus does not only depend on a Coulomb interaction between protons but also the strong nuclear interactions between all nucleons. With both of these forces, the magic numbers for nuclei near stability correspond to  $N, Z = 2, 8, 20, 28, 50, 82$  and  $126$  for both protons and neutrons, as shown in figure 1.2. Identifying these magic numbers can be achieved by looking at how bound a nucleon is in the nucleus, represented by the separation energy  $S_{2p}$  for protons and  $S_{2n}$  for neutrons. The reasoning for two proton and neutron separation energies is due to the even-odd staggering in the pairing of nucleons in the nucleus. When a shell is filled there is a large increase in the separation energy. Protons and neutrons are not identical particles. Because of this, they each have their own shells to

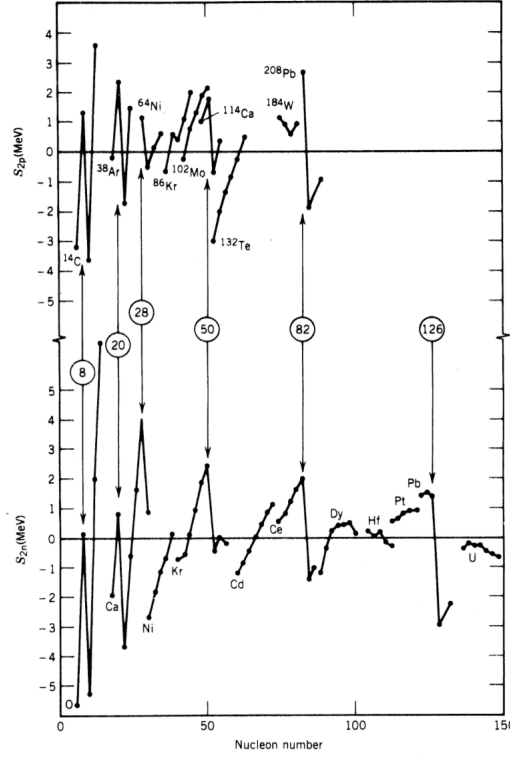


Figure 1.2: The two neutron and two proton separation energies versus nucleon number, with increased separation energies at the magic numbers.

fill independently, while following the Pauli exclusion principle.

To understand the nuclear magic numbers, we start by approximating the nuclear potential as a simple harmonic oscillator. In Cartesian coordinates this is represented as:

$$U(r) = -U_o + \frac{1}{2}m\omega^2(x^2 + y^2 + z^2). \quad (1.1)$$

Solving the Schrödinger equation for a spherically symmetric harmonic oscillator potential in three dimensions gives the familiar result for the energy eigenvalues of  $E = \hbar\omega(N + \frac{3}{2})$ , with  $N$  being the principal quantum number represented by  $N = n_x + n_y + n_z$  and  $n_x, n_y$  and  $n_z$  have integer values. In the spherical case the principal quantum number is represented

as  $N = 2n_r + l$ . The energies of the harmonic oscillator are thus only dependent on  $N$ , with the degeneracy of the levels given by  $\frac{1}{2}(N+1)(N+2)$ . This result arises from the solutions to the radial component which allows only specific values for the orbital angular momentum for a given  $N$ . The orbital angular momentum is at most allowed to be equal to  $N$  and if  $N$  is odd (or even) then the orbital angular momentum must be odd (or even) as well. Knowing this, the shell gaps, or magic numbers, produced by the harmonic oscillator can be calculated.

N	$E_n(\hbar\omega)$	Levels	Degeneracy	Magic Number
0	3/2	1s	2	2
1	5/2	1p	6	8
2	7/2	2s, 1d	12	20
3	9/2	2p, 1f	20	40
4	11/2	3s, 2d, 1g	30	70
5	13/2	3p, 2f, 1h	42	112

Table 1.1: Magic numbers for a spherical harmonic oscillator potential. The levels are listed in spectroscopic notation with s, p, d, f, g and h corresponding to orbital angular momentum  $l = 0, 1, 2, 3, 4$  and  $5$  respectively.

The harmonic oscillator successfully reproduces the first three nuclear magic numbers of 2, 8, 20 but after this it fails to reproduce the experimental results. In order to reproduce all of the magic numbers successfully, a better description of the nuclear potential is needed than simply the harmonic oscillator. With the introduction of a Wood-Saxon potential [3] and an additional term used to describe spin-orbit coupling occurring at the surface of the nucleus, it is possible to begin to describe real nuclei by considering nucleons to move in a potential described by.

$$U(r) = \frac{U_o}{1 + e^{((r-R_o)/a)}} + \frac{U_{ls}}{r_o^2} \frac{1}{r} \frac{d}{dr} \left( \frac{1}{1 + e^{((r-R_o)/a)}} \right) \hat{l} \cdot \hat{s}. \quad (1.2)$$

Here  $U(r)$  is the potential evaluated at radial distance  $r$ ,  $a$  is a surface thickness parameter,  $R_o = r_o A^{\frac{1}{3}}$  with  $r_o \approx 1.2 fm$  and  $A$  is the number of nucleons in the nucleus. The first term in this equation is the Wood-Saxon potential while the second portion is the spin-orbit potential. Spin-orbit coupling is mainly a surface phenomenon and only comes into play when  $r$  is sufficiently close to the nuclear surface  $R$ .

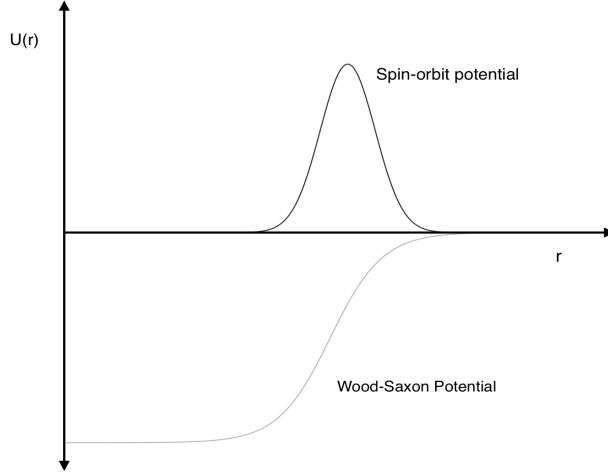


Figure 1.3: A plot of the Wood-Saxon potential and the spin-orbit coupling coming into play at the nuclear surface.

With the addition of the spin-orbit coupling, this potential successfully reproduces the experimental magic numbers and provides a good description of the organization of shell structure for stable nuclei. As nuclei move away from stability and closer to the drip lines, corresponding to the maximum number of protons or neutrons a nucleus can contain before it no longer can remain in a bound state, this shell structure evolves and other magic numbers are observed to form [4].

The evolution of nuclear shell structure is an extremely interesting and active field of research with many different tests to elucidate the structure of nuclei. There are thousands of known nuclei thus far with many more to be discovered. In figure 1.5 an idea of how

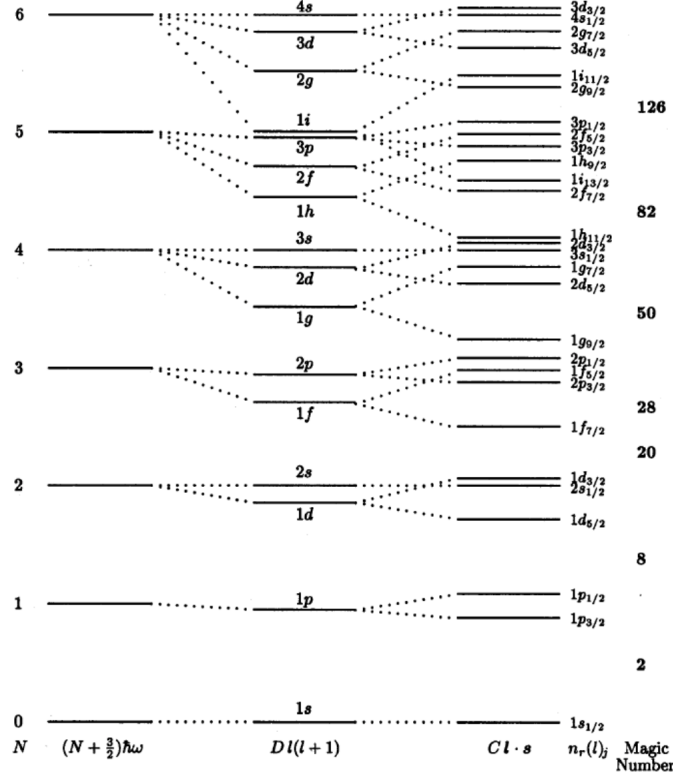


Figure 1.4: The single particle energy levels for the harmonic oscillator (far left) and the Wood-Saxon with the addition of a spin-orbit term (far right), which reproduces the experimentally observed magic numbers  $N, Z = 2, 8, 20, 28, 50, 82, 126$ .

the nuclear chart appears and some basic properties are presented. In this chart, all of the nuclei which are not black are unstable and will thus decay to a more stable state via radioactive decay processes described in the following section. From these decays, nuclear spin determinations through angular correlation measurements are one test to comprehend nuclear structure. With nuclei generally ending up in an excited state after an  $\alpha$  or  $\beta$  decay, one can study the couplings of the valence nucleons in the outer most shells that make up the spin of the nucleus.



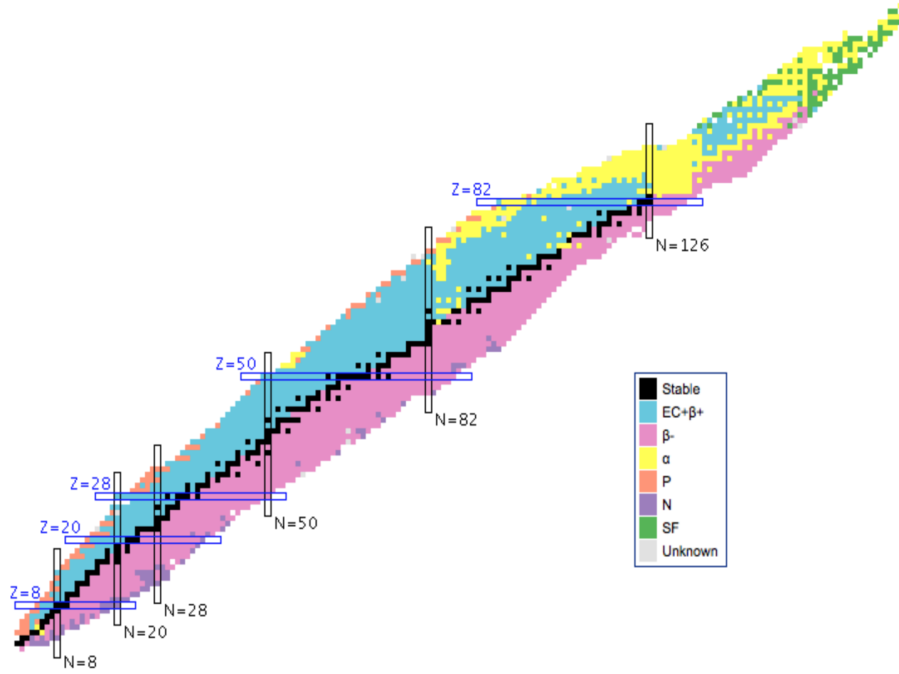


Figure 1.5: The chart of nuclides showing stable and radioactive nuclei.

## 1.2 Radioactive Decay

Several thousand unique isotopes made up of particular combinations of protons and neutrons, each of which has different characteristics such as mass, life-time and other properties are known to be bound. Most of these configurations of protons and neutrons are, however, unstable, meaning they generally release energy or matter in order to proceed towards stability. The main decay processes a nucleus can undergo consist of  $\alpha$ ,  $\beta$  and  $\gamma$  decay as well as spontaneous fission. Spontaneous fission generally occurs in heavy nuclei, causing them to break apart into two large fragments and a number of free neutrons.  $\alpha$  decay is the emission of an  $\alpha$  particle consisting of a tightly bound system of two protons and two neutrons. It is similar to spontaneous fission as they are both governed by the strong nuclear force.  $\beta$  decay is the process by which a nucleus converts a proton into a neutron or vice

versa, causing a  $\beta$  particle and a neutrino or anti-neutrino to be emitted.  $\beta$  decay occurs via the weak interaction.

$$\alpha \text{ decay: } {}^A_Z X_N \rightarrow {}^{A-4}_{Z-2} Y_{N-2} + \alpha$$

$$\beta^+ \text{ decay: } {}^A_Z X_N \rightarrow {}^A_{Z-1} W_{N+1} + e^+ + \nu_e$$

$$\beta^- \text{ decay: } {}^A_Z X_{N+} \rightarrow {}^A_{Z+1} V_{N-1} + e^- + \bar{\nu}_e$$

An additional weak interacting process is electron capture (EC). This is similar to the  $\beta^+$  decay, but captures an atomic electron instead of emitting a  $\beta^+$ .

$$\text{EC decay: } {}^A_Z X_N + e^- \rightarrow {}^A_{Z-1} W_{N+1} + \nu_e$$

These methods of spontaneous decay all require that the energy or the particles in the reactants have a larger mass-energy than the products. The difference in the mass energy between the two is denoted as the  $Q$ -value. For the previously defined decay methods, the  $Q$ -values can be expressed as:

$$Q_\alpha = M({}^A_Z X_N)c^2 - M({}^{A-4}_{Z-2} Y_{N-2})c^2 - M(\alpha)c^2$$

$$Q_{\beta^+} = M({}^A_Z X_N)c^2 - M({}^A_{Z-1} W_{N+1})c^2 - 2m_e c^2$$

$$Q_{\beta^-} = M({}^A_Z X_N)c^2 - M({}^A_{Z+1} V_{N-1})c^2$$

$$Q_{EC} = M({}^A_Z X_N)c^2 - M({}^A_{Z+1} W_{N-1})c^2$$

where  $M({}^A_Z X_N)c^2$  is the mass of a neutral atom with  $Z$  protons and  $N$  neutrons in the nucleus.

Finally, there is  $\gamma$  decay an electromagnetic interaction. This occurs when a nucleus is in an excited state and emits a  $\gamma$ -ray to achieve a lower energy state.  $\gamma$  decay is the only one listed here that does not change the number of protons or neutrons in the nucleus. It can be thought of as a reorganization of the nucleus to achieve a lower energy state.

### 1.2.1 Radioactive Decay Law

Starting with a number of nuclei,  $N_o$ , the number that remain after a given time interval is given by:

$$dN = -N_o\lambda dt \tag{1.3}$$

where  $\lambda$  is the *decay constant* or *transition rate* for a particular isotope of interest, and has units of inverse seconds,  $dt$  is a time interval and  $N$  is the number of remaining nuclei. If both sides of the equation are integrated, the number of parent nuclei remaining as a function of time can be written as:

$$N(t) = N_o e^{-\lambda t}. \tag{1.4}$$

This is the well known radioactive decay law.

A common quantity used in radioactive decay is the *half-life*. This is the amount of time it takes in order for the original number of nuclei to be reduced by half. Substituting  $N = \frac{N_o}{2}$  into equation (1.4) the half-life is given in terms of the decay constant by:

$$T_{1/2} = \frac{\ln 2}{\lambda}. \tag{1.5}$$

If multiple modes of decay are possible, the decay is classified as a *multi-modal decay*. Instead of having only one decay constant, there is one for each decay mode. The total decay

constant is then the sum of the decay constants for each mode of decay. For example, if there are two modes of decay possible, then  $\lambda_T = \lambda_1 + \lambda_2$  with  $\lambda_1$  and  $\lambda_2$  being the decay constants for each mode. Sometimes one method of decay is favoured over another and occurs more frequently. Determining these probabilities gives the *branching ratios*. Branching ratios tell you how often each decay mode occurs as a fraction of the total number of decays. In the prior example with  $\lambda_1$  and  $\lambda_2$ , the branching ratio for mode one is  $B_{\lambda_1} = \frac{\lambda_1}{\lambda_T}$ . More generally, the branching ratio for mode  $i$  is given by:

$$B_{\lambda_i} = \frac{\lambda_i}{\lambda_T} \tag{1.6}$$

with  $i$  being a particular branch or mode the nucleus can decay by. The sum of the branching ratios must be unitary as they describe all methods of decay [5].

### 1.3 Theory of $\gamma$ Decay

Most forms of nuclear decay, including  $\alpha$  and  $\beta$  decays, will often produce a daughter nucleus in an excited state [6]. These excited states can have a large range of possible half-lives. Excited states, in general, decay to lower energy states via the emission of one or more  $\gamma$ -rays. If an excited state reaches the ground state by the emission of a single  $\gamma$ -ray, the process has the form:

$$\gamma \text{ decay: } {}^A_Z X_N^* \rightarrow {}^A_Z X_N + \gamma$$

with  $*$  representing the nucleus in an excited, or higher energy, state. At this point it is

important to restate that the nucleus has not changed in terms of the number of protons,  $Z$ , or neutrons,  $N$ , but has just reorganized itself into a different configuration.

For  $\gamma$ -ray emission to occur, the nucleus in an excited state emits a  $\gamma$ -ray that carries away energy and momentum with  $E_\gamma = pc = \hbar\omega$ , with  $\omega$  being the angular frequency. The precise measurement of the energies of these  $\gamma$ -rays give us the difference in energy between the quantized energy levels of the nucleus. In a transition from an initial excited state  $E_i$  to some lower energy state  $E_f$ , and assuming that the nucleus is initially at rest, the emission of the  $\gamma$ -ray will cause the nucleus to recoil to conserve energy and momentum. Using the laws of conservation of energy:

$$E_i = E_f + E_\gamma + E_{KR} \quad (1.7)$$

with  $E_\gamma$  being the energy of the emitted  $\gamma$ -ray and  $E_{KR}$  being the recoil energy of the nucleus. Using conservation of momentum:

$$0 = p_{KR} + p_\gamma. \quad (1.8)$$

Knowing that the recoil energy of the nucleus is very small due to its large mass, ( $E_{KR} \ll E_i - E_f$ ) then to a good approximation  $E_\gamma \approx E_i - E_f$ . This is a good first-order approximation, but the recoil kinetic energy has to be taken into account for high-precision measurements. Knowing the energies of the  $\gamma$ -ray transitions between nuclear excited states, it is possible to start placing transitions to build a level scheme.

The transition rate between initial and final states for a time-dependent quantum-mechanical

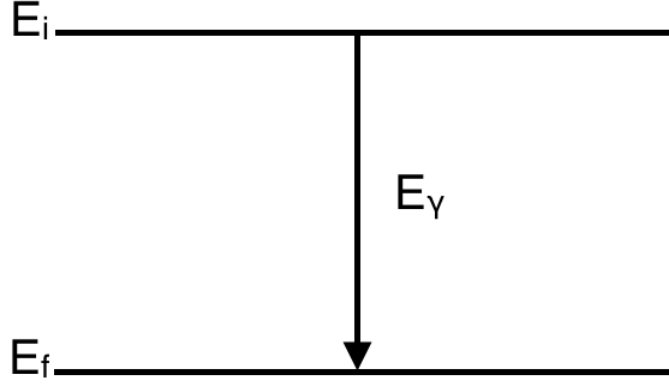


Figure 1.6: Representation of an excited state energy,  $E_i$ , decaying to a lower energy state,  $E_f$ , by emitting a  $\gamma$ -ray.

process is given by Fermi's Golden Rule:

$$\lambda = \frac{2\pi}{\hbar} | \langle \psi_f | \hat{H}_{int} | \psi_i \rangle |^2 \rho(E_f) \quad (1.9)$$

where  $\langle \psi_f | \hat{H}_{int} | \psi_i \rangle$  is the matrix element that connects the initial and final states and  $\rho(E_f)$  is the density of final states, or the number of available states per unit energy at the final energy,  $E_f$ . This expression is independent of the type of transition ( $\alpha$ ,  $\beta$ ,  $\gamma$ , etc.) but for the following it will be discussed in terms of  $\gamma$  decay.

In the kinematics of  $\gamma$  decay there is only one independent momentum (the photon). If we normalize wave functions in a box of volume  $V$ , the number of quantum states available with momentum up to  $p_\gamma$  is:

$$n = \frac{1}{(2\pi\hbar)^3} \int \int d^3x d^3p. \quad (1.10)$$

If the integrals are performed, the number of states can be expressed as:

$$n = \frac{V}{2\pi\hbar} \frac{4\pi p_\gamma^3}{3} \quad (1.11)$$

with  $p_\gamma = \frac{E_\gamma}{c}$  and  $n$  being the number of available states. The density of states, or number of states available per unit of energy, is:

$$\rho(E_\gamma) = \frac{\partial n}{\partial E_\gamma} = \frac{4\pi V E_\gamma^2}{(2\pi\hbar c)^3}. \quad (1.12)$$

The next step is to determine the matrix element. For a non-relativistic point charge we can write the electromagnetic Hamiltonian as [5]:

$$\hat{H} = \hat{H}_o + \hat{H}_{int} = mc^2 + \frac{\not{p}^2}{2m} + q\Phi + \frac{(\not{p}qA)}{m} + \frac{q^2 A^2}{2m} \quad (1.13)$$

here the Hamiltonian is broken into a free particle in an electromagnetic field,  $\hat{H}_o$ , and an interaction term,  $\hat{H}_{int}$ ,  $\not{p}$  is the momentum,  $m$  is the mass,  $q$  is the charge,  $\Phi$  is the electrostatic potential and  $A$  is the vector potential. The last term in equation 1.13 represents two-photon emission or absorption, which is generally less probable than the case of single photon emission or absorption. Neglecting this term, assuming that the electrostatic potential is zero, and using the relation  $\not{p} = -i\hbar\nabla$  the interaction Hamiltonian then becomes:

$$\hat{H}_{int} = \frac{(iq\hbar \nabla A)}{m}. \quad (1.14)$$

Noting that the vector potential is just the wave function of the photon for a plane wave [7,8]

it is seen that:

$$A = \sqrt{\frac{2\hbar^2}{\epsilon_o V E_\gamma}} \vec{\epsilon} \cos(\vec{k} \cdot \vec{r} - \omega t) \quad (1.15)$$

where  $\vec{\epsilon}$  is the polarization vector for the photon,  $V$  is the volume and  $\epsilon_o$  is the permittivity of free space. Expanding the cosine function in terms of exponentials and using the *dipole approximation*, which accepts only the lowest angular momentum term for the photon ( $L = 1$ ):

$$A = \frac{\hbar}{\sqrt{2\epsilon_o V E_\gamma}} \vec{\epsilon} [e^{\frac{iE_\gamma t}{\hbar}} + e^{\frac{-iE_\gamma t}{\hbar}}]. \quad (1.16)$$

The next term in the expansion would represent the quadrupole portion of the photon wave function, and so on.

Looking back at the matrix element, we have:

$$\langle \psi_f | \hat{H}_{int} | \psi_i \rangle = \frac{iq\hbar \vec{\epsilon}}{m\sqrt{2\epsilon_o V E_\gamma}} \int \psi_f^*(\vec{r}) \vec{\nabla} \psi_i(\vec{r}) d^3 \vec{r}. \quad (1.17)$$

Using commutator relationships and knowing the energy eigenstates of the Hamiltonian, we can rewrite Fermi's Golden Rule:

$$\lambda = \frac{4\alpha c}{3} \left( \frac{E_\gamma}{\hbar c} \right)^3 |\langle \psi_f | \vec{r} | \psi_i \rangle|^2 \quad (1.18)$$

with  $\alpha$  being the fine structure constant ( $\approx \frac{1}{137}$ ). At this moment it is important to note that the matrix element is zero unless the initial and final wave functions have opposite parity. This gives rise to the parity and angular momentum selection rules for electric dipole



transitions:

$$\pi_i = -\pi_f \quad (1.19)$$

$$\vec{J}_i = \vec{J}_f + \vec{1}. \quad (1.20)$$

If we include higher order transitions other than the dipole, then the general selection rules become:

$$\pi_i = (-1)^{L_\gamma} \pi_f \quad \textit{Electric transitions} \quad (1.21)$$

$$\pi_i = (-1)^{L_\gamma+1} \pi_f \quad \textit{Magnetic transitions} \quad (1.22)$$

$$\vec{J}_i = \vec{J}_f + \vec{L}_\gamma \quad (1.23)$$

with  $L_\gamma$  being the angular momentum of the photon.

Excited nuclear states have specific nuclear spins and parities, both considered to be good quantum numbers. The emission of  $\gamma$  rays conserves angular momentum as the nucleus transitions from one state to the next. If there is a transition from a state  $J_i$  to a lower energy state  $J_f$ , the angular momentum of the  $\gamma$  ray,  $L_\gamma$ , must be in the range of  $|J_i - J_f| \leq$

$L_\gamma \leq J_i + J_f$ . The angular momenta of the states involved in this transition  $J_i$  and  $J_f$  must be oriented in some direction in space, causing them to be in a specific magnetic substate, or m-state. These m-states span from  $-J_i$  (or  $-J_f$ ) to  $J_i$  (or  $J_f$ ) in integer steps. For example, if  $J_i = 3$  then the possible m-state values are  $-3, -2, -1, 0, 1, 2, 3$  in units of  $\hbar$ .

## 1.4 Weisskopf Estimates

If we assume that a transition from an excited state to a lower energy state involves only a single particle, the wave function of that particle can be broken into a radial component and angular component described by a spherical harmonic function. Crudely assuming that the radial component of the wave function is constant out to the nuclear radius,  $R$ , and zero beyond, an order of magnitude estimate can be made for the transition rate. These estimates are called *Weisskopf estimates*. For electric transitions these estimates are given by [9]:

$$\lambda(EL) = \frac{2\pi\alpha c(L+1)}{L[(2L+1)!!]^2} \left(\frac{E_\gamma}{\hbar c}\right)^{2L+1} \left(\frac{3}{L+3}\right)^2 R^{2L} \quad (1.24)$$

with  $R = R_o A^{\frac{1}{3}}$  ( $R_o \approx 1.2 fm$ ) is the nuclear radius,  $\alpha$  is the fine structure constant ( $\approx 1/137$ ) and  $A$  the nuclear mass number. Similarly, for magnetic transitions, the transition estimates are given by [9]:

$$\lambda(ML) = \frac{10\alpha c(L+1)}{L[(2L+1)!!]^2} \left(\frac{E_\gamma}{\hbar c}\right)^{2L+1} \left(\frac{3}{L+3}\right)^2 R^{2L-2} \left(\frac{\hbar c}{m_p c^2}\right)^2, \quad (1.25)$$

where  $m_p$  is the mass of the proton. Evaluating the above expressions for either electric or magnetic transitions at a given multipole order,  $L$ , and the immediate higher order,  $L + 1$ , it is seen that for a nucleus with  $A \approx 100$  nucleons that:

$$\frac{\lambda[\sigma(L + 1)]}{\lambda(\sigma L)} \approx 10^{-5} E_\gamma^2 \quad (1.26)$$

with  $E_\gamma$  in units of  $MeV$ .

This implies that the lower multipole order transitions are much more likely to occur than higher multipole order transitions. Also, taking a ratio of electric and magnetic transition rates for the same multipolarity, even though a transition cannot be both for a single value of  $L$  because of the parity selection rules given in equations (1.21) and (1.22), it is noticed that the electric transitions have higher transition rates by a factor:

$$\frac{\lambda(EL)}{\lambda(ML)} \approx 3.2 A^{\frac{2}{3}}. \quad (1.27)$$

Because of the favouring of the electric transitions, the possibility arises that electric transitions of order  $L + 1$  can compete with magnetic transitions of order  $L$ , if both satisfy the parity and momentum selection rules for a given transition.

## 1.5 Mixing Ratios

If more than one available multipolarity is allowed by the angular momentum and parity selection rules in equation 1.23, it is possible to have a mixture of electric and magnetic transitions as noted above. This is quite common as E2 transitions in particular are often enhanced with respect to Weisskopf estimates and frequently compete with M1 transitions.

In this case we define a *mixing ratio*:

$$\delta = \frac{\langle \psi_f | E(L+1) | \psi_i \rangle}{\langle \psi_f | ML | \psi_i \rangle} \quad (1.28)$$

which compares the relative matrix elements for electric and magnetic transitions. The reason why the electric transition is in the numerator is because the mixing of higher order electric transitions with lower order magnetic transitions is possible as the transition rates can be comparable. For the opposite case, one generally does not see a mixing between M2 and E1 for example, as the ratio of the transition rates is more like  $10^{-7} E_\gamma^2$ . This is, of course, dependent on the very crude assumptions made in the Weisskopf estimates, and large deviations in transition rates from the single-particle Weisskopf estimate can, and do, occur.

The fraction of electric and magnetic contributions to such decays is given by  $E(L+1) = \frac{\delta^2}{1+\delta^2}$  and  $ML = \frac{1}{1+\delta^2}$ . Obviously, they sum to unity.

## 1.6 Angular Correlations

If a nuclear state does not experience a magnetic field, meaning that the m-states are degenerate and equally populated in an ensemble of nuclei, the  $\gamma$ -rays emitted by that ensemble of nuclei must be isotropic in the laboratory frame. This is because all possible m-states must be summed over to give the angular distribution, as seen in Figure 1.7.

Each individual m-state can be seen to yield an anisotropic distribution, but with equal populations of each m-state, then by summing over all m-states the angular distribution becomes isotropic.

This can be seen in Table 1.2 by looking at the dipole radiation, summing the three

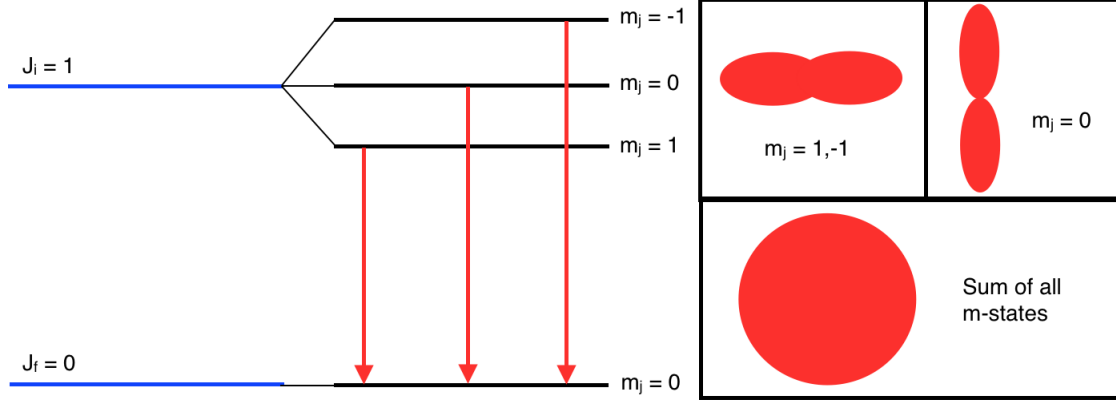


Figure 1.7: The images on the top right show the anisotropic distributions for single  $m$ -states ( $\Delta m = \pm 1$  and  $\Delta m = 0$ ), the total being the sum over all  $m$ -states is isotropic.

Multipole	$m = 0$	$m = \pm 1$	$m = \pm 2$
Dipole ( $L = 1$ )	$\sin^2\theta$	$\frac{1}{2}(1 + \cos^2\theta)$	
Quadrupole ( $L = 2$ )	$6\sin^2\theta\cos^2\theta$	$1 - 3\cos^2\theta + 4\cos^4\theta$	$1 - \cos^4\theta$

Table 1.2: Dipole and quadrupole directional dependences according to  $m$ -state population.

$m$ -states and representing this angular distribution by  $W(\theta)$ :

$$W(\theta) \propto \frac{1}{2}(1 + \cos^2\theta) + \sin^2\theta + \frac{1}{2}(1 + \cos^2\theta) \propto 1. \quad (1.29)$$

The sum is proportional to a constant, yielding a completely isotropic distribution of  $\gamma$  rays.

When an excited nucleus decays by emitting multiple  $\gamma$  rays, an anisotropy is generally found in the spatial distribution of the second  $\gamma$  ray with respect to the first. If the first  $\gamma$  ray is defined to be the  $z$ -axis, and therefore defines the  $m$ -states, then the intermediate state will, in general, have an unequal population of  $m$ -states. For a  $J = 0$ ,  $m = 0$  initial state, for example, the  $m=0$  intermediate state cannot be populated because the photon must carry away at least one unit of angular momentum ( $L = 1$ ) with  $m = \pm 1$  along the

direction of propagation. For the case of a  $0 \rightarrow 2 \rightarrow 0$  cascade the  $m = \pm 1$  intermediate states are populated giving:

$$W(\theta) \propto 1 - 3\cos^4\theta - 4\cos^2\theta \quad (1.30)$$

for the angular correlation between the two  $\gamma$ -rays shown in this cascade.

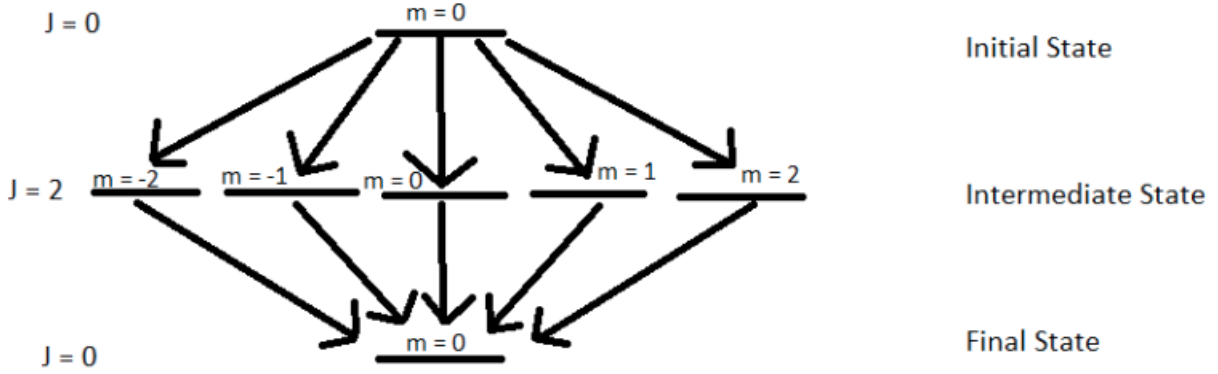


Figure 1.8: Possible transitions for a  $0 \rightarrow 2 \rightarrow 0$  cascade. Allowing the first  $\gamma$ -ray to be defined as the z-axis, then the  $m = 0$  and  $\pm 2$  states for the intermediate level can not be populated.

Of course, as higher and higher angular momenta are considered, the more complicated these scenarios become. The general form for angular correlations [10–13],  $W(\theta)$  is given by:

$$W(\theta) = \sum_{k=0, k=\text{even}}^{2L} a_k P_k(\cos\theta), \quad (1.31)$$

where the  $a_k$  are coefficients dependent on the nuclear spins of the states involved, angular

momentum carried by the  $\gamma$ -ray and the mixing ratios, while the  $P_k(\cos\theta)$  are the Legendre polynomials. The sum in this equation involves only even values of  $k$  (to conserve parity) and extends to twice the lowest multipolarity of the  $\gamma$  rays involved in the cascade. For example, if the cascade is quadrupole-quadrupole as in the  $0 \rightarrow 2 \rightarrow 0$  cascade mentioned above then,  $W(\theta) = a_0 P_0(\cos\theta) + a_2 P_2(\cos\theta) + a_4 P_4(\cos\theta)$ . The Legendre polynomials are a set of even and odd functions dependent on the order  $k$ . The first few Legendre polynomials are listed below with  $x$  representing  $\cos\theta$ :

Legendre Polynomial Order	Form
$P_0(x)$	1
$P_1(x)$	$x$
$P_2(x)$	$\frac{1}{2}(3x^2 - 1)$
$P_3(x)$	$\frac{1}{2}(5x^3 - 3x)$
$P_4(x)$	$\frac{1}{8}(35x^4 - 30x^2 + 3)$

Table 1.3: Table of the first five Legendre polynomials.

As was previously mentioned, the angular correlation coefficients are dependent on the spin assignments of the initial, intermediate and final states in the cascade, the multipolarity of the two  $\gamma$  rays and the mixing ratios for mixed transitions. The values of these coefficients are thus one way of determining the spins of nuclear levels. Even though there has been no direct mention about parities thus far and the angular correlations themselves do not strictly depend on the parity of the states, by combining the multiplicities of the transitions determined from the angular correlations with the selection rules, parities can often be inferred. The angular correlations also allow the determination of unknown mixing ratios.

Looking specifically at the formulation of the angular correlation coefficients, they can be described by two symmetric functions, with one being dependent on the first  $\gamma$ -ray and

the other on the second  $\gamma$ -ray:

$$a_k = A_k(\gamma_1)D_k(\gamma_2) \quad (1.32)$$

where the even  $k$  values usually have a maximum value of four when looking at actual experiments, meaning that the radiation is either dipole, quadrupole or some combination of the two. As long as the transitions in the cascade occur quickly enough in time, and do not pass through a long-lived isomeric state [14], the values of  $k$  range up to the lesser of either two times the maximum multipolarity of the  $\gamma$ -ray,  $2L_{max}$ , or two times the maximum nuclear spin,  $2J_i$  [15]. The  $A_k$  and  $D_k$  are given by:

$$A_k^{max}(\gamma_1) = \frac{1}{1 + \delta_1^2} (f_k(L_1, L_1, J_i, J_f) + 2\delta_1 f_k(L_1, L'_1, J_i, J_f) + \delta_1^2 f_k(L'_1, L'_1, J_i, J_f)) \quad (1.33)$$

$$D_k^{max}(\gamma_2) = \frac{1}{1 + \delta_2^2} (f_k(L_2, L_2, J_i, J_f) + 2\delta_2 f_k(L_2, L'_2, J_i, J_f) + \delta_2^2 f_k(L'_2, L'_2, J_i, J_f)) \quad (1.34)$$

where the max superscript represents the system if it is completely aligned and the  $f_k$  coefficients are functions of the multipolarities of the  $\gamma$ -ray, mixing ratios, as well as the nuclear spins of the levels involved:

$$f_k = (-1)^{J_f - J_i - 1} [(2L_1 + 1)(2L_2 + 1)(2J_i + 1)]^{\frac{1}{2}} (L_1 1 L_2 - 1 | k 0) W(J_i J_i L_1 L_2; k J_f) B_k(J_i). \quad (1.35)$$



Here  $B_k(J_i)$  is an alignment parameter proportional to a Clebsh-Gordan coefficient,

$$B_k(J) = (2J + 1)^{1/2}(-1)^J(J0J0|k0) \quad (1.36)$$

for integral spin and

$$B_k(J) = (2J + 1)^{1/2}(-1)^{J-1/2}(J\frac{1}{2}J\frac{1}{2}|k0) \quad (1.37)$$

for half-integral spin. If the system is not completely aligned, as is the case in most experimental situations, then there is an alignment coefficient that needs to be included in equations 1.33 and 1.34.

$$A_k(\gamma_1) = \alpha_k A_k^{max}(\gamma_1) \quad (1.38)$$

and

$$D_k(\gamma_2) = \alpha'_k D_k^{max}(\gamma_2). \quad (1.39)$$

The  $\alpha_k$  coefficients describe the alignment of nuclei and are related to  $B_k(J)$  by:

$$\alpha_k(J_i) = \frac{\rho_k(J_i)}{B_k(J_i)} \quad (1.40)$$

where  $\rho_k(J_i)$  is a statistical tensor expressed as:

$$\rho_k(J) = (2J + 1)^{\frac{1}{2}} \sum_m (-1)^{J-m} (JmJ - m|k0) P_m(J) \quad (1.41)$$

with the  $P_m(J)$  being the population of the m-states [11].

The theoretical values of  $f_k$  in equation 1.35 also depend on the Racah coefficients:

$$(-1)^{j_1+j_2+j_4+j_5} W(j_1 j_2 j_5 j_4; j_3 j_6) = \left\{ \begin{matrix} j_1 & j_2 & j_3 \\ j_4 & j_5 & j_6 \end{matrix} \right\} \quad (1.42)$$

where  $W(j_1 j_2 j_5 j_4; j_3 j_6)$  is the Racah coefficient and is proportional to the Wigner 6j symbol [16]:

$$\left\{ \begin{matrix} j_1 & j_2 & j_3 \\ j_4 & j_5 & j_6 \end{matrix} \right\} = \sum_{m_i} (-1)^S \left( \begin{matrix} j_1 & j_2 & j_3 \\ m_1 & m_2 & -m_3 \end{matrix} \right) \left( \begin{matrix} j_1 & j_5 & j_6 \\ -m_1 & m_5 & m_6 \end{matrix} \right) \quad (1.43)$$

$$\left( \begin{matrix} j_4 & j_5 & j_3 \\ m_4 & -m_5 & -m_3 \end{matrix} \right) \left( \begin{matrix} j_4 & j_2 & j_6 \\ -m_4 & -m_2 & -m_6 \end{matrix} \right)$$

which itself is a sum over Wigner 3j symbols with  $S = \sum_{n=1}^6 (j_n - m_n)$ . Finally, these Wigner 3j symbols are comprised of Clebsch-Gordan coefficients describing the angular momentum coupling between specific values of  $j_1$ ,  $j_2$  and  $j_3$  and their magnetic substates:

$$\left( \begin{matrix} j_1 & j_2 & j_3 \\ m_1 & m_2 & -m_3 \end{matrix} \right) = \frac{(-1)^{j_1-j_2-m_3}}{\sqrt{2j_3+1}} \langle j_1 m_1 j_2 m_2 | j_3 - m_3 \rangle. \quad (1.44)$$

The  $f_k$  coefficients have been calculated in tables for many different possibilities of cascades [11, 17, 18], a number of which are shown in table 1.4.

Using the formulations discussed in equation 1.32 through equation 1.44,  $f_k$  coefficients

Cascade	$a_2$	$a_4$
$0 \rightarrow 2 \rightarrow 0$	0.3571	1.1419
$4 \rightarrow 2 \rightarrow 0$	0.1020	0.0091
$1 \rightarrow 2 \rightarrow 0$ ( $\delta = -5$ )	0.3627	-0.7326
$3 \rightarrow 2 \rightarrow 0$ ( $\delta = 0$ )	-0.0714	0.0000
$2 \rightarrow 2 \rightarrow 0$ ( $\delta = 0$ )	0.2500	0.0000
$2 \rightarrow 2 \rightarrow 0$ ( $\delta = 1$ )	-0.2792	0.1633

Table 1.4: Theoretical coefficients of a few cascades with different values of nuclear spins. In all cases the coefficients are normalized such that  $a_0 = 1$ . It can be seen that the values for these coefficients can vary quite drastically as the mixing ratio is changed as well.

were calculated with a C++ code so as not to rely on tables, particularly as the mixing ratios are continuous parameters that can take on any value [19]. With the  $f_k$  coefficients calculated, the correlations coefficient yield the theoretical angular correlation for any given cascade and mixing ratios. The intensity,  $W(\theta)$ , is plotted as a function of angle for some representative cascades in Figure 1.9.

With many of these angular correlations showing distinct anisotropies, they can be used to determine the spins and parities of excited nuclear states. With the knowledge of these spins and parities, physical models of nuclei can be refined as our knowledge of nuclear structure expands.

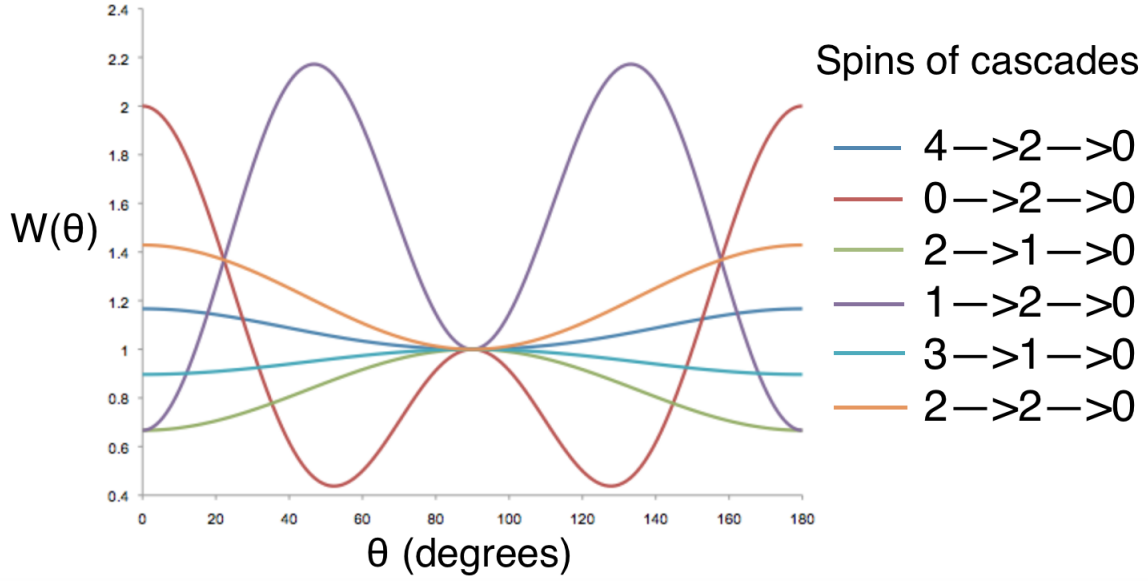


Figure 1.9: Example angular correlations for a variety of nuclear cascades. It can be seen that some correlations have stronger anisotropies than others. Mixing ratios, when relevant, are given in Table 1.4.

## 1.7 Experimental Angular Correlation Measurements and Spin Assignments

Gamma-Gamma angular correlation measurements to assign nuclear spins have been performed since the 1940s. Over the years, different methods have been used to extract the spins of nuclear excited states from these angular correlations, allowing scientists to better elucidate nuclear structure and test theoretical models. A brief overview of various methods as described by Robinson [20], is presented in the following sections.

### 1.7.1 Direct Correlation Coefficient Measurements

The first method used was to attempt to extract the  $a_2$  and  $a_4$  values directly, assuming that cascades are only dependent on dipole and quadrupole transitions. The measured angular correlations would be corrected for the opening angle of the detectors, deorientation effects of any intermediate states and also attenuation due to the interaction of any long-lived intermediate states with extranuclear fields. After the corrections to the correlation data were completed, a quadratic fit in  $\cos^2\theta$  would be made to determine the  $a_2$  and  $a_4$  values, as well as the error on the  $a_2$  and  $a_4$  coefficients. Most commonly, a least-squares fit routine would be used and a reduced chi-squared would be determined from the fit to the data.

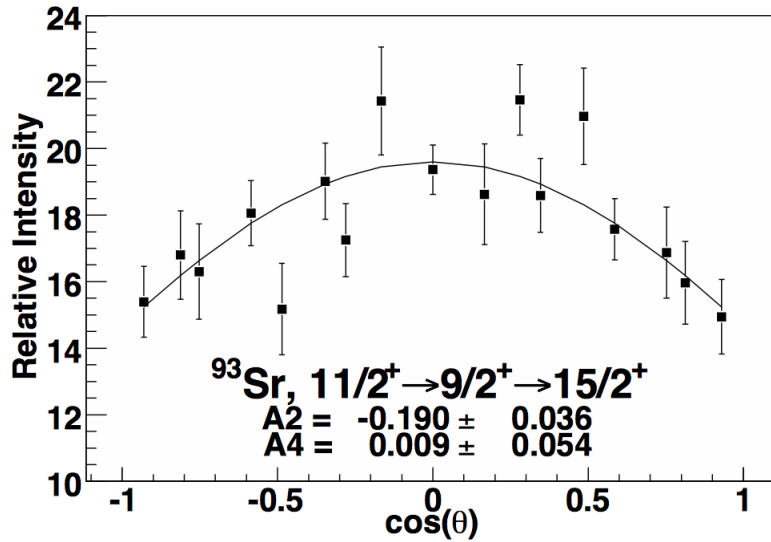


Figure 1.10: The angular correlation for the 1182.5 keV and 986.1 keV transitions in  $^{93}\text{Sr}$  [21].

In Figure 1.10 the angular correlation measured between the 1192.5 keV and 986.1 keV transitions in  $^{93}\text{Sr}$  is shown. The data points are represented by the black squares and the

fit by the continuous line through the data. From the fit the  $a_2$  and  $a_4$  coefficients are determined to be  $-0.190 \pm 0.036$  and  $0.009 \pm 0.054$  respectively. With the measured  $a_2$  and  $a_4$  coefficients, the states in this cascade we assigned spins of  $11/2^+ \rightarrow 9/2^+ \rightarrow 15/2^+$  with the  $11/2$  spin not previously known.

### 1.7.2 Ellipse Comparisons

In some cases involving  $\gamma$ -ray mixing ratios it is common to generate ellipses by plotting the  $a_2$  and  $a_4$  coefficients against each other [22]. With both the  $a_2$  and  $a_4$  coefficients are dependent on the same mixing ratios there is a correlation between them, in general this is true for all  $a_k$  coefficients. As these values converge for large positive and negative mixing ratios, a smooth ellipse is made with the theoretical values of the coefficients. If there is no mixing then, the  $a_2$ ,  $a_4$  coefficients simply appear as a point on the graph.

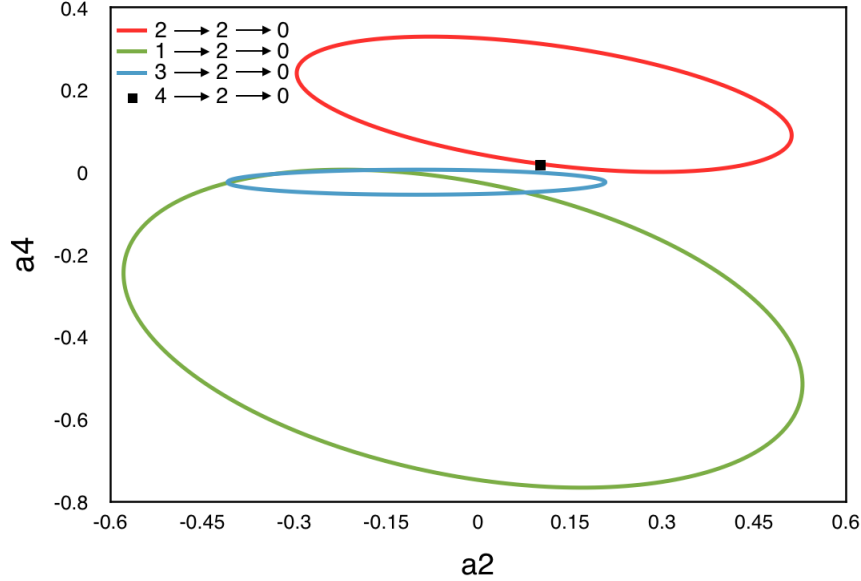


Figure 1.11: Theoretical ellipses for a few cascades that can have E2/M1 mixing as well as a  $4 \rightarrow 2 \rightarrow 0$  cascade where no mixing occurs.

It is important to note from Figure 1.11 that the  $a_2$  and  $a_4$  coefficients of the  $4 \rightarrow 2 \rightarrow 0$  cascade are effectively identical for a  $2 \rightarrow 2 \rightarrow 0$  with a particular mixing ratio of  $\delta = 0.19$ . Also, making a comparison between the  $1 \rightarrow 2 \rightarrow 0$  and the  $3 \rightarrow 2 \rightarrow 0$  it can be seen that they have effectively identical correlations for a range of mixing ratios corresponding to  $-0.10 \leq \delta \leq 0.19$  for the  $1 \rightarrow 2 \rightarrow 0$  and  $-1 \leq \delta \leq -0.12$  for the  $3 \rightarrow 2 \rightarrow 0$  cascade.

The experimentally determined  $a_2$  and  $a_4$  were then overlaid on a series of such ellipses, which represented different nuclear spins and mixing ratios. If the error on the  $a_2$  and  $a_4$  would overlap with the ellipse, within  $2\sigma$ , it would be considered as a possible spin assignment. The mixing ratio was then taken from the theoretical values using the closest point on the ellipse and having  $1\sigma$  taken for the error from the confidence of the intersection with the ellipse.

### 1.7.3 Goodness-Of-Fit vs. Mixing Ratio

A third method uses a non-linear least square fit to the measured angular correlation function,  $W(\theta)$ , taking the mixing ratio as a parameter of the fit. A goodness-of-fit test is preformed by extracting a reduced chi-square between the experiment and theoretical  $W(\theta)$  values at each measured angular separation  $\theta_i$ :

$$\chi^2 = \frac{\sum_i (W_{exp}(\theta_i) - W_{th}(\theta_i))^2}{\Delta W_{exp}(\theta_i)^2} \quad (1.45)$$

Plotting the  $\chi^2$  versus the  $\arctan(\delta)$ , minima can be seen for specific ranges of mixing ratios. Within defined confidence limits, the spin values that agree with the measured angular correlation can be determined and the mixing ratio in each case extracted.

From Figure 1.12, two confidence levels are set at 95% and 99%. At these levels,  $2\sigma$  and

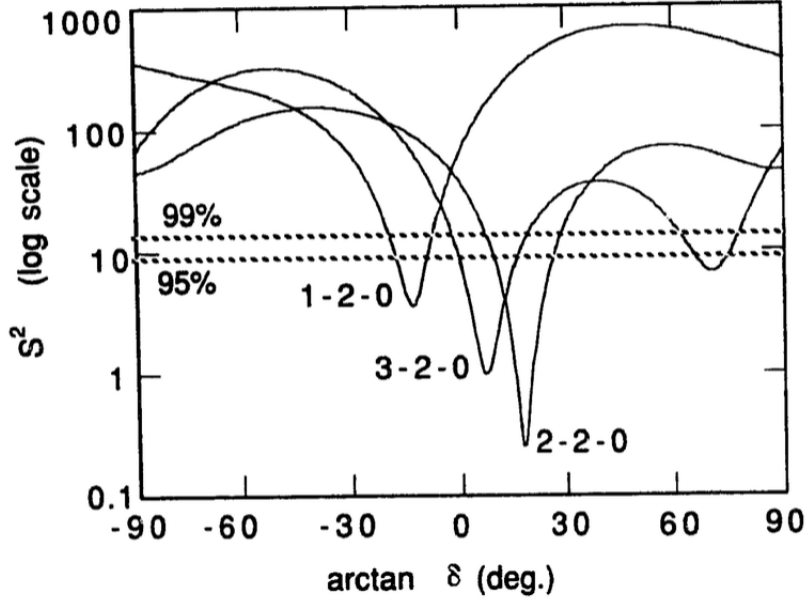


Figure 1.12: Chi squared values between an experimentally measured  $\gamma$  ray cascade in  $^{146}\text{Nd}$  [20] and various theoretical correlations from different nuclear spin assignments as a function of mixing ratio. Minima are clearly seen and in each case a range of values for the mixing ratios can be extracted.

$3\sigma$  estimates can be taken for mixing ratios that satisfy the given confidence level. For the data, the spins that agree with the data include  $1 \rightarrow 2 \rightarrow 0$ ,  $2 \rightarrow 2 \rightarrow 0$  and  $3 \rightarrow 2 \rightarrow 0$  illustrating that angular correlation measurements do not always provide definitive spin assignments.

## 1.8 Methodology for Spin Assignments Via Angular Correlations Measurements With GRIFFIN

Robinson was able to show the above methods are not all equally effective, which can potentially lead to mislabelling of spins and mixing ratios for excited states [20]. For this analysis the goodness-of-fit method is used, as it was stated to be the most effective. It becomes difficult to extract the  $a_2$  and  $a_4$  values directly once a  $\gamma$ -ray detector has a geometry



more complicated than a cylinder. For early measurements, two detectors, usually of simple geometry, were placed at specific locations spatially and moved to get intensities at various angles. By integrating over the solid angle subtended by the detector face a geometric correction factor, or Q value, value was determined (not to be confused with the radioactive decay Q values given in Section 1.2. The Q-value was then used as a correction for the  $a_k$  angular correlation coefficients [23]. These values could be corrected with the Q-value solid angle correction since the detectors were simple in geometry. As will be discussed in more detail in Chapter 2, the detectors being used in this research are not simply cylinders, but rather four-leaf "clover" detectors with each square face separated into four segments. The crystal shape themselves also have complicated geometry with tapered edges and are not cylindrically symmetric. This makes it difficult to determine the Q-values solid angle correction.

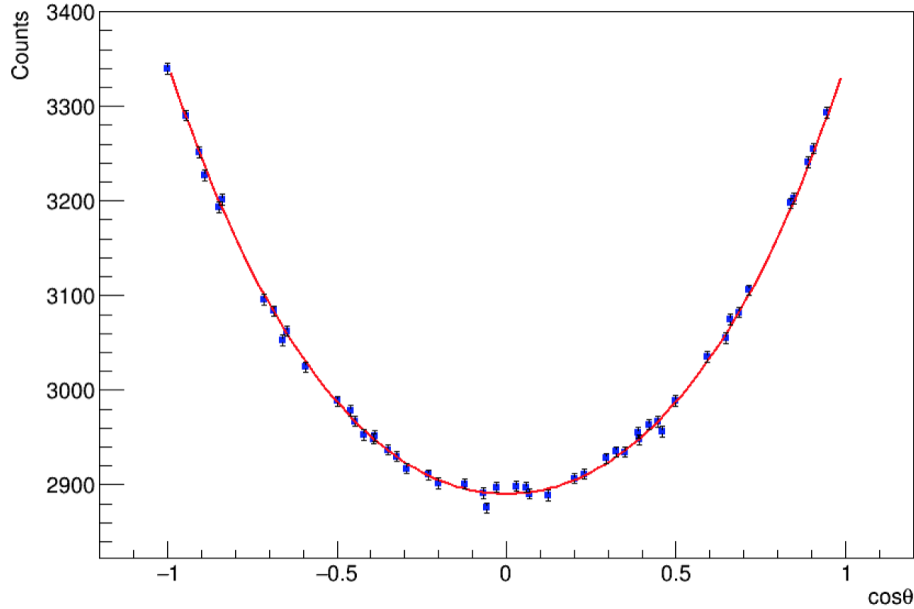


Figure 1.13: Angular correlation template of the  $4^+ \rightarrow 2^+ \rightarrow 0^+$  cascade in  $^{60}\text{Co}$  simulated data points (blue) fit with  $W(\theta)$  function (red).

The goodness-of-fit test is rather done with Monte Carlo simulations that were run to produce sets of “templates” given the theoretical angular correlations for the experimental geometry used. With the use of Geant4 various templates were generated for cascades involving different angular correlation coefficients. The templates were run using the same detector geometry as in the experiment. These templates were used to make a direct comparison with experimental data to extract a  $\chi^2$  to produce  $\chi^2$  vs.  $\arctan(\delta)$  plots for various cascades. In Figure 1.13 an example template is seen for the  $4^+ \rightarrow 2^+ \rightarrow 0^+$  cascade in  $^{60}\text{Co}$  decay. By running simulations using the detector geometry, it alleviates the need for detector solid angle corrections and should allow for more accurate measurements of mixing ratios. The  $\chi^2$  vs.  $\arctan(\delta)$  plots measured in this work will be discussed in Chapter 3.

# Chapter 2

## Experiment

### 2.1 TRIUMF

The TRI-University Meson Facility (TRIUMF) in Vancouver, BC, is Canada's national laboratory for nuclear and particle physics research and related sciences. Established in 1966, this facility is centered around the world's largest cyclotron, which allows for a proton beam to be accelerated to energies of 500 MeV. The proton beams can be delivered directly to experimental halls or can collide with a target to produce secondary beams [24].

#### 2.1.1 ISAC

One of the halls located at TRIUMF is the Isotope Separator and ACcelerator (ISAC). This facility uses the Isotope Separation On-Line (ISOL) technique. The ISOL technique consists of primary beam production, a target/ion source, a mass separator and a secondary beam transport system. The Rare Isotope Beams (RIBs) that are produced stop in the primary production target, diffuse, inside the hot target to the surface, and effuse to the

ion source where they are ionized [25]. Once ionized these particles are accelerated through an electric potential difference of  $\Delta V = 30 \text{ kV}$  to an energy of  $30 \text{ keV}$  and enter the mass separator, which is used for selecting the desired beam by its mass to charge ratio,  $A/q$ . Since the spallation reactions with the target generally favour the production of isotopes with a similar ratio of neutron number to proton number as the target material it can be difficult to produce beams of very neutron (or proton) rich nuclei. As a rough rule of thumb, as you move away from stability along an isotopic chain, for each neutron added (toward the neutron dripline) or removed (toward the proton dripline) a loss of approximately an order of magnitude in beam rate occurs.

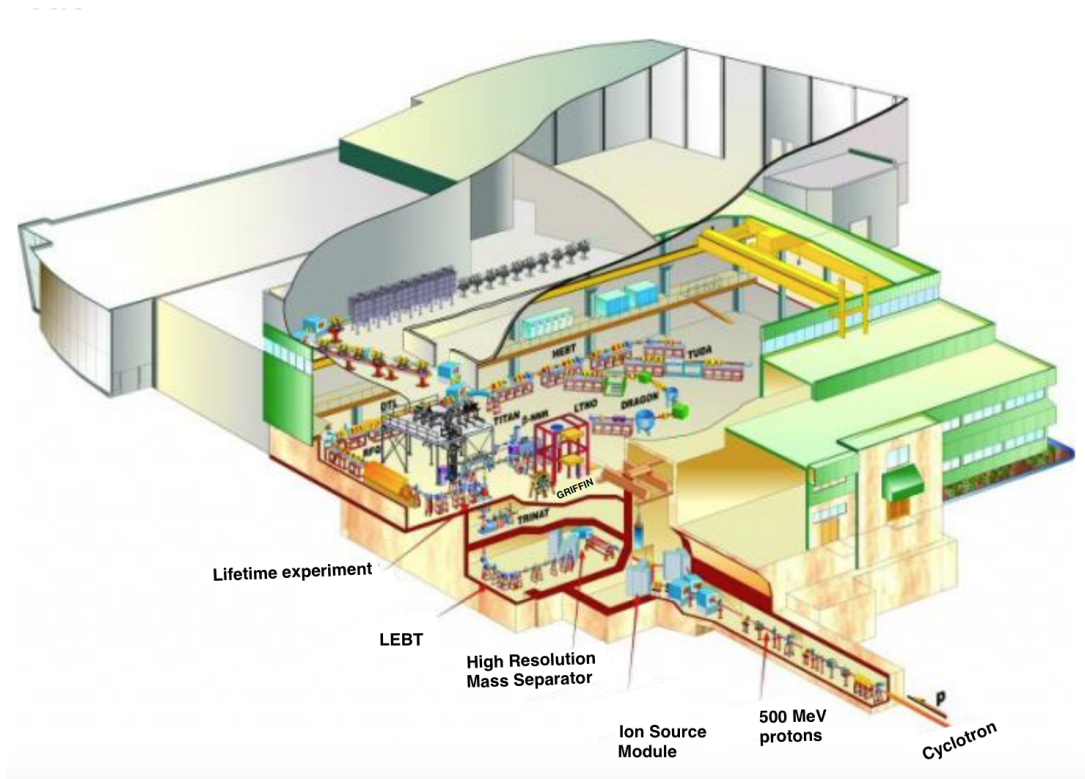


Figure 2.1: The layout of the ISAC facility at TRIUMF [24].

To deliver the ionized products to the experimental hall, the mass separator uses a

constant magnetic field to bend the charged particles through a  $45^\circ$  arc, with radius of curvature.

$$R = \frac{1}{B} \sqrt{\frac{2m\Delta V}{q}} \quad (2.1)$$

dependent on the mass,  $m$ , the charge,  $q$ , the magnetic field,  $B$ , and the electric potential difference,  $\Delta V$ . As  $B$  and  $\Delta V$  are common for all isotopes at a given time, based on their charge-to-mass ratio, the mass separator is able to distinguish between particles with a resolving power of  $\frac{\Delta m}{m} \approx \frac{1}{1000}$ , eliminating ions with different mass number,  $A$ , but often transmitting isobaric contaminants at the same mass number. For example, a  $^{10}\text{C}^{16}\text{O}$  molecular beam can be accompanied by a contaminant of  $^{13}\text{N}_2$ . Both of these molecules have  $A = 26$  with fourteen protons and twelve neutrons and the mass difference is less than the resolution of the mass separator. With nearly identical (as far as the mass separator is concerned) charge-to-mass ratios, these contaminants must be dealt with appropriately by other methods when analyzing the data. Following mass separation the RIB is delivered to the appropriate experimental facility either as a low-energy (30 keV) beam, or following acceleration higher energies if required for a given experiment.

## 2.2 Gamma-Ray Interactions in Germanium Detectors

A major difficulty in the detection of  $\gamma$  rays stems from the fact that they are able to travel much farther into materials than other types of radiation, such as  $\alpha$  or  $\beta$  particles. As they do not interact continuously like a charged particle via the Coulomb force,  $\gamma$  rays must have “catastrophic interactions” with atoms of the detector material. Due to this fact, detectors built for  $\gamma$  ray spectroscopy must utilize relatively large volumes to gain efficiency.

The main types of  $\gamma$  ray detectors involve using either scintillators, such as sodium-iodide (NaI), or semi-conductors, such as high-purity germanium (HPGe) crystals. In the past, it was easier to make large volume crystals for NaI than it is for HPGe, giving them larger efficiencies because there is more material for the  $\gamma$  rays to travel through. However, the energy resolution of HPGe far surpasses that of NaI. A distinction between peaks of similar energy can thus be made because of the gain in resolution provided by HPGe. This difference in energy resolution is highlighted in Figure 2.2. The difference in width of the peaks is easily noticeable, and hence, if attempting to resolve peaks close in energy, HPGe is the detector material of choice.

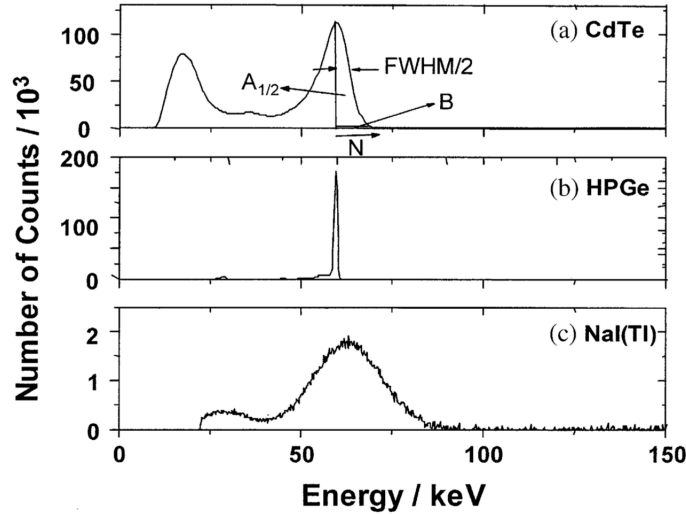


Figure 2.2: A comparison of CdTe, HPGe and NaI detectors used for  $\gamma$ -ray spectroscopy with  $\gamma$ -rays from a  $^{241}\text{Am}$  source [26].

In  $\gamma$  ray detectors different processes can occur inside the detection material. The significant interactions include Compton scattering, photoelectric absorption and pair production. These events cause many different sources of background, so they are important to comprehend when analyzing data. In Figure 2.3 the relative attenuation coefficients are shown

with the photoelectric effect dominating at low energies, Compton scattering at intermediate energies, and pair production dominating for higher energy  $\gamma$ -rays.

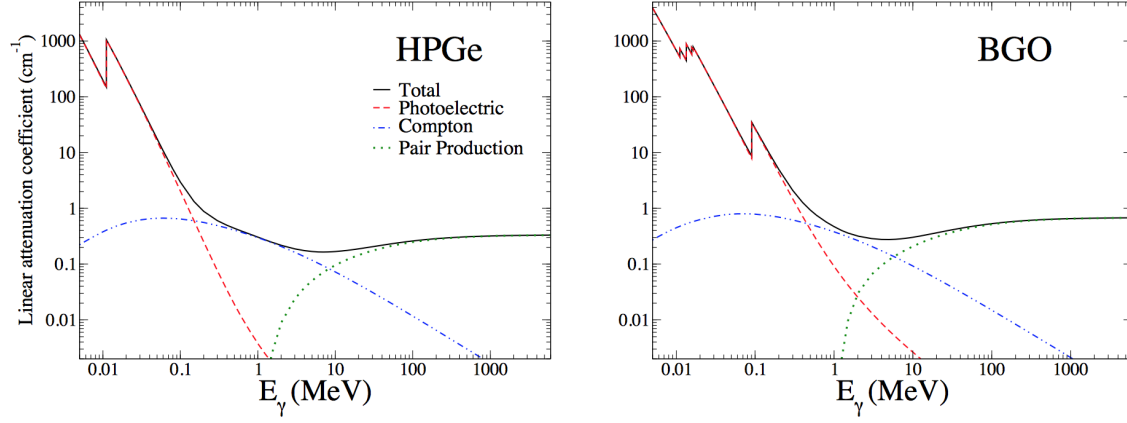


Figure 2.3: The linear attenuation coefficients for photoelectric absorption, Compton scattering and pair production as a function of the  $\gamma$ -ray energy in germanium (HPGe) and bismuth germanate (BGO) [27].

### 2.2.1 Photoelectric Absorption

In the photoelectric absorption process, a photon interacts with an atom and is absorbed. All of the energy of the photon is transferred to an electron in one of the electron shells. This produces a photoelectron that is ejected from the atom. After the photoelectron is ejected, the atomic electrons must rearrange to fill the hole that was created. This will emit characteristic X-rays or Auger electrons from the atom. All of the energy of the incident photon is transferred to the photoelectron with its energy given by:

$$E_{e^-} = E_\gamma - E_b \quad (2.2)$$

where  $E_b$  was the binding energy of the electron in the atom. This process is dominant for lower energy  $\gamma$  rays, usually less than about 100 *keV* in HPGe. Not only does the photo absorption probability increase for low  $\gamma$  ray energies but it also increases for atoms with a high atomic number,  $Z$ . The probability of photoelectric absorption is approximated by:

$$\sigma \propto \frac{Z^n}{(E_\gamma)^3} \quad (2.3)$$

with  $n$  varying between four and five for a given  $\gamma$ -ray energy [28]. The dependence of  $Z$  in this relationship is the primary reason why materials with a large  $Z$ , such as bismuth germanate (BGO), are chosen to be used as Compton shields in doing  $\gamma$ -ray spectroscopy.

### 2.2.2 Compton Scattering

Compton scattering occurs when an incident photon scatters off an electron. This process is dominant for  $\gamma$  rays in the energy range of 100 *keV* to 10 *MeV*. In these events, the  $\gamma$ -ray is deflected from its original direction by an angle,  $\theta$ . When this occurs, a portion of its energy is transferred to the electron causing the electron to recoil with a scattering angle,  $\phi$ . The change in wavelength of the  $\gamma$  ray is given by:

$$\Delta\lambda = \frac{h}{m_e c}(1 - \cos\theta) \quad (2.4)$$

where  $\theta$  is the scattering angle of the  $\gamma$ -ray. This relationship can be derived by applying conservation of momentum and energy to the scattering process under the approximation that the electron is initially free and at rest. Converting to energies, the change in  $\gamma$ -ray energy, which equals the energy given to the recoil electron and, hence, the energy deposited



in the detector is given by:

$$E'_\gamma = E_\gamma \left[ 1 + \frac{E_\gamma}{m_e c^2} (1 - \cos\theta) \right]^{-1}. \quad (2.5)$$

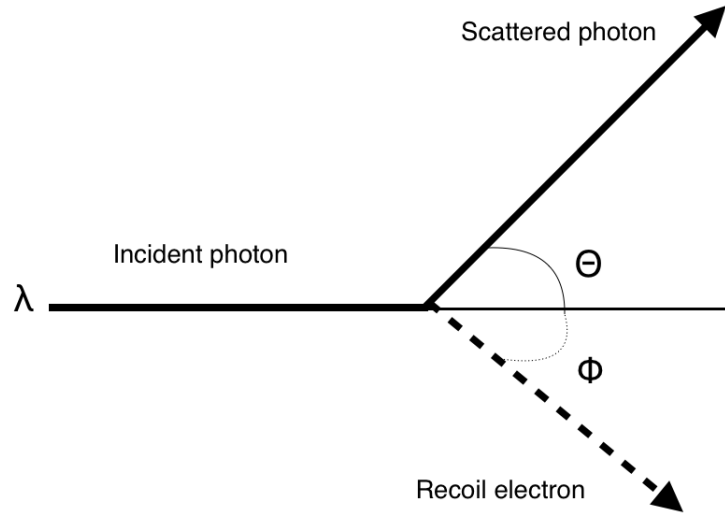


Figure 2.4: Schematic of Compton scattering in which a  $\gamma$ -ray interacts with, and transfers energy to, an electron.

Compton scattering events can occur multiple times depending on the energy of the  $\gamma$ -ray. Sometimes a scattered  $\gamma$ -ray can escape the detector, carrying a portion of the total incident energy with it. Also, depending on which atomic shell the electron is emitted from, there may also be X-rays or Auger electrons created from the de-exciting atom. If the photon just grazes the electron, meaning  $\theta \approx 0$ , the photon will have approximately the same energy before scattering compared to after. If the photon collides and completely back scatters,  $\theta = 180^\circ$ , the maximum energy is transferred to the electron producing what is known as the Compton edge. For the Compton background, suppressors are generally implemented in order to veto events. Suppressors are usually constructed of a material with a large number

of available electrons, increasing the probability of Compton scattering and photoelectric absorption, and thus a high  $Z$  and dense material such as BGO is often used.

### 2.2.3 Pair Production

Every known particle has an antiparticle and if they interact with one another they can annihilate and produce two  $\gamma$ -rays. Similarly, if a  $\gamma$ -ray has energy greater than the sum of the particle-antiparticle masses, it can interact in the Coulomb field of a nucleus and create the particle-antiparticle pair. This is called pair production, and while it begins to occur for  $\gamma$ -ray energies greater than  $m_e c^2 + m_e c^2 = 1.022 \text{ MeV}$  it becomes dominant for  $\gamma$ -rays of higher energy (5  $\text{MeV}$  or more).

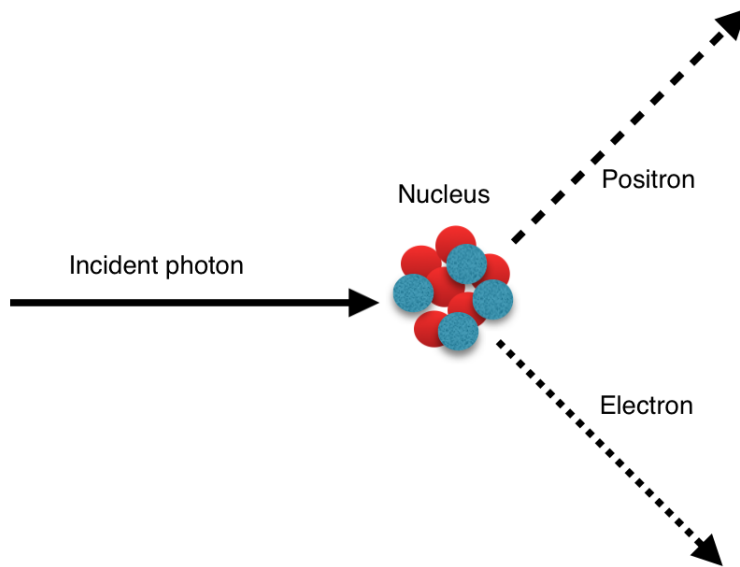


Figure 2.5: An incident photon interacts with the Coulomb field of a nucleus and produces an electron-positron pair.

An issue with pair production is that when the positron stops and interacts with an

electron in the detector it annihilates and creates two 511  $keV$   $\gamma$ -rays. Some of these  $\gamma$ -rays may escape the detector, causing single and double escape peaks at the energy of the initial  $\gamma$ -ray minus 511 or 1022  $keV$ . These can be troublesome if there are peaks of interest in those particular energy ranges.

All three of the processes described above are methods for  $\gamma$ -rays to produce energetic electrons. These energetic electrons interact with the detector material through Coulomb interactions and generate many secondary electrons as they slow down. The ability to resolve the energy of the  $\gamma$ -ray is dependent on the number of these secondary electrons created. The more electrons (or electron-hole pairs) generated in an event, the more precise the energy measurements are due to the statistical fluctuations in the number of such secondary events. Scintillating detectors ultimately convert the ionization to optical light, which is measured to produce the detector signals. This can lead to poor energy resolution making them of limited use when trying to resolve peaks of similar energy. As previously mentioned, this is why semiconductors, such as HPGe detectors, are generally used for detailed  $\gamma$ -ray spectroscopy.

## 2.2.4 Semiconductor Diode Detectors

The use of scintillators generally produces poor energy resolution because the process of converting the  $\gamma$ -ray energy to electrical signals involves many inefficient steps, usually requiring an average of 100  $eV$  or more per optical photon detected [29]. In order to have a better energy resolution, more free charge carriers are needed for  $\gamma$ -rays of the same energy interacting in the same manner. A large HPGe crystal, used as a semiconductor diode, allows for excellent energy resolution. In HPGe diode detectors, only an average of about 3  $eV$  of energy deposited in the detector is required to produce an electron-hole pair.

Crystals have a periodic lattice, with the highest electrons just below the Fermi level

forming a valence band with electrons bound to specific sites within the lattice. Just above this band is a region where electrons in higher energy states can travel. This is called the conduction band and it contributes to the conductivity of the material. These bands are separated by a bandgap, the amount of energy required for an electron to be promoted from the valence band to the conduction band. The size of the bandgap determines whether the material is a conductor, a semiconductor, or an insulator.

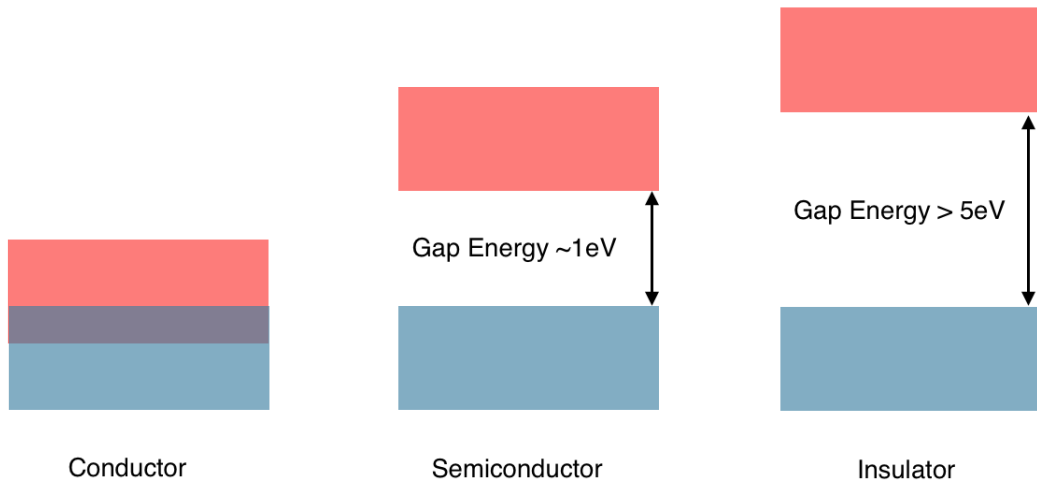


Figure 2.6: Band structure for conducting, semiconducting and insulating materials.

Impurities may be added to the crystal lattice, known as doping, in order to form what is known as a p-n junction. A n-type semiconductor has an impurity that is an electron donor. A donor impurity contains an extra electron that, when in the lattice, is very lightly bound and takes very little energy to become free. These electrons sit very close to the conduction band and a large fraction of them are ionized. Because of this, the number of conduction electrons is much greater than the number of holes, and the electrical conductivity of the material is mainly determined by the flow of electrons. An example of dopant used for producing n-type semiconductors in HPGc is lithium. In contrast, a p-type semiconductor

contains one fewer valence electron. This vacancy is represented by a hole. If an electron is placed in this hole, it will bond in a different way than the majority of the crystal lattice, causing the electron to be slightly less bound. This type of impurity is called an electron acceptor as it creates locations for electrons to be accepted into the lattice with energies near the valence band. An example of such an electron acceptor in HPGe is boron [29]. These electrons and holes act as charge carriers when a bias is applied to the crystal.

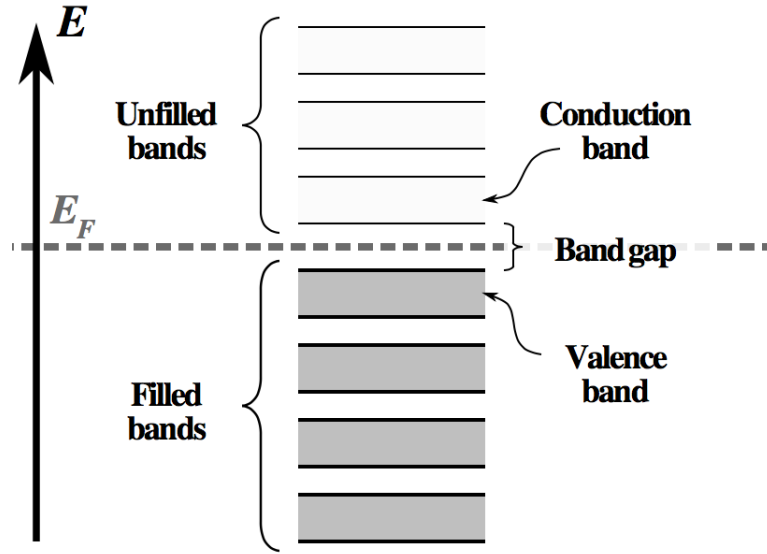


Figure 2.7: Band structure for semiconducting materials showing the filled bands with the Fermi energy.

When a p-n junction is formed, the electron density differences allows for diffusion of the electrons from the n-type side of the junction to drift to the holes of the p-type, causing an electric field to be generated. The diffusion of charges creates a depletion zone, a zone where all free charge carriers are removed. By applying a bias potential that makes the p-side of a diode more negative and the n-side more positive one can increase the size of the depletion region. This is called reverse-biasing the diode. The depletion zone in which there is a large electric field but no free charge carriers, is useful for radiation detection. When

ionizing radiation enters this zone, electron-hole pairs are formed creating a current flow. The amount of charge collected is then proportional to the energy deposited by the radiation. To have good energy resolution, there must be many free charges created, and therefore a low energy requirement for the creation of each electron-hole pair. The more carriers created, the smaller the relative statistical fluctuations and therefore the more precise the energy measurement. The low average energy required to create an electron-hole pair is one of the reasons why HPGe semiconductor diode detectors have better energy resolution than scintillators.

## 2.3 The GRIFFIN Spectrometer

In the summer of 2014, a new  $\gamma$ -ray spectrometer was commissioned at TRIUMF. This array is called the Gamma Ray Infrastructure For Fundamental Investigations of Nuclei (GRIFFIN) [30]. This state-of-the-art high efficiency  $\gamma$ -ray spectrometer is designed to be an improvement over the previous  $8\pi$  spectrometer [31,32]. GRIFFIN, being composed of 16 large-volume clover-type detectors each containing four high-purity germanium crystals, will be used to advance nuclear structure, nuclear astrophysics, nuclear medicine and fundamental symmetries research [30].

With the use of HPGe, GRIFFIN has excellent energy resolution, with a full width at half maximum (FWHM) of approximately  $1.9\text{ keV}$  for  $1.33\text{ MeV}$   $\gamma$ -rays. The beam is implanted on an aluminized mylar tape located in the centre of GRIFFIN. The tape can be moved as required behind a lead shielding wall outside the array. An advantage of this tape is that the beam is stopped and no Doppler corrections are needed to the data set. An additional advantage is, if there are any unwanted daughters or granddaughters following the desired

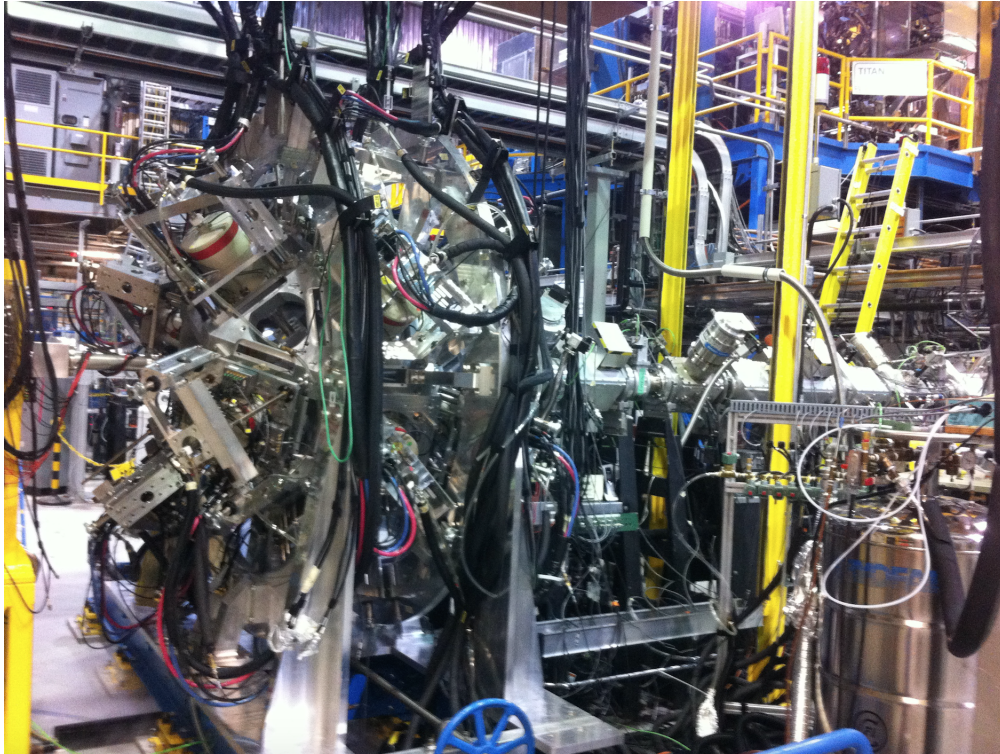


Figure 2.8: The full GRIFFIN array containing all 16 clover-type detectors with the incoming beam-line seen to the right of the array.

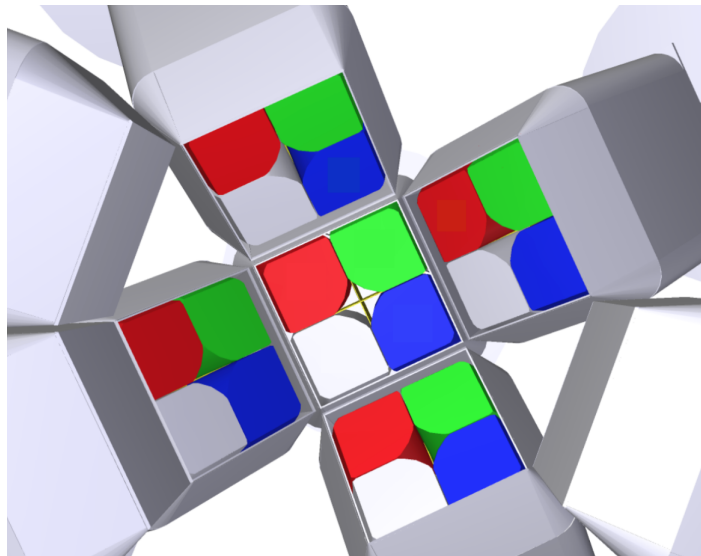


Figure 2.9: A Geant4 simulated image of GRIFFIN detectors with detector faces visible.

decay, they can often be removed from the spectrometer before they decay. The HPGe crystals in GRIFFIN are cut from crystals with an initial size of 90mm long and 60mm diameter, with tapered edges shown in Figure 2.10. The geometry of GRIFFIN is that of a rhombicuboctahedron (with the beam line sections left open), which offers an optimal design for solid angle coverage and angular correlation measurements allowing for the array to be very efficient [30]. The HPGe clover detector faces can either be placed at 11 *cm* from the implantation site on the tape, called the high efficiency mode, or at 14.5 *cm*, which will be used to provide a maximum peak-to-total ratio once BGO shielding is in place. The efficiency gain is most dramatic when comparing to the previous  $8\pi$  spectrometer, especially when detecting  $\gamma - \gamma$  coincidences required for  $\gamma - \gamma$  angular correlation measurements. With the improved efficiency from the large volume clovers, the ability to run experiments that could not be contemplated with the  $8\pi$  are now possible, allowing for the expansion of information on many nuclear properties.

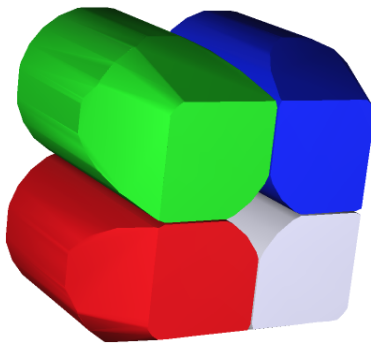


Figure 2.10: The four large-volume crystals contained inside each of the GRIFFIN HPGe clover detectors.

A more quantitative illustration of this improvement is shown in the top left panel of Figure 2.11. The efficiency of GRIFFIN is vastly greater than that of the  $8\pi$  spectrometer. This is because there is a lot more germanium in the GRIFFIN array for the  $\gamma$ -rays to interact



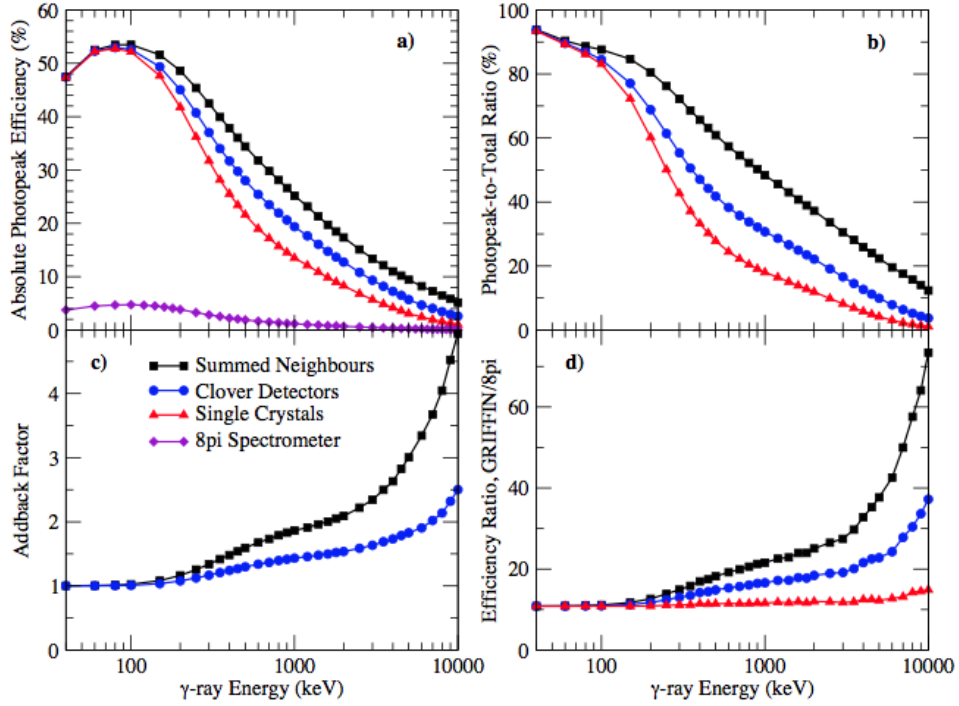


Figure 2.11: Simulated efficiencies of GRIFFIN using Geant4 in single crystal mode (triangles), clover add-back (circles) and neighbouring crystal add-back (squares), as well as  $8\pi$  efficiencies (diamonds). Plot a) shows the absolute photopeak efficiency, b) is the peak-to-total ratio, c) the ratio of add-back performance compared to single crystal methods and d) is the ratio of efficiency in comparison to the  $8\pi$ .

with. For a 1  $MeV$   $\gamma$ -ray, GRIFFIN is approximately 17 times more efficient than  $8\pi$ , and as the energy of the  $\gamma$ -ray increases, so does this ratio of the efficiencies. This is clearly seen in the bottom right panel of Figure 2.11. Now, if one considers a  $\gamma - \gamma$  coincidence efficiency comparison, this improvement factor is squared, meaning a pair of 1  $MeV$   $\gamma$ -rays is detected in coincidence about 300 times more efficiently with GRIFFIN than the previous  $8\pi$  spectrometer. With over two orders of magnitude gain in  $\gamma - \gamma$  efficiency, excited states with much weaker intensities can be studied with angular correlation measurements to determine spin and parity assignments.

### 2.3.1 Angular Properties of GRIFFIN

GRIFFIN has sixteen clover detectors, and 64 individual HPGe crystals. There are thus 4096 ( $64 \times 64$ ) crystal pairs, including a crystal paired with itself when two  $\gamma$ -rays in a cascade interact and deposit their full energy in the same HPGe crystal. The clover detectors in the array can be divided into three components: the first lampshade, corresponding to an angle of  $45^\circ$  relative to the beam axis; the corona, with an angle of  $90^\circ$ ; and the second lamp shade, with an angle of  $135^\circ$ . The first lamp shade contains four detectors, the corona contains eight detectors and the second lamp shade the four remaining detectors.

Detector ID	$\theta_{lab}$	$\phi_{lab}$
1	45	67.5
2	45	157.5
3	45	247.5
4	45	337.5
5	90	22.5
6	90	67.5
7	90	112.5
8	90	157.5
9	90	202.5
10	90	247.5
11	90	292.5
12	90	337.3
13	135	67.5
14	135	157.5
15	135	247.4
16	135	337.5

Table 2.1: Angular positions in the laboratory frame of the centre faces of each HPGe clover detector in the GRIFFIN array.

With the geometry of GRIFFIN, the 4096 crystal pairs produce 52 distinct opening angles between crystals, ranging from zero degrees, i.e. the same crystal, to  $180^\circ$ . When measuring angular correlations these 52 angle pairs can be used to determine the  $a_2$  and  $a_4$  parameters

Open Angle (degrees)	Weight	Open Angle (degrees)	Weight
0.000	64	91.5264	128
18.7868	128	93.7624	48
25.6015	64	93.7716	64
26.6904	64	96.9575	64
31.9463	64	101.331	64
33.6541	48	103.619	96
44.3643	128	106.916	64
46.7937	96	109.140	96
48.5755	128	110.136	64
49.7979	96	112.544	64
53.8336	48	113.359	64
60.1511	96	114.984	96
62.7049	48	116.914	64
63.0860	64	117.295	48
65.0157	96	119.849	96
66.4608	64	126.166	48
67.4562	64	130.202	96
69.8641	64	131.424	128
70.8601	96	133.206	96
73.0838	64	135.636	128
76.3814	96	146.346	48
78.6690	64	148.054	64
83.0425	64	152.310	64
86.2284	64	154.398	64
86.2376	48	160.213	128
88.4736	128	180.000	64

Table 2.2: The 52 unique opening angles between HPGe crystals in the GRIFFIN geometry, for a 1 *MeV*  $\gamma$ -ray, and the corresponding weights, or number of occurrences for each angle.

as discussed in Section 1.6. To determine the angles between crystals two vectors first are assigned to the crystal centres:

$$\vec{v}_i = (r \sin \theta_i \cos \phi_i, r \sin \theta_i \sin \phi_i, r \cos \theta_i)$$

$$\vec{x}_n = (\delta_j c_p, \delta_k c_p, i_d)$$

with  $i = 1, 2$  and  $n = 1, 2, 3, 4$ , for the four crystals. Here,  $r$  is the distance to the centre face of the detector,  $c_p$  is the distance from the centre of the detector to the centre of a crystal,

$i_d$  is the average interaction depth of the  $\gamma$ -ray and  $\delta_{j,k}$  are defined as either  $\pm 1$  depending on which of the four crystals in the detector the vector is pointing to.  $\vec{x}_n$  is rotated with respect to the  $\theta$  and  $\phi$  of  $\vec{v}_i$  and the two vectors are added together. With the dot product of  $(\vec{x}_{n1} + \vec{v}_1) \cdot (\vec{x}_{n2} + \vec{v}_2)$  yield the opening angles between crystals.

It is important to note that since many angles are similar, as seen in Table 2.2, they may be grouped together, and since the angular correlation functions for  $\gamma$ -rays are all symmetric about  $90^\circ$ , the data may also be folded about  $90^\circ$  without loss of information. The method of grouping and folding angles used in this thesis changes the number of angular bins from 52 to 11 distinct angles. The decision on how to group these angles was based on attempting to achieve similar weighting factors for each angle or group, with weighting defined as the number of occurrences each opening angle appears using a unique combination of crystals in the array. This gives approximately equal statistical accuracy in each angular bin.

Open Angle (degrees)	Weight
0.000	128
18.7868	256
26.146	256
32.800	224
45.479	448
50.736	544
61.981	416
66.311	448
72.269	448
79.364	448
87.101	480

Table 2.3: After grouping and folding the angles, eleven opening angles remain in the GRIF-FIN geometry with the indicated weighting factors.

Having such large detector faces, with each crystal face taking up a large portion of the solid angle, and being 90 *mm* in length,  $\gamma$ -ray interactions at different depths correspond to

different angles. With these different interaction depths, the effective average angles between detectors will change as a function of  $\gamma$ -ray energy. Therefore, maps were generated over a range of  $\gamma$ -ray energies using Geant4 to determine the effective average opening angle as a function of energy. How these maps are produced is discussed in Chapter 3.

### 2.3.2 Auxiliary Detectors

GRIFFIN is not a standalone detector. There are a number auxiliary detectors that can be used in conjunction with GRIFFIN for alternative particle detection. For the sake of this thesis, only a brief description will be given.

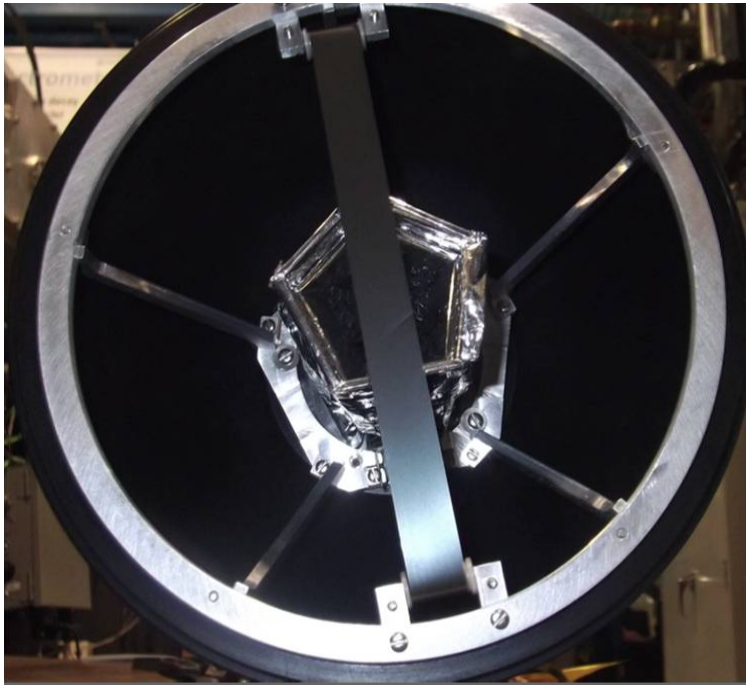


Figure 2.12: One half of the SCEPTAR array inside the vacuum chamber with the tape system visible.

The first of these detectors is the SCintillating Electron-Positron Tagging Array (SCEPTAR) [33], seen in Figure 2.12, which is divided into two hemispheres, each containing 10

thin plastic scintillators of 1.6 *mm* thickness. These panels are arranged into pentagonal rings and are used for the detection of  $\beta$  particles. SCEPTAR has an efficiency of  $\sim 80\%$  and is excellent when tagging on the  $\beta$  particles, especially when considering  $\beta - \gamma - \gamma$  coincidence events that help reject most of the room background signals. It provides a much cleaner spectrum and the ability to detect peaks that may have been immersed in room background events.

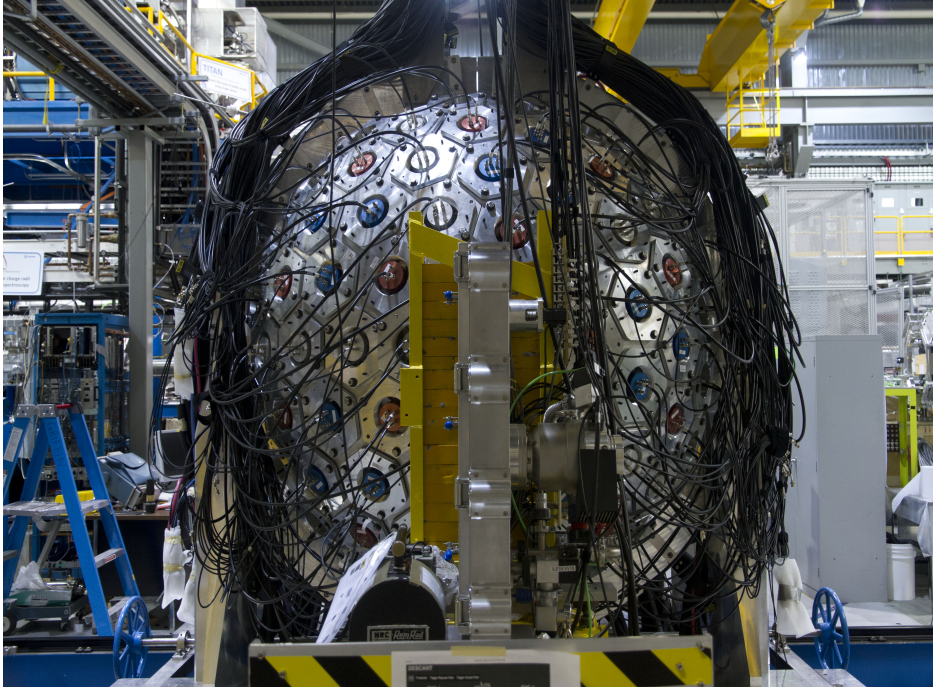


Figure 2.13: The DESCANT array replacing four GRIFFIN clovers and mounted on the GRIFFIN frame.

Another detector shown in Figure 2.13, is the DEuterated SCintillator Array for Neutron Tagging (DESCANT) [34] consisting of 70 closely packed detectors filled with deuterated benzene. This detector is used to study  $\beta$ -delayed neutron emitters. It replaces the lampshade of GRIFFIN in the outgoing beam line direction with the DESCANT detectors approximately 50*cm* from where the beam is implanted. It can also be used with the TRIUMF

ISAC Gamma-Ray Escape-Suppressed Spectrometer (TIGRESS) array [35].

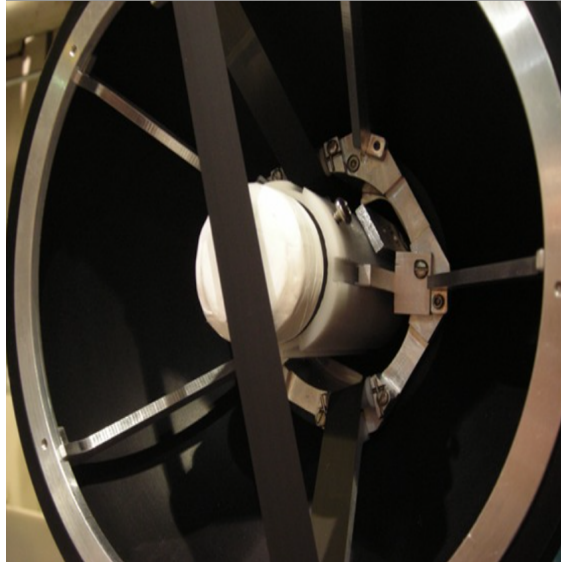


Figure 2.14: Zero degree scintillator behind beam implantation site.

The Zero Degree Scintillator (ZDS), seen in Figure 2.14, is used for fast timing  $\beta$  detection. It is a plastic scintillator that sits immediately behind where the beam is implanted on the tape and can replace one hemisphere of SCEPTAR.

The Pentagonal Array of Conversion Electron Spectrometers (PACES) has five lithium doped silicon detectors and is used for the detection of conversion electrons that compete with  $\gamma$  decay or arise from E0 transitions. This detector is shown in Figure 2.15. Finally, 8 lanthanum bromide ( $\text{LaBr}_3$ ) detectors are available for fast timing measurements with GRIFFIN. With this wide range of auxiliary detectors, GRIFFIN will be able to provide advancements in many aspects of nuclear physics. Given its ability to handle intense beam rates, as well as being a high efficiency device, a wide range of beams and experiments will expand our knowledge about nuclear structure.



Figure 2.15: The PACES array used for detection of internal conversion electrons and  $\alpha$  particles.



# Chapter 3

## Analysis

### 3.1 Simulations and Data Corrections

The first portion of the research reported in this thesis was completed through Geant4 Monte Carlo simulations. Geant4 is a C++ based toolkit used to simulate the interactions of particles travelling through matter [36]. In order to test GRIFFIN’s sensitivity to these  $\gamma - \gamma$  angular correlations, Geant4 simulations were performed for a wide variety of  $\gamma$ -ray energies and for different spins and parities of the nuclear states and different mixing ratios for the  $\gamma$ -ray transitions involved. By changing the energy of the  $\gamma$ -ray, the average interaction depth changes, hence a specific map was generated corresponding to the effective angle of each detector as a function of the energies used. The other effect caused by varying the  $\gamma$ -ray energy is the change in the detector efficiency. With high-energy  $\gamma$ -rays, there is more scattering between detectors, and having full energy deposition in a single crystal becomes less likely. Because of this, different forms of “addback”, i.e. adding energies, were tested and implemented. Altering the nuclear spins and parities and the mixing ratios of

the transitions allows for the investigation of the uniqueness of the angular correlations for different cascades. By studying these differences, it is often possible to assign spin and parity to the nuclear state and to measure the mixing ratios of mixed transitions.

In the Geant4 simulations, specific geometries are defined by their shape (volume), material and position in space. These properties are created by the user and can be as simple or as complicated as required. Once the materials, volumes and locations are set inside the Geant4 world, simulations can commence by firing particles such as  $\gamma$ -rays, protons, neutrons, etc. in a designated direction. These particles are tracked in every volume they travel through and where they interact and deposit energy in those volumes determined by Monte Carlo techniques. Unlike real experiments, the exact location of every step through volumes can be recorded, as well as every point where energy is deposited in a volume. The interaction types are also classified, for  $\gamma$ -rays being labelled as Compton scattering, photoelectric absorption or pair production. Secondary electrons and positrons are also tracked until the energy of the particle reaches a point where its mean range in the material drops below a predefined threshold, and the remaining energy of the particle is assumed to be absorbed. In the simulations performed in this work, the range threshold was set to 1 *mm*.

### 3.1.1 Generating GRIFFIN Maps

Assisted with the ability to track particles at every step with Geant4, GRIFFIN maps, which are an array of opening angles between crystal pairs, were generated in order to view the angular properties of the array's geometry. Because of the different attenuation of  $\gamma$ -rays of different energies, a variety of maps were generated with  $\gamma$ -ray energies from 100 *keV* up to 5 *MeV*. A smooth transition is visible in Figure 3.1 representing the effective opening angle changing between neighbouring crystals in a clover as a function of the  $\gamma$ -ray energy.

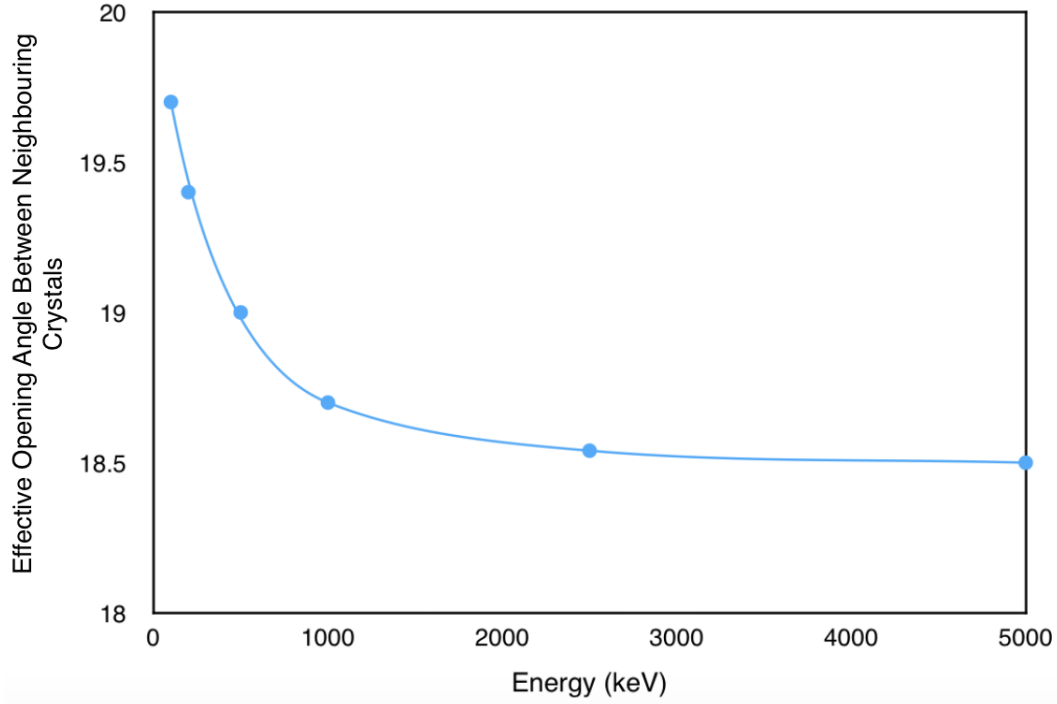


Figure 3.1: Effective opening angle between neighbouring crystals in a GRIFFIN HPGe clover detector as a function of the  $\gamma$ -ray energy.

The method used to determine the effective crystal angular positions for plotting of the angular correlations was as follows:

- Run a simulation with  $\gamma$ -rays emitted in random directions across the crystal surface.
- Use Geant4 to determine the first interaction coordinates  $(r, \theta, \phi)$  only for events with full energy deposition in a single crystal and histogram these  $(r, \theta, \phi)$  values.
- Determine the average  $(r, \theta, \phi)$  for a  $\gamma$ -ray of this particular energy that deposits its full energy in the crystal.
- Once the three spherical coordinates  $(r, \theta, \phi)$  are found for one crystal, use the geometry of the array to determine opening angles for every crystal pair.

The main reason why these simulations had to be preformed is the complex geometry of the detector. If the detector was simply a cube, rectangular prism, or any symmetric shape in  $\theta$  and  $\phi$ , then taking a “centre point” for the crystals would be easier. The crystals in the GRIFFIN detectors are, however, not a simple geometry as they not only have tapered edges, but toward the centre portion of the detector there is a central core for the electrical contact and biasing of the detector with no HPGe for detection.

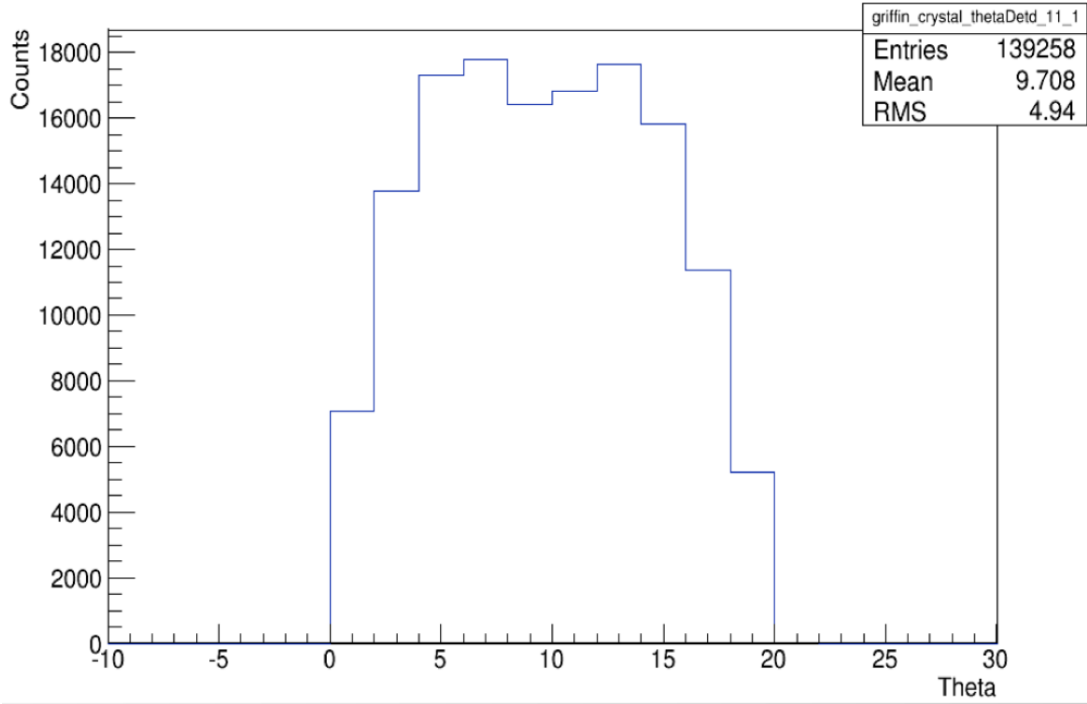


Figure 3.2: Theta distribution for fully absorbed  $\gamma$ -rays in the crystal reference frame for 200 keV  $\gamma$ -rays. The dip in the centre is caused by the central core of the HPGe detector.

### 3.1.2 Angular Correlation Simulation Package

Once the  $\gamma - \gamma$  angular correlation simulation package was installed [37], it was tested by running simulations for multiple cascades in an almost empty Geant4 world. By doing this, it was possible to determine the exact positions where the  $\gamma$ -rays left the world volume.

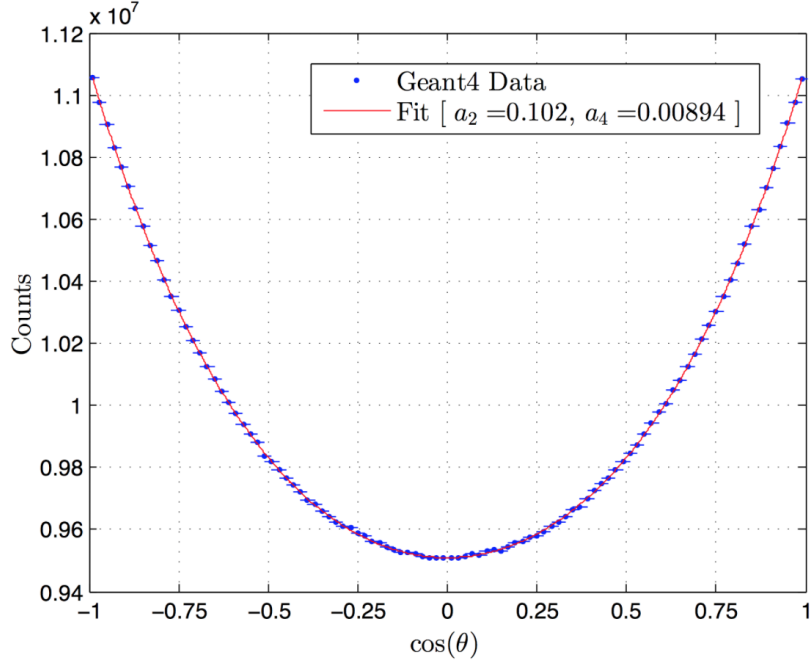


Figure 3.3: Plot of  $4^+ \rightarrow 2^+ \rightarrow 0^+$  cascade with the  $\gamma$ -ray angular correlation being determined by where the two  $\gamma$ -rays exit the (empty) world volume.

With the dot product of the vectors pointing to those locations, the opening angles between the  $\gamma$ -rays were precisely determined. These simulations were run in a galactic environment, with a density of  $10^{-25} \frac{g}{cm^3}$ , in order to minimize any interactions of the  $\gamma$ -rays before leaving the world volume. Once this was completed, the  $a_2$  and  $a_4$  values were determined by fitting the data and comparing to theoretical values.

Cascade	Theoretical ( $a_2, a_4$ )	Simulated ( $a_2, a_4$ )
$0 \rightarrow 2 \rightarrow 0$	0.3571, 1.1419	0.3601(32), 1.1389(56)
$4 \rightarrow 2 \rightarrow 0$	0.1020, 0.0091	0.1028(21), 0.0089(13)
$3 \rightarrow 2 \rightarrow 0$ ( $\delta = 0$ )	-0.0714, 0.0000	0.0709(11), 0.0002(19)
$2 \rightarrow 2 \rightarrow 0$ ( $\delta = 0$ )	0.2500, 0.0000	0.2487(24), -0.0004(15)
$2 \rightarrow 2 \rightarrow 0$ ( $\delta = 1$ )	0.4527, 0.1633	0.4526(35), 0.1617(49)

Table 3.1: Comparison of theoretical angular correlation coefficients to simulated values in a near vacuum Geant4 simulation.

The value of the  $a_2$  and  $a_4$  coefficients determined in this way agree within statistical uncertainties with theoretical expectations validating the angular correlation package.

### 3.1.3 Crystal Efficiency and Corrections

The efficiency of the GRIFFIN array is measured by placing sources inside the array before and usually also after an experiment. These sources have well-known  $\gamma$ -ray energies over a wide range and generally the activity of at least one of the sources is accurately known providing an absolute efficiency calibration. Some of the most commonly used sources include  $^{60}\text{Co}$ ,  $^{56}\text{Co}$ ,  $^{152}\text{Eu}$  and  $^{133}\text{Ba}$ . These sources give a wide range of  $\gamma$ -ray energies from around 80 *keV* up to 3500 *keV*. Sometimes, in order to minimize bremsstrahlung from  $\beta$  particles creating unwanted signals in GRIFFIN, a sphere of delrin is placed just inside the array. The delrin spheres used in experiments are usually either 10*mm* or 20*mm* thick, and when in place the efficiency for low-energy  $\gamma$ -rays can be reduced significantly.

To extract these efficiencies, the  $\gamma$ -ray peaks were fit using a TPeak function in a C++ based sorting code called GRSISort [39], developed by the GRIFFIN collaboration. These efficiencies include finding an absolute efficiency defined as:

$$\epsilon_{absolute} = \frac{P_R}{P_E} \quad (3.1)$$

with  $P_R$  being the number of  $\gamma$ -ray photopeak events recorded and  $P_E$  being the number of  $\gamma$ -rays emitted. Also, a relative efficiency is used for sources where the activity of the source is unknown.

$$\epsilon_{relative} = \frac{P_R}{R_E} \quad (3.2)$$

Nucleus	$\gamma$ -ray energies ( $keV$ )	Intensity (%)
$^{56}\text{Co}$	1037	14.05 (4)
	1238	66.46 (12)
	1771	15.41 (6)
	2598	16.97 (4)
	3253	7.923 (21)
$^{60}\text{Co}$	1172	99.85 (3)
	1332	99.9826 (6)
$^{133}\text{Ba}$	81	32.9 (3)
	276	7.16 (5)
	302	18.34 (13)
	356	62.05 (15)
	383	8.94 (6)
$^{152}\text{Eu}$	121	28.53 (16)
	344	26.59 (20)
	779	12.93 (8)
	867	4.23 (3)
	964	14.51 (7)
	1408	20.87 (9)

Table 3.2: Table of  $\gamma$ -ray energies from the different sources placed inside the GRIFFIN array. The intensity values for this data set came from the National Nuclear Data Centre [38].

Here  $R_E$  is the relative number of  $\gamma$  rays of a given energy incident on the detector [40]. An absolute efficiency plot for GRIFFIN is shown in Figure 3.4. In this figure there are three efficiency curves plotted using different thickness of delrin just inside the detectors.

For angular correlations, not only do the measurements have to be corrected for the number of pairs of crystals at each opening angle in the GRIFFIN geometry, but also for the slightly different efficiencies of the crystals. The first thing to look at is the efficiency of each individual crystal as a function of the  $\gamma$ -ray energy. In Figure 3.5 it is seen that the efficiencies of different crystals can vary by  $\approx 10\%$ . Making a two-dimensional array by multiplying the efficiencies of all 4096 crystal pairs, then combining the ones at the same opening angles and dividing by the number of occurrences of each angle, the effective efficiency associated with

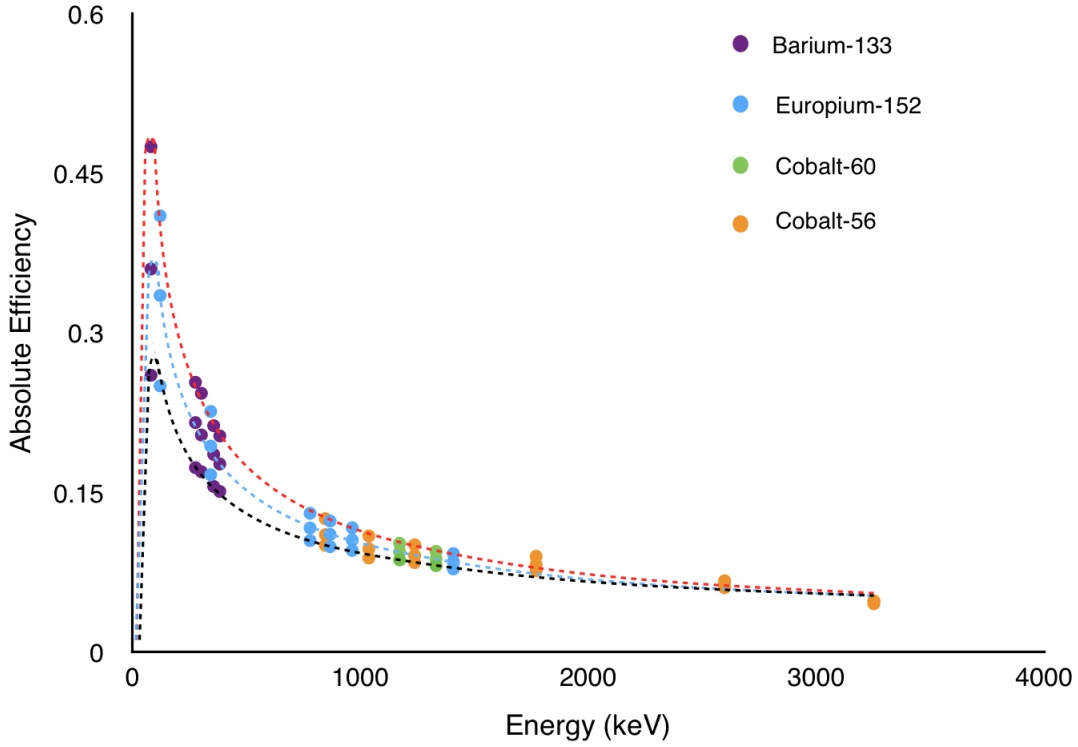


Figure 3.4: Plot of efficiencies for different sources placed inside the GRIFFIN array. The black line includes a  $20mm$  thick delrin sphere placed just inside the detectors, the blue line has a  $10mm$  thick delrin sphere and the red line has no delrin sphere. All of the efficiencies in this plot use the single crystal method, i.e. full energy deposition within a single crystal.

each opening angle can be seen and discrepancies corrected if needed.

It is seen in Figure 3.6 that the corrections, once averaged over all crystal pairs for a given opening angle, are very small, with the maximum discrepancy being approximately 1.4%. Also, once similar opening angles are grouped and the data points are folded about  $90^\circ$ , this correction factor becomes even smaller with the largest difference being about 0.9%, as shown in Figure 3.7. However, if a statistical precision of order 1% is achieved for individual angular groupings in an experiment, then adjustments must be made in order to correct for these small differences in effective efficiency.



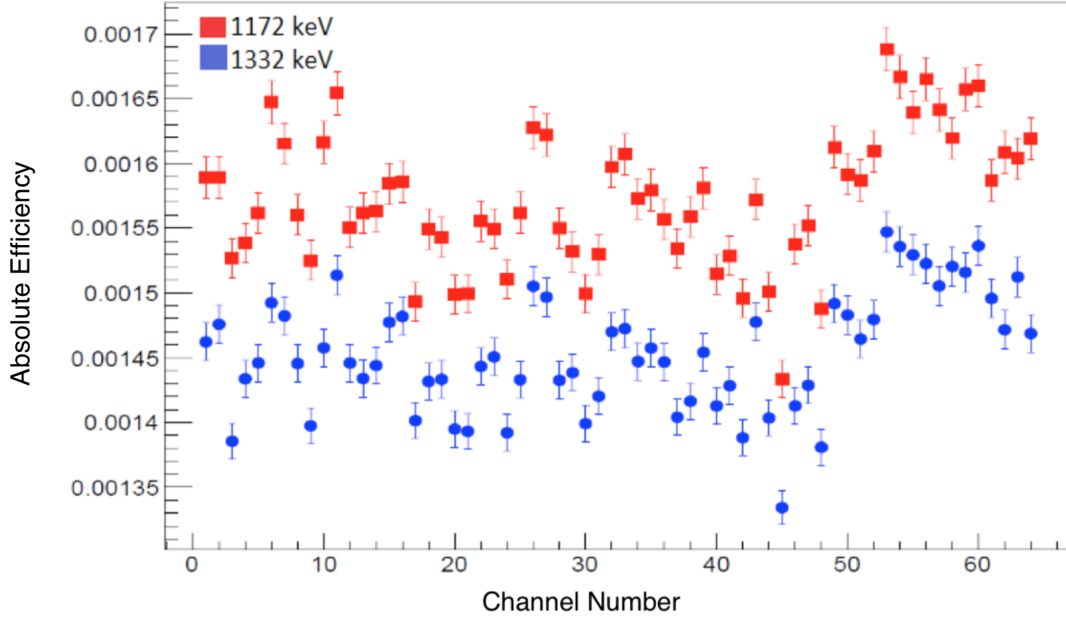


Figure 3.5: Absolute efficiencies for the 1172 *keV* (red) and 1332 *keV* (blue)  $\gamma$ -rays in  $^{60}\text{Co}$  for each of the individual HPGe crystals of GRIFFIN.

### 3.1.4 Background Subtractions

For data involving  $\gamma$ -rays, there are many sources of background. They involve the processes described in Section 2.2, as well as room background and cosmic rays. In the Geant4 simulations the room background and cosmic rays do not exist, but there is background from Compton scatters in the simulated  $\gamma$ -ray spectra. In order to remove this background, subtractions are performed on the data. In Figure 3.8, it is seen that there is a narrow gate set on the photopeak for the 1332 *keV*  $\gamma$ -ray from  $^{60}\text{Co}$  decay. There is also a wider gate set above the peak that is used to subtract the background under the 1332 *keV* peak due to Compton events from higher energy  $\gamma$ -rays. The background gate is best set above the photopeak without including any other clear  $\gamma$ -ray peaks if possible and significantly wider than the photopeak gate to limit the statistical fluctuations introduced by the background subtractions.

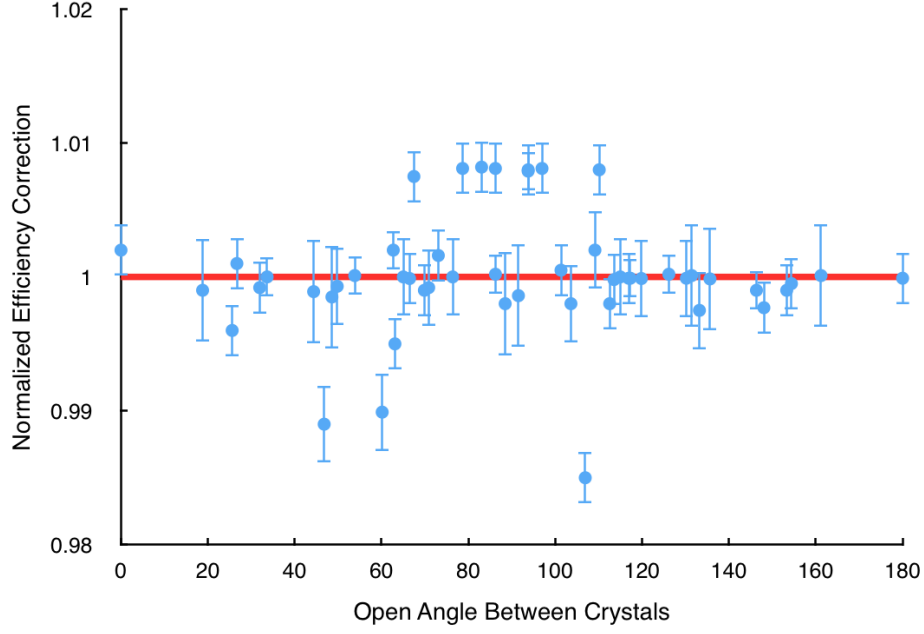


Figure 3.6: Normalized efficiency for each of the 51 opening angles between crystal pairs in the GRIFFIN array determined for the  $1.33 \text{ MeV}$   $\gamma$ -ray from  $^{60}\text{Co}$  decay.

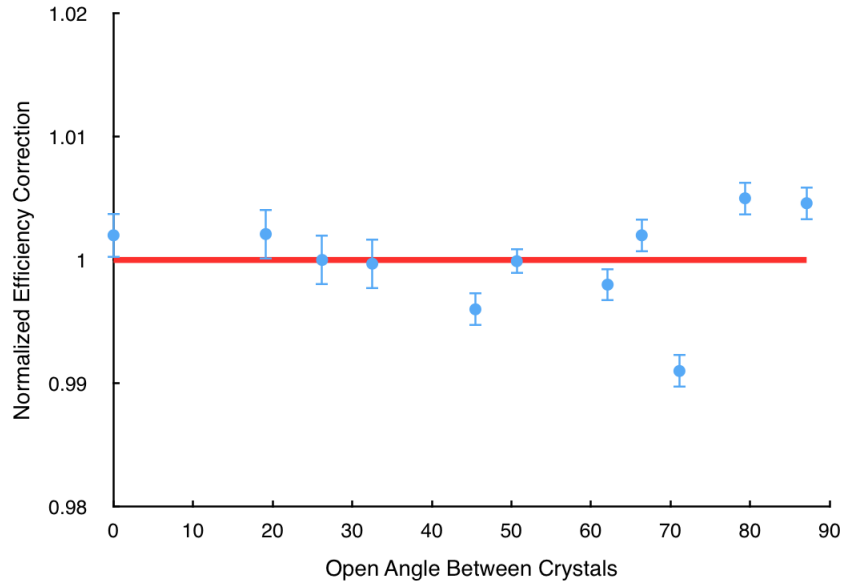


Figure 3.7: Normalized efficiency for the 11 opening angles between crystal pairs when grouped and folded together, as determined for the  $1.33 \text{ MeV}$   $\gamma$ -ray from  $^{60}\text{Co}$  decay.

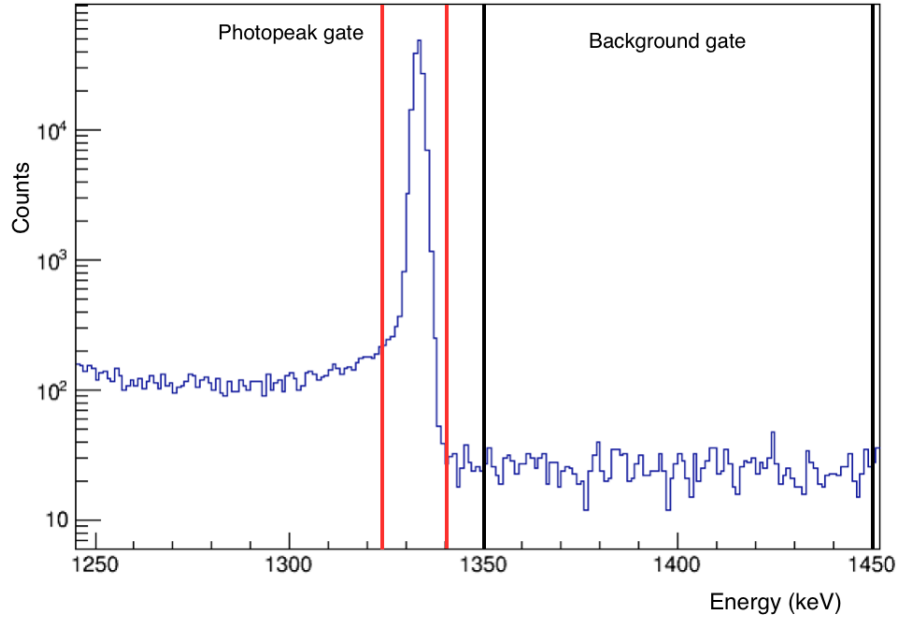


Figure 3.8: Gate set on the 1332  $keV$  photopeak (red) in  $^{60}\text{Co}$  as well as the background gate (black) set above the peak.

Leaving the Geant4 world and moving to a real experimental situation, there are also time random events. These are events that can come from room background, such as  $^{40}\text{K}$  decay that has a 1460  $keV$  peak, cosmic rays passing through the atmosphere that produce a broad spectrum of energies, or other events from the source of interest occurring at nearly the same time. Many room background peaks have been measured in different facilities and are well known and understood [41]. These events can have a wide range of energies, causing false counts in photopeaks. To exclude these events, a cut is placed on the timing of the 2  $\gamma$  rays involved in the  $\gamma - \gamma$  coincidence and background is subtracted, as shown in Figure 3.9. After normalizing the backgrounds of both Compton scattered events from higher energy  $\gamma$ -rays and from time randoms, the remaining spectrum is then considered the true events and angular correlations can be extracted.

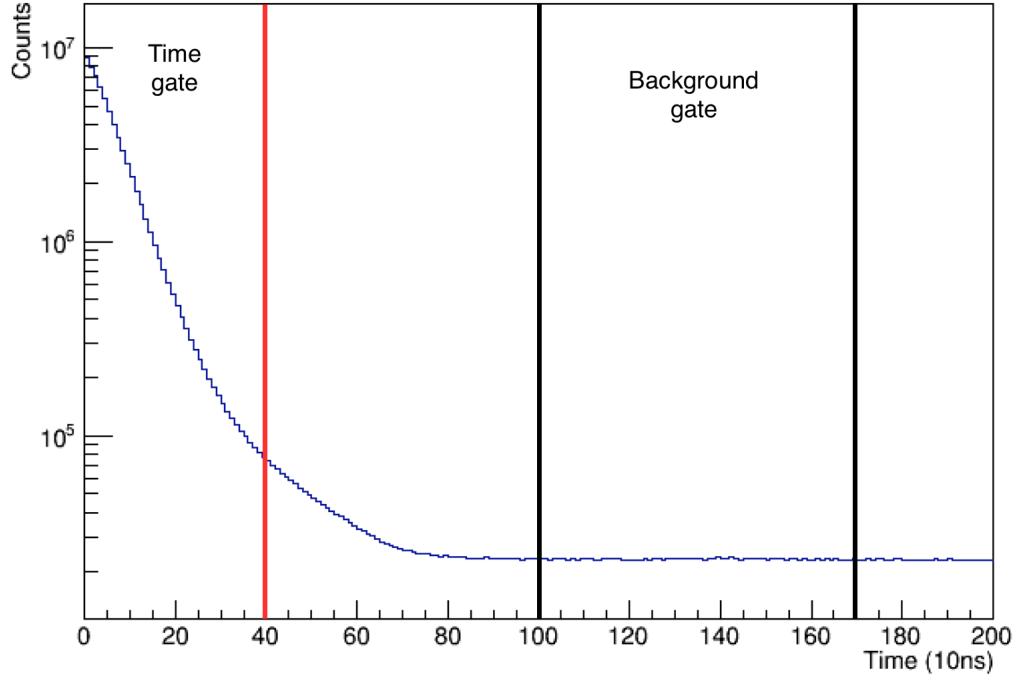


Figure 3.9: Gate set on the  $\gamma - \gamma$  time difference coincidence peak as well as the time-random background gate.

### 3.1.5 Event Mixing Technique

As mentioned in section 3.1.4, in Geant4 simulations some factors are not taken into account that may alter the experimental angular correlations. These include background from the room, cosmic rays, as well as efficiency differences between crystal pairs. In order to correct for these factors, an event mixing technique [42] was used. The event mixing technique constructs angular correlations of  $\gamma$ -rays from different events. As there is no true angular correlation between  $\gamma$ -rays from different nuclear decays, this should produce an isotropic distribution with any deviation from a flat angular correlation reflecting the bias in the instrumental response under the actual experimental conditions and involving the exact

$\gamma$  ray energies of interest. The experimental distribution can be expressed as [42]:

$$w(\theta, E_a, E_b) = \sum_{i,j}^{\theta=|\theta_i-\theta_j|} \epsilon_i(E_a)\epsilon_j(E_b, t) \int_{\theta-\Delta\theta}^{\theta+\Delta\theta} X_{ij}(\theta, E_a, E_b)W(\theta)d\theta \quad (3.3)$$

where  $w(\theta, E_a, E_b)$  is the experimental angular correlation,  $\epsilon_{i,j}$  are efficiency corrections for specific crystal pairs,  $X_{ij}$  are the weighting factors for the number of occurrences of crystal pairs and  $W(\theta)$  is the theoretical angular correlations described in Section 1.6. Thus far, the weighting factors have been taken care of in the Geant4 simulations while making the templates, and the crystal pair efficiency corrections have been shown to be small, on the order of 1%.

If a second distribution is made using mixed events, that we assume are randomly distributed spatially, and we define in a similar fashion:

$$y(\theta, E_a, E_b) = \sum_{i,j}^{\theta=|\theta_i-\theta_j|} \epsilon_i(E_a)\epsilon_j(E_b, t) \int_{\theta-\Delta\theta}^{\theta+\Delta\theta} X_{ij}(\theta, E_a, E_b)Y(\theta)d\theta, \quad (3.4)$$

both distributions are made using the same  $\gamma$ -ray energies and the timing of the events are close enough to assume detector efficiencies have not varied. Dividing the two distributions, it can be seen that the efficiency corrections will cancel out leaving:

$$\frac{w(\theta, E_a, E_b)}{y(\theta, E_a, E_b)} = \frac{\int_{\theta-\Delta\theta}^{\theta+\Delta\theta} X_{ij}(\theta, E_a, E_b)W(\theta)d\theta}{\int_{\theta-\Delta\theta}^{\theta+\Delta\theta} X_{ij}(\theta, E_a, E_b)Y(\theta)d\theta} \quad (3.5)$$

Knowing that the  $Y(\theta)$  distribution is between mixed events, it is isotropic and proportional to a constant. Also, both distributions use the same geometry and detector pairs [43]. With the use of this method, the non-uniformity of the instrumental response  $Y(\theta, E_a, E_b)$  can be

used to correct the experimental angular correlations, for direct comparison with the Geant4 generated templates  $W(\theta, E_a, E_b)$ .

### 3.1.6 Angular Correlations and Templates

The method used for distinguishing nuclear spins in this work was to build a library of Geant4 angular correlation templates for specific nuclear spin values, mixing ratios and  $\gamma$ -ray energies. With high statistic simulations, these templates are designed to be smooth curves that are made for the specific purpose of comparison between simulations and experiments using the same GRIFFIN geometry and actual  $\gamma$ -ray energies of interest. By directly comparing the angular correlation templates generated by Geant4 to experiment, the usual  $a_2$  and  $a_4$  coefficients are no longer needed as the templates provide a direct method to discriminate and assign spins to states. Also, the correction factor for the granularity of the detector is entirely included within the Geant4 templates in this approach.

The normalized templates are directly compared to the experimental data and the reduced chi squared,  $\frac{\chi^2}{\nu}$ , between the templates and experimental data is treated as a goodness-of-fit test. For cascades containing a mixing ratio,  $\delta$ , a range of mixing ratios were simulated. The mixing ratio can range from  $-\infty$  to  $\infty$ . The  $a_2$  and  $a_4$  coefficients, however, converge for large values of  $|\delta|$ , with the most interesting and drastic changes in the correlations occurring when  $-1 \leq \delta \leq 1$ .

It would be impossible to test an infinite range of values for mixing ratios, so in order to determine which values need to be tested, a plot of  $a_2$  versus  $a_4$  is made for different values of mixing ratios. In Figure 3.10 the theoretical coefficients were calculated for many mixing ratios for a  $2^+ \rightarrow 2^+ \rightarrow 0^+$  cascade. The two-dimensional plot of the  $a_2$  versus  $a_4$  values was then compared to the  $4^+ \rightarrow 2^+ \rightarrow 0^+$  cascade coefficients, as shown in Figure 3.11. This

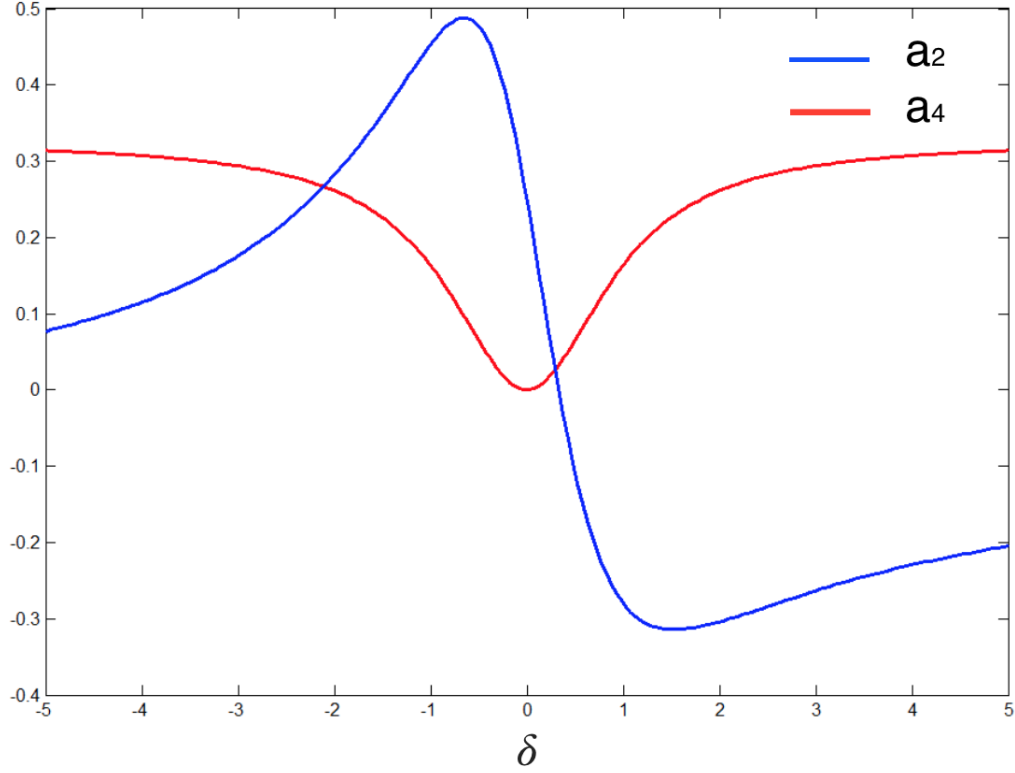


Figure 3.10: Theoretical  $a_2$  and  $a_4$  as a function the mixing ratio,  $\delta$ , for a  $2^+ \rightarrow 2^+ \rightarrow 0^+$ .

gives a good idea for the range of mixing ratios that need to be tested when attempting to distinguish a  $4^+ \rightarrow 2^+ \rightarrow 0^+$  cascade from a  $2^+ \rightarrow 2^+ \rightarrow 0^+$  cascade.

As shown in Figure 3.11, the  $2^+ \rightarrow 2^+ \rightarrow 0^+$  has almost identical  $a_2$  and  $a_4$  as a  $4^+ \rightarrow 2^+ \rightarrow 0^+$  cascade for a particular mixing ratio  $\delta \approx 0.193$ . For testing purposes, the cobalt-60 cascade was simulated for both its true  $4^+ \rightarrow 2^+ \rightarrow 0^+$  angular correlation and under the assumption of a  $2^+ \rightarrow 2^+ \rightarrow 0^+$  cascade with a range of mixing ratios around  $\delta = 0.2$ . Only a narrow range of  $\delta$  should be needed to make these two cascades distinguishable, as the theoretical coefficients change quickly around this value as seen in Figure 3.10.

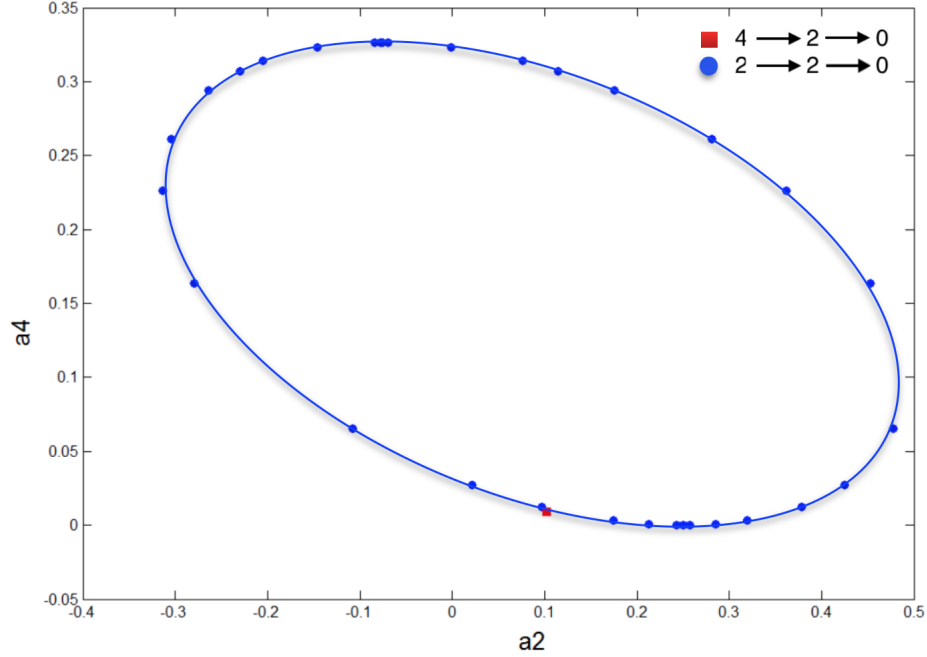


Figure 3.11: Two-dimensional plot of  $a_2$  against  $a_4$  for a  $2^+ \rightarrow 2^+ \rightarrow 0^+$  cascade with different mixing ratios. The red square is for a  $4^+ \rightarrow 2^+ \rightarrow 0^+$  cascade

### 3.1.7 Cobalt-60 Simulations

To build  $\gamma$ -ray angular correlations, first an excited state must be populated that will emit successive  $\gamma$ -rays without passing through some long-lived, isomeric state. If an intermediate state is long lived, the nucleus could change m-states and wash away the angular correlations [14]. The first data set taken for this thesis was with a  $^{60}\text{Co}$  source. This nucleus has a very well-known  $\beta^-$  decay which populates the 2.5 MeV excited  $4^+$  state in  $^{60}\text{Ni}$ , with a branching ratio of effectively 100%, which subsequently decays with the emission of 1173 and 1332 keV  $\gamma$ -rays in cascade.

After detecting  $\gamma$ -rays in cascade, the next step is to create a  $\gamma-\gamma$  energy matrix. This is a two-dimensional histogram containing the energies of the detected  $\gamma$ -rays. In Figure 3.14, a few features can be seen for the  $^{60}\text{Co}$  spectra. Most prominent are the 1.17 MeV and 1.33



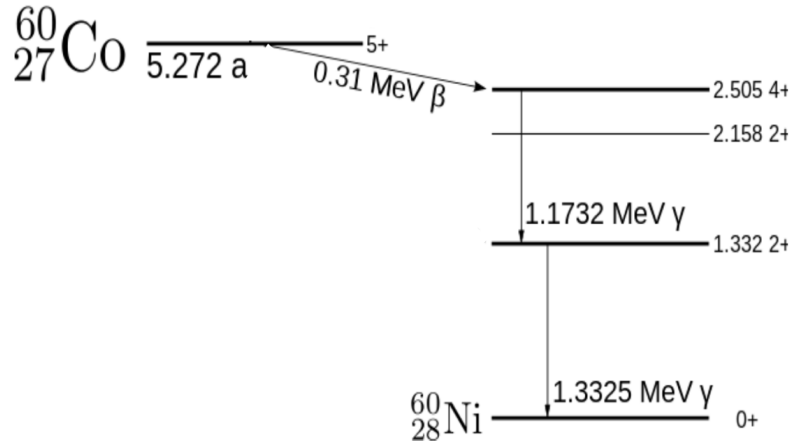


Figure 3.12: Example decay of  $^{60}\text{Co}$  to  $^{60}\text{Ni}$  excited state.

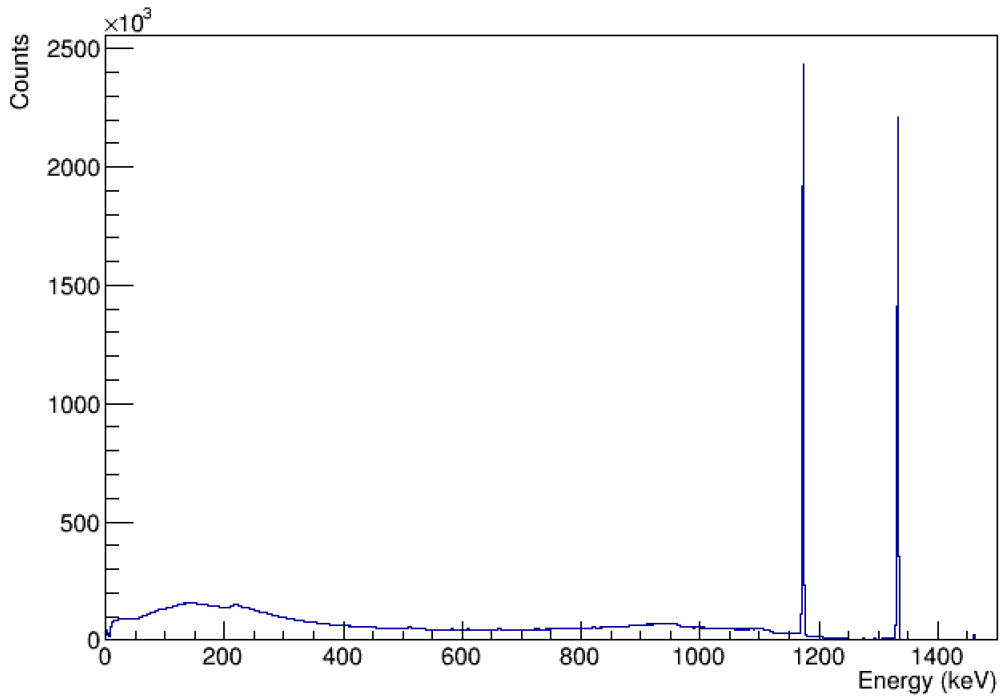


Figure 3.13: The  $\gamma$ -ray spectrum measured with individual GRIFFIN crystals following the  $\beta$  decay of  $^{60}\text{Co}$ .

*MeV*  $\gamma$  ray photopeaks. The Compton edges and Compton background can also be seen with significant scattering occurring between crystals located close together.

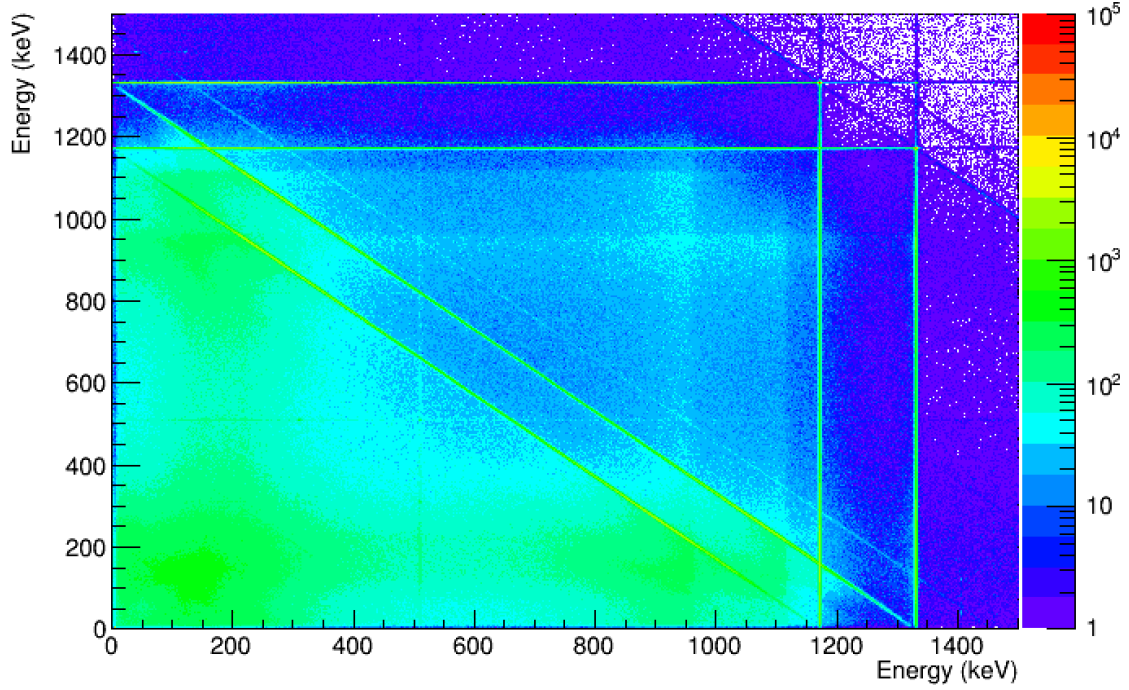


Figure 3.14: The  $\gamma$ - $\gamma$  coincidence matrix for  $^{60}\text{Co}$  with GRIFFIN operating in single crystal mode.

The next step was to take the two dimensional  $\gamma - \gamma$  coincidence matrix and expand it in the z-direction. On the z-axis was the opening angle between the crystals hit by the two  $\gamma$ -rays. This is essentially the same as creating a two-dimensional  $\gamma - \gamma$  coincidence matrix for each of the 51 distinct opening angles of the detector geometry. In Figure 3.15 the features previously described are visible. Most of the scattering events are seen to occur at low opening angles in the array, meaning crystals in close proximity. The key information for the correlations exists in the vertical columns seen at the two photopeak energies.

With this three-dimensional histogram the projection is taken gating on the higher energy  $\gamma$ -ray, in this case  $1.33 \text{ MeV}$ . This projection is made for each opening angle in GRIFFIN. In coincidence with the  $1.33 \text{ MeV}$  should be the  $1.17 \text{ MeV}$  photopeak found in the  $^{60}\text{Co}$  decay scheme. Fitting the  $1173 \text{ keV}$  peak in the  $1.33 \text{ MeV}$  coincidence gated spectrum,

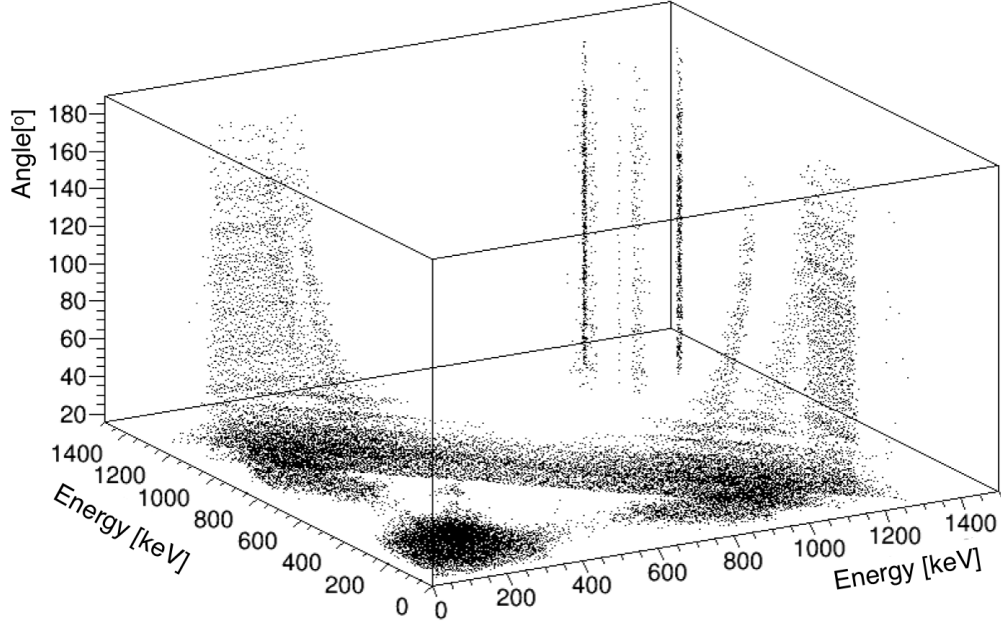


Figure 3.15: The  $\gamma$ - $\gamma$  coincidence matrix with the single crystal method expanded along the z-axis giving the opening angle between the two crystals that the  $\gamma$ -rays were detected in GRIFFIN.

as shown in Figure 3.16, we can extract the coincidence counts for each angle. In order to find the total counts in the peak, the fit curve was integrated. Performing the background subtraction, described in Section 3.1.4, and normalizing for the weighting factor for each opening angle gives the angular correlation of the two  $^{60}\text{Co}$   $\gamma$ -rays shown in Figure 3.17.

In this correlation there is no data point at the  $\theta = 0$ ,  $\cos\theta = 1$ , location. This data point requires both  $\gamma$ -rays to deposit their full energy in a single crystal, resulting in a sum peak in the  $\gamma$ -ray singles spectra. If a transition occurs naturally in the decay, creating a single  $\gamma$ -ray with the energy of the sum peak, it must be accounted for to distinguish the two contributions. For the purpose of this work, the sum peak was not included in the angular correlation analysis.

It is important to remember that these correlations are symmetric about  $90^\circ$  and contain

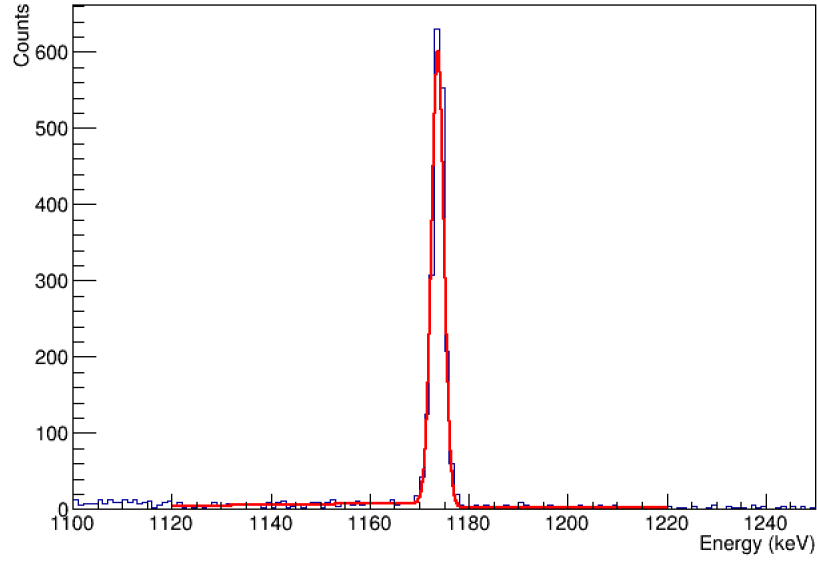


Figure 3.16:  $\gamma$ -ray spectrum gated on the 1.33  $MeV$   $\gamma$ -ray and fitting the 1.17  $MeV$   $\gamma$ -ray in coincidence. These data were for a particular opening angle of  $60.15^\circ$  between the two detectors

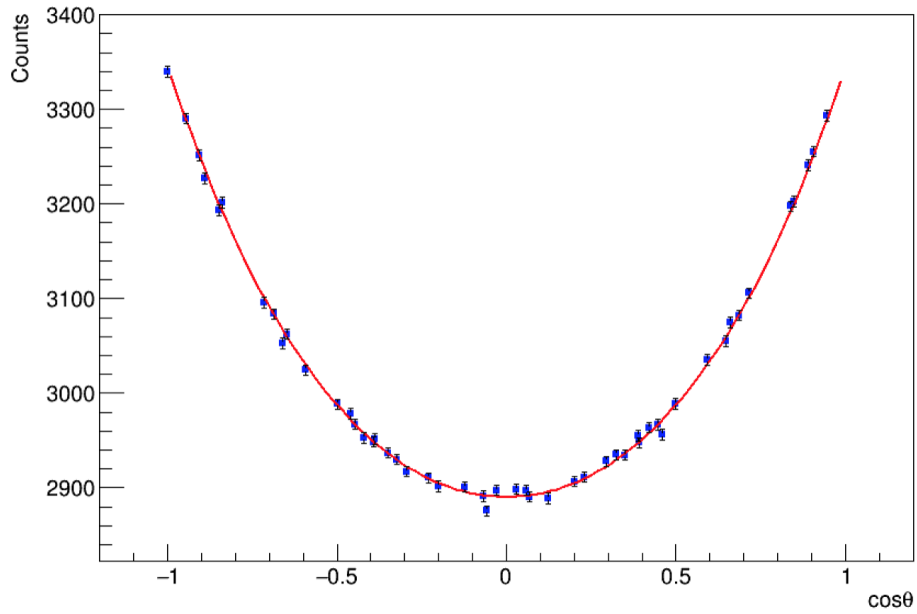


Figure 3.17:  $10^9$  simulated events for the angular correlation of the  $4^+ \rightarrow 2^+ \rightarrow 0^+$  cascade in  $^{60}\text{Co}$ , including all 51 distinct opening angles in the GRIFFIN geometry.

opening angle groups that are close together. Because of this, grouping similar angles and folding the data about  $90^\circ$  can improve the statistical precision within individual opening angle bins, as shown in Figure 3.18.

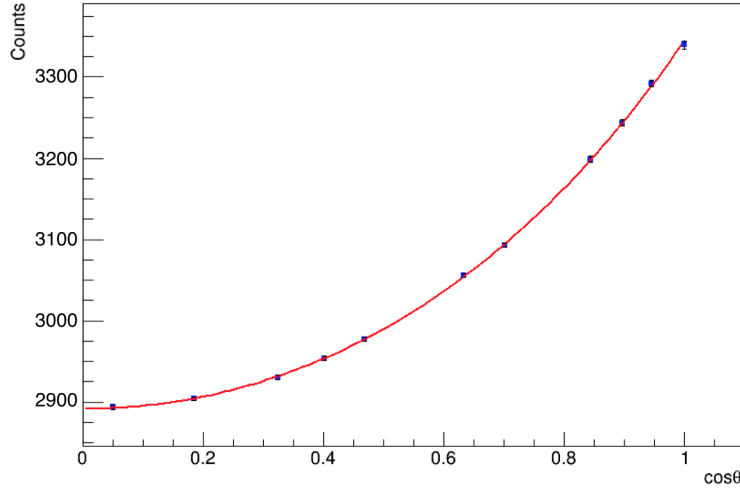


Figure 3.18: The  $\gamma - \gamma$  angular correlation template for the  $4^+ \rightarrow 2^+ \rightarrow 0^+$  cascade in  $^{60}\text{Co}$  after grouping similar angles and folding the data about  $90^\circ$ .

The choice of how to group angles is subjective. This thesis uses a grouping method that was designed to allow for the statistical weighting to be as close to uniform as possible, as described in Section 2.3.1.

For cascades where there is the possibility of mixing, E2/M1 for example, as in the first transition of a  $2^+ \rightarrow 2^+ \rightarrow 0^+$  cascade, a variety of mixing ratios must be considered to view the differences created in the shape of the angular correlations. The mixing ratios used for the creation of templates were decided upon with the help of Figure 3.11.

The angular correlation shown in Figure 3.20 is one of significant importance as it is extremely similar to the  $4^+ \rightarrow 2^+ \rightarrow 0^+$  from the  $^{60}\text{Co}$  decay.

Templates were constructed for cascades involving states of varying spins and transitions with a range of mixing ratios. In Figures 3.19, 3.20, 3.21 the angular correlations are shown

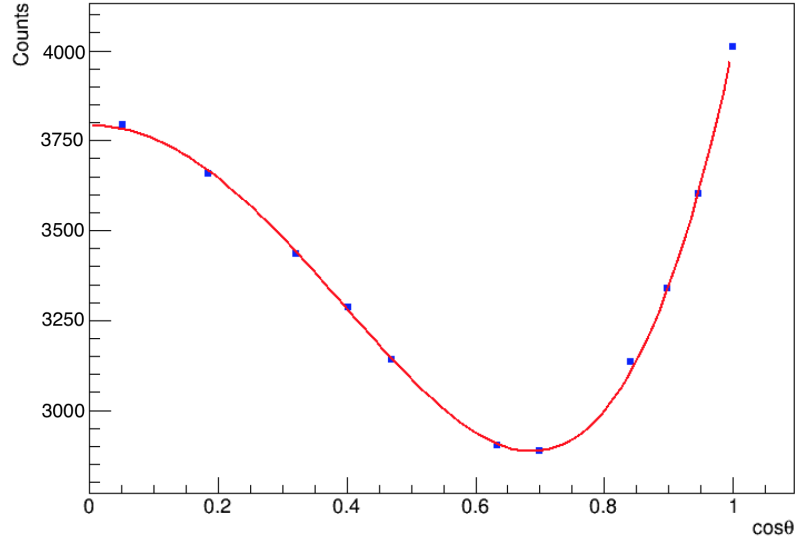


Figure 3.19: High statistics simulation used to produced a template for a hypothetical  $2^+ \rightarrow 2^+ \rightarrow 0^+$  cascade in  $^{60}\text{Co}$  decay with  $\delta = -10$ .

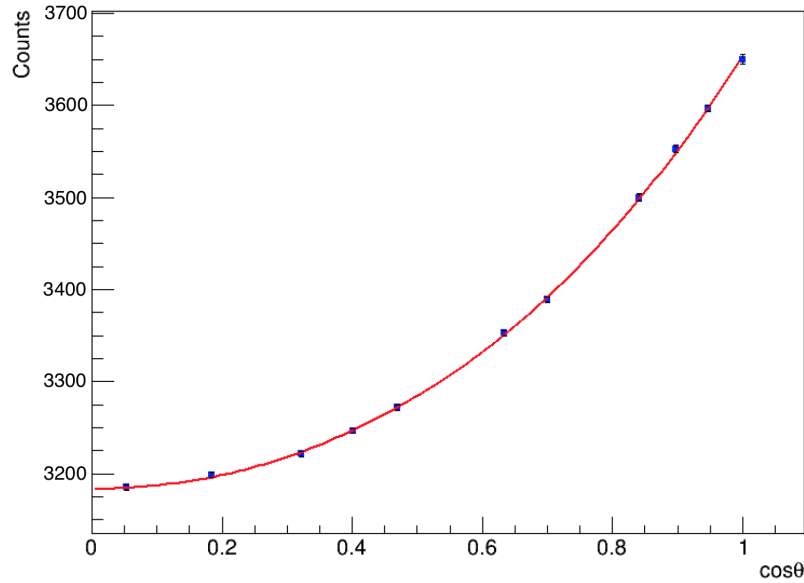


Figure 3.20: High statistics simulation used to produced a template for a hypothetical  $2^+ \rightarrow 2^+ \rightarrow 0^+$  cascade in  $^{60}\text{Co}$  decay with  $\delta = 0.2$ .

for hypothetical  $2^+ \rightarrow 2^+ \rightarrow 0^+$  cascades with  $\gamma$ -ray energies in the  $^{60}\text{Co}$  decay and different mixing ratios. The differences in shape are easily visible. Once all of the templates were

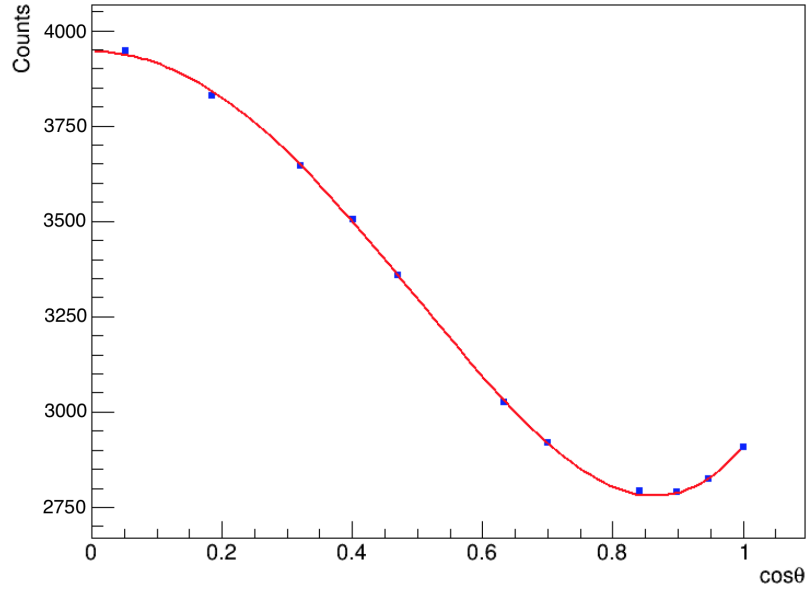


Figure 3.21: High statistics simulation used to produced a template for a hypothetical  $2^+ \rightarrow 2^+ \rightarrow 0^+$  cascade in  $^{60}\text{Co}$  decay with  $\delta = 1$ .

created, they were compared to an experimental data set in order to explore the sensitivity of GRIFFIN to these different angular correlations.

### 3.1.8 Addback

All of the previous work has been carried out assuming full energy deposition of the  $\gamma$ -ray in a single crystal. For the  $\gamma$ -ray energies from  $^{60}\text{Co}$  decay,  $1.17 \text{ MeV}$  and  $1.33 \text{ MeV}$ , this yields approximate absolute detection efficiencies of 10% and 9% respectively. If instead of considering energies deposited in single crystals, the energies deposited in all of the crystals in a clover detector are added together, known as clover addback, photopeak efficiencies are increased to approximately 13% and 11%, respectively. When crystals are added together, however, there is a loss in the angular resolution. Therefore, choosing an optimal method of addback becomes a balance of gaining photopeak efficiency and losing angular resolution.

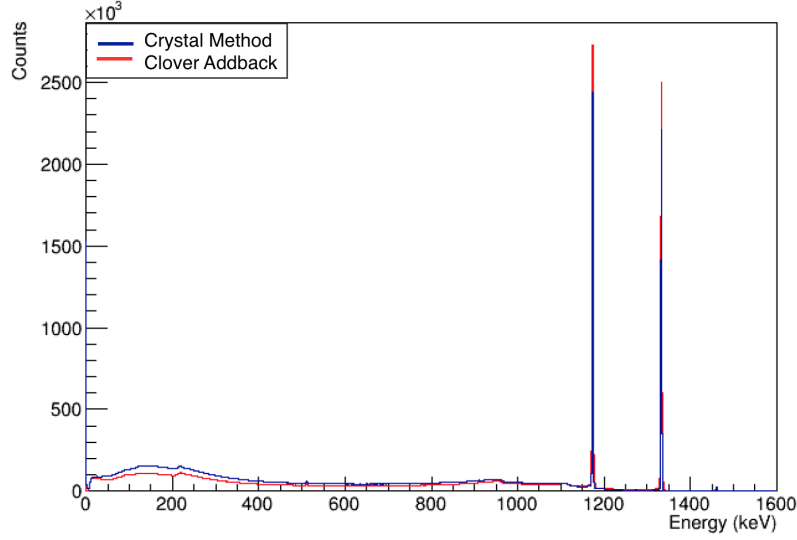


Figure 3.22:  $\gamma$ -ray spectrum from  $^{60}\text{Co}$  decay with single crystal method in blue and clover addback in red.

In Figure 3.22, a spectrum from  $^{60}\text{Co}$  is seen with the red histogram being with addback and the blue histogram being for the single crystal method. As previously mentioned, the addback mode has more counts in the photopeak, i.e. a greater efficiency. Of course, those counts had to originate from somewhere in the single crystal spectra, so as a bonus, the amount of Compton background is decreased. For complicated spectra with many peaks, this background reduction is important as the Compton background from higher energy  $\gamma$ -rays can hide low-energy photopeaks. Looking more closely at the 1.33  $\text{MeV}$   $\gamma$ -ray, the gain in photopeak efficiency becomes quite apparent, as shown in Figure 3.23. It is also important to note that the width of the peak grows slightly, due to the larger noise contribution when adding energies from more than one crystal and implying that energy gates have to be wider.

Comparing Figures 3.14 with 3.24, the most visible attribute is the vast reduction in Compton background as well as the scatter peaks. This same comparison can be made between Figures 3.25 and 3.15, as the low angle scattering is greatly reduced with only



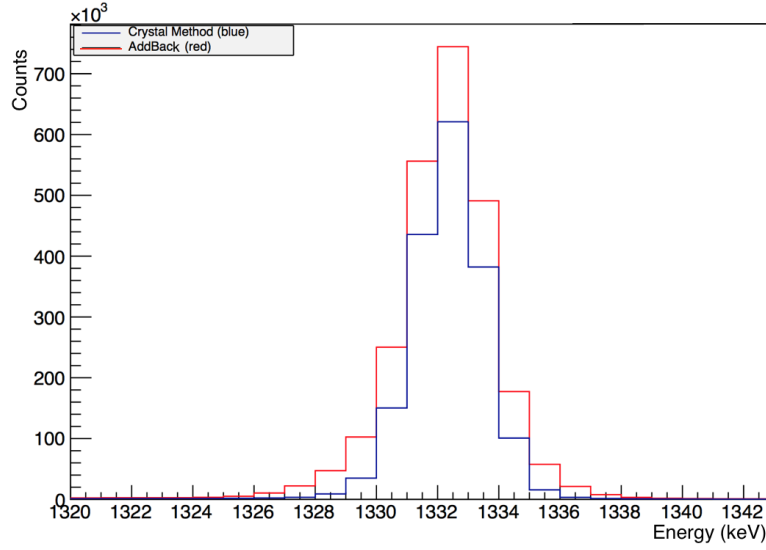


Figure 3.23:  $^{60}\text{Co}$   $\gamma$ -ray spectrum zoomed in on the 1332.5 keV photopeak to see the gain in photopeak efficiency.

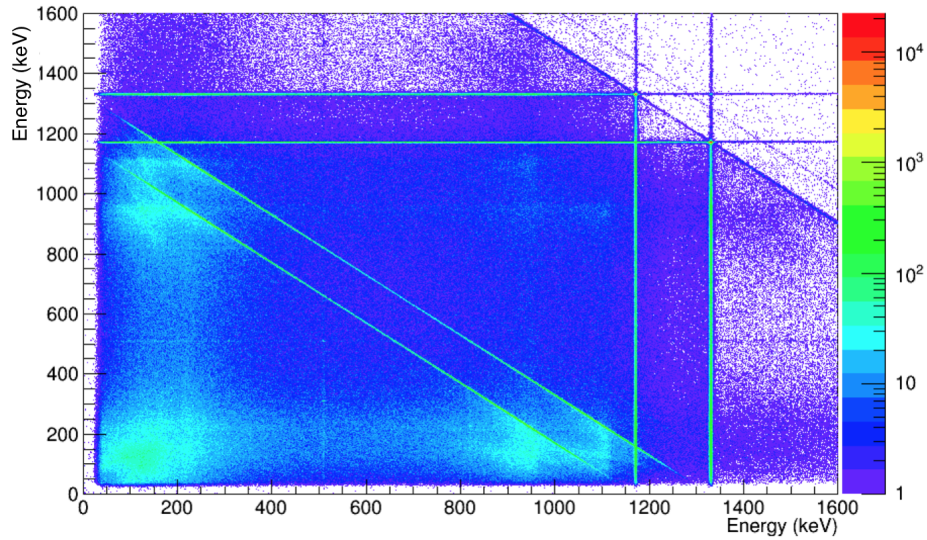


Figure 3.24: The  $\gamma$ - $\gamma$  coincidence matrix for  $^{60}\text{Co}$  decay using clover addback.

scattering events between crystals from neighbouring detectors visible. Despite this gain in efficiency and the reduction of background with addback, the loss of angular resolution is a concern and it becomes important to test both methods in order to determine which is

better suited for the measurement of angular correlations and the assignment of spins to excited nuclear states.

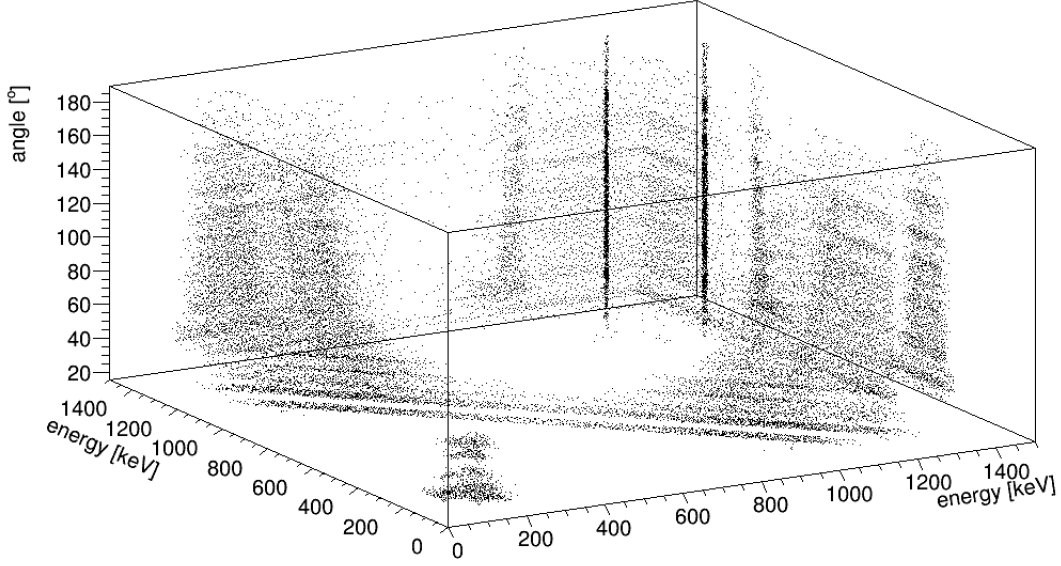


Figure 3.25: The  $\gamma$ - $\gamma$  coincidence matrix for  $^{60}\text{Co}$  decay with the clover addback method expanded along the z-axis with respect to the opening angle between two GRIFFIN detectors.

### 3.1.9 Spin Assignments

Once all the high-statistics templates were created with Geant4, they were fit with the  $W(\theta)$  function (see Section 1.6) using a least squares method. The fits from these templates were then compared firstly to lower-statistics Geant4 simulated experiments, and then later to actual experimental data collected with GRIFFIN. The approach used to determine a goodness-of-fit test between the template and the data was the  $\chi^2$  statistic:

$$\chi^2 = \sum_i^n \frac{(O_i - E_i)^2}{\sigma_i^2} \quad (3.6)$$

where  $O_i$  is the low-statistics experimental or simulated data point,  $E_i$  is the high-statistics template value and  $\sigma_i$  is the combined error from both. With these templates having such high-statistics relative to the low-statistics simulated experiments the error in the template is much less than the error in the low-statistics data point.

When making the  $\gamma - \gamma$  angular correlation measurements a comparison of single crystal and clover addback methods was examined. For the  $4^+ \rightarrow 2^+ \rightarrow 0^+$  cascade in  $^{60}\text{Co}$  decay both give similar results, with the single crystal method having a  $\chi^2/\nu = 0.97$  and the clover addback method  $\chi^2/\nu = 0.94$ . These are shown in Figure 3.26 and 3.27, respectively. For the  $2^+ \rightarrow 2^+ \rightarrow 0^+$  cascade a similar trend is seen at the minima near  $\delta = 0.19$ . Moving away from the minima, the  $\chi^2/\nu$  plots retain similar shapes, but with the more counts in the photopeak addback has smaller relative errors than the single crystal method. This smaller error increases the  $\chi^2$ , and hence the  $\chi^2/\nu$ , giving more sensitivity for the measurements of the mixing ratios in the addback method.

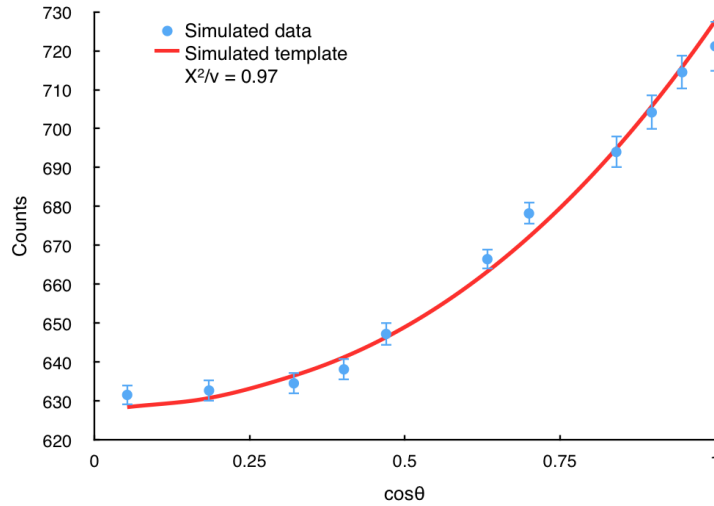


Figure 3.26: Angular correlations with single crystal method for the  $4^+ \rightarrow 2^+ \rightarrow 0^+$  cascade in the  $^{60}\text{Co}$  decay with Geant4.

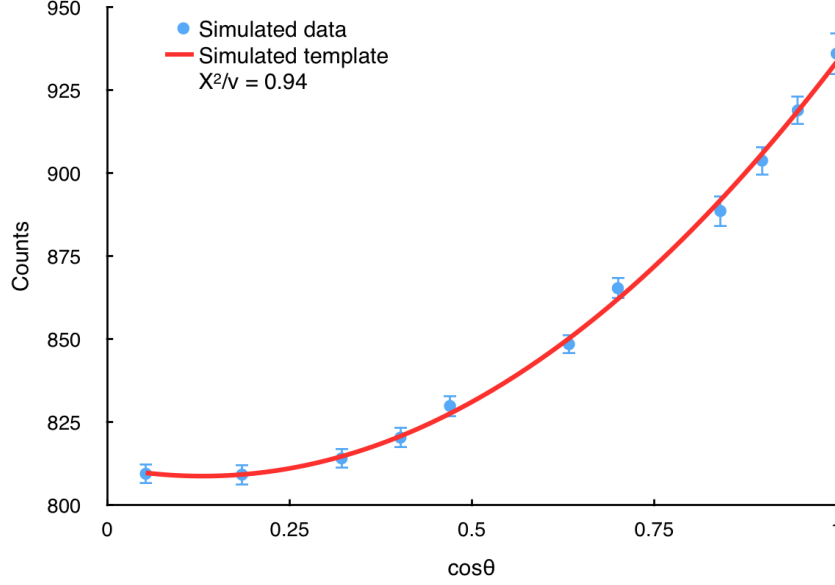


Figure 3.27: Angular correlations with clover addback method for the  $4^+ \rightarrow 2^+ \rightarrow 0^+$  cascade in the  $^{60}\text{Co}$  decay with Geant4.

Dividing the  $\chi^2$  by the number of degrees of freedom,  $\nu$ , given by the number of data points minus one to account for the overall normalization of the template the data, produces the reduced chi squared,  $\frac{\chi^2}{\nu}$ . Figure 3.28 shows results from a simulated experiment for the  $4^+ \rightarrow 2^+ \rightarrow 0^+$  cascade in  $^{60}\text{Co}$  produced by Geant4 compared to the high-statistics templates. In this plot the data set was produced and analyzed using single crystal and clover addback methods. For clover addback, the crystal with the highest energy deposited was assumed to be the first interaction site, and is used as the crystal location for generating the opening angles. The two methods produce similar results in comparison to the  $2 \rightarrow 2 \rightarrow 0$  templates for mixing ratios close to the minima, but the addback method has a slightly narrower minimum, making it a more sensitive option. The advantage with addback is more obvious when looking at other hypothetical cascades such as  $0 \rightarrow 2 \rightarrow 0$  and  $3 \rightarrow 2 \rightarrow 0$ , for which addback gives a much larger  $\chi^2/\nu$  and hence greater discrimination from the actual  $4 \rightarrow 2 \rightarrow 0$

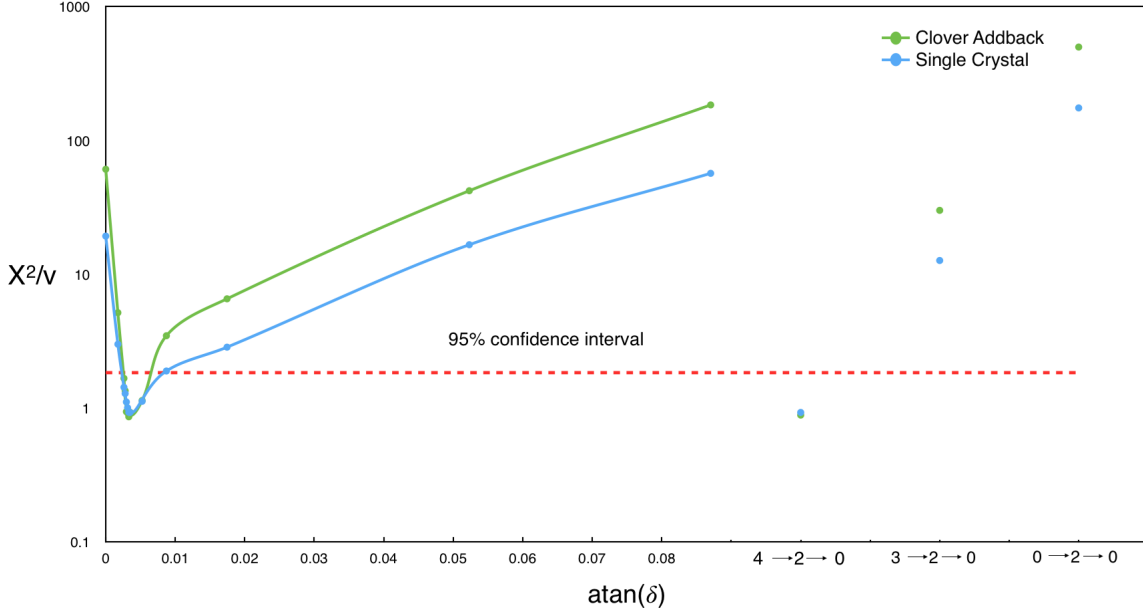


Figure 3.28:  $\chi^2/\nu$  versus  $\text{atan}(\delta)$ . The  $2^+ \rightarrow 2^+ \rightarrow 0^+$  cascade uses a range of mixing ratios while the other cascades either have no mixing or the mixing was considered zero.

cascade. In this particular case of a  $4 \rightarrow 2 \rightarrow 0$  cascade, we have not been able to assign a definitive spin from the angular correlations alone due to the effective degeneracy with a  $2 \rightarrow 2 \rightarrow 0$  cascade with  $\delta = 0.19$ . As this occurs at a finite mixing ratio, the first transition of the  $2^+ \rightarrow 2^+ \rightarrow 0^+$  cascade would have a mixture of magnetic (M1) and electric (E2) character and could, in principle, be separated from a  $4^+ \rightarrow 2^+ \rightarrow 0^+$  (pure E2-E2) cascade by using the clover structure of GRIFFIN to act as a polarimeter to investigate the polarization of the Compton events scattering between crystals.

## 3.2 Experimental Data

In order to test the angular correlation techniques developed through Geant4 simulations, experimental data were collected with a long-lived  $^{60}\text{Co}$  source and radioactive beams of  $^{66}\text{Ga}$

and  $^{62}\text{Ga}$ . These data sets will be discussed in terms of motivations and how each data set was collected and analyzed. Each data set has important characteristics allowing the capabilities of GRIFFIN to be tested and compared to simulation. Using the methods described in the previous sections, spin and parity assignments will be discussed.

### 3.2.1 Gain Matching

Data was collected individually from each crystal when the energy deposited exceeded a  $\sim 50\text{ keV}$  threshold. The HPGe crystals, which are semiconductor diodes, each have a reverse bias voltage applied that allows for the charge carriers to be collected after a  $\gamma$ -ray deposits energy in the crystal. Charge sensitive preamplifiers convert the charge collected to a voltage signal that is digitized 100 million times a second by a  $100\text{ MHz}$  analog-to-digital converter (ADC). To ensure all channels produce the correct energy for photopeaks, the ADCs must be gain matched. In a gain-matched ADC each channel has been adjusted so the same ADC channel corresponds to the same energy deposited in the crystal. Using well known peaks from sources such as  $^{60}\text{Co}$  and  $^{152}\text{Eu}$ , the gain matching was done on a crystal-by-crystal basis to match the ADC channel numbers with the well-known peak energies. Once gain matched properly at two energies, the array should produce reasonably calibrated results for other energies due to the linearity of the ADC response. When looking at cascades with GRIFFIN, it is usually a good idea to gain match on the peaks involved in the cascade after the initial gain match to one of the sources.

Dealing specifically with  $^{60}\text{Co}$  as an example, before the data were gain matched, it can be seen in Figure 3.29 that the photopeaks are staggered for each crystal. These data would be extremely difficult to work with as the energy of the peak is not consistent. If it were a complicated spectra, discerning peaks would not be a trivial task.

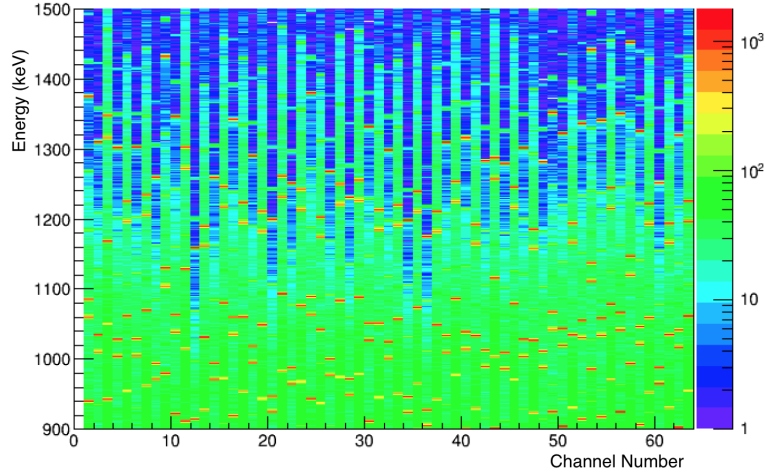


Figure 3.29:  $^{60}\text{Co}$  data showing 1172 and 1332 keV photopeaks for each crystal of GRIFFIN not gain matched.

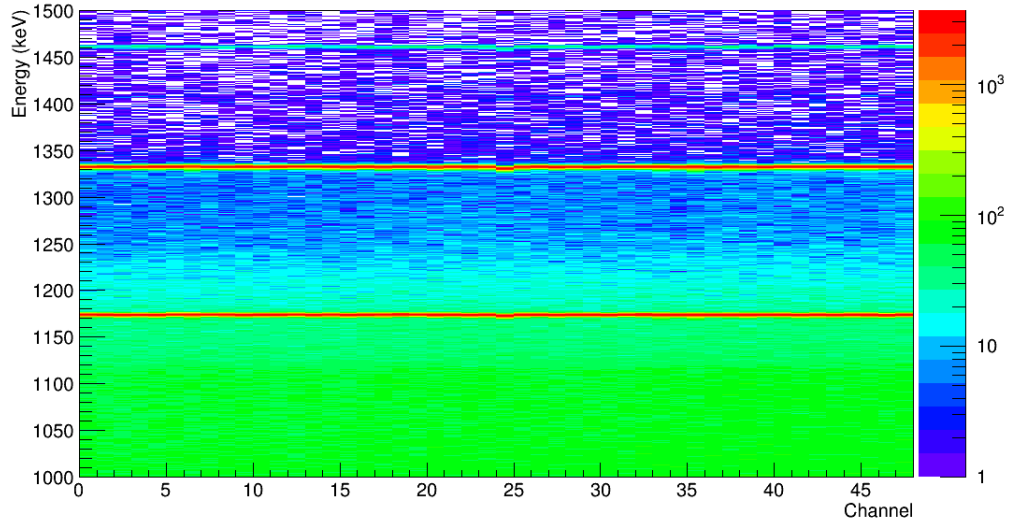


Figure 3.30:  $^{60}\text{Co}$  data showing 1172 and 1332 keV photopeaks for each crystal of GRIFFIN after gain matching.

In Figure 3.30 the gain-matched spectrum for  $^{60}\text{Co}$  is shown with the 1.17 *MeV* and 1.33 *MeV* photopeaks. Also seen in this image is the background line from potassium-40,  $^{40}\text{K}$ , which corresponds to an energy of 1.46 *MeV*. With the data properly gain matched and peaks located at their proper energies, it is now possible to look at coincidences by setting

energy gates on  $\gamma$ -rays across all crystals.

### 3.2.2 $^{60}\text{Co}$ Source Data

The  $^{60}\text{Co}$  source data for this analysis was taken as a baseline in order to measure the sensitivity of GRIFFIN to angular correlations. This decay has effectively a 100% branch to the 2505  $keV$   $4^+$  excited state of  $^{60}\text{Ni}$ , which then decays via two  $\gamma$ -rays to the ground state. As previously mentioned, this is a well known  $4^+ \rightarrow 2^+ \rightarrow 0^+$  cascade with both transitions being electric quadrupole (E2) transitions. The first requirement is the need to demonstrate that both  $\gamma$ -rays in this decay, being 1172  $keV$  and 1332  $keV$ , are actually detected in coincidence with GRIFFIN. The  $\gamma$ -ray spectrum in Figure 3.31 shows that the two photopeaks are clearly visible. A small peak at 511  $keV$  is also visible which corresponds to  $\gamma$ -rays produced by annihilation reactions.

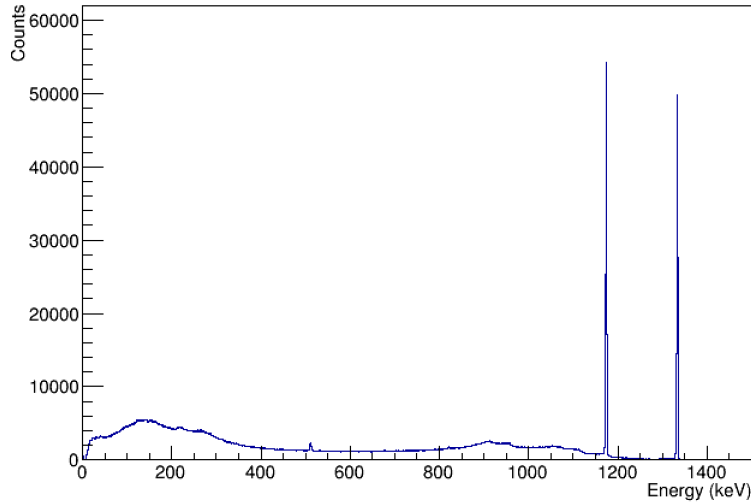


Figure 3.31:  $\gamma$ -ray spectrum for a  $^{60}\text{Co}$  source inside GRIFFIN.

Following the procedures discussed in the previous section, a  $\gamma$ - $\gamma$  matrix was constructed



for coincidence events that fall within a 400 *ns* time window. Also constructed were  $\gamma$ - $\gamma$  matrices for uncorrelated  $\gamma$ -rays from different events and  $\gamma - \gamma$  matrices gated on the time random background. Once the matrices were produced for all 51 opening angles in

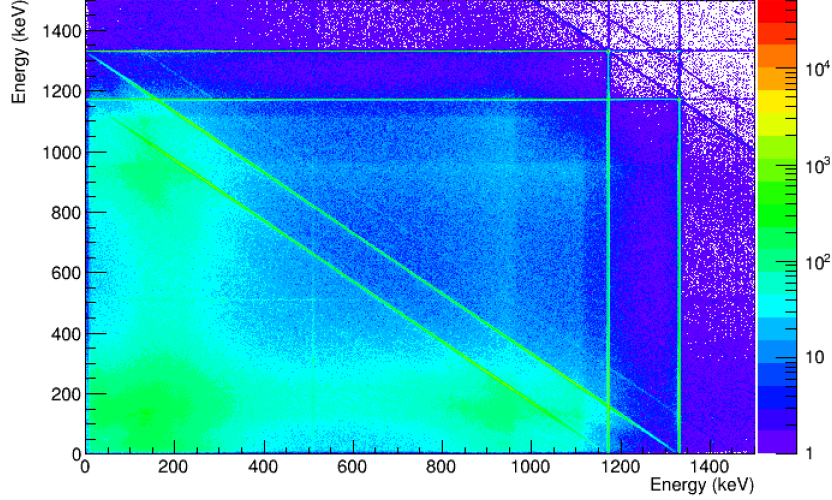


Figure 3.32:  $\gamma$ - $\gamma$  matrix for a  $^{60}\text{Co}$  source inside GRIFFIN.

GRIFFIN, the time-random background was subtracted from the original matrix in order to obtain the true coincidences from the source. A gate was set above the 1332 *keV* photopeak to produce a spectrum in coincidence with the Compton background as shown in Figure 3.33 on the left, and using mixed events an uncorrelated  $\gamma$ -ray spectrum as shown in Figure 3.33 on the right. It is desirable to have many events in the uncorrelated  $\gamma - \gamma$  data in order to have the angular correlation appear as close to flat (isotropic) as possible. In Figure 3.34, the uncorrelated events are seen to have a flat distribution, as expected. These mixed events should account for any efficiency corrections between crystals as discussed in equations 3.3 to 3.5. They should also account for any geometric differences between simulation and experiment (considered to be quite negligible). Thus, after this correction is applied, the angular correlation should give the same solution as generated by the simulation, in which

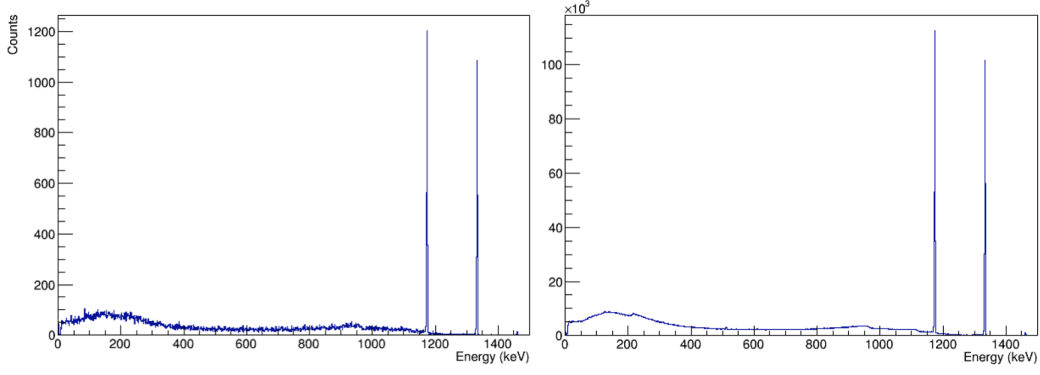


Figure 3.33:  $\gamma$ -ray spectrum for a  $^{60}\text{Co}$  source gated on the Compton background above the 1.33 MeV photopeak (left) and the uncorrelated  $\gamma$ -rays from different events (right).

all crystals were of the same geometry and thus had identical efficiencies.

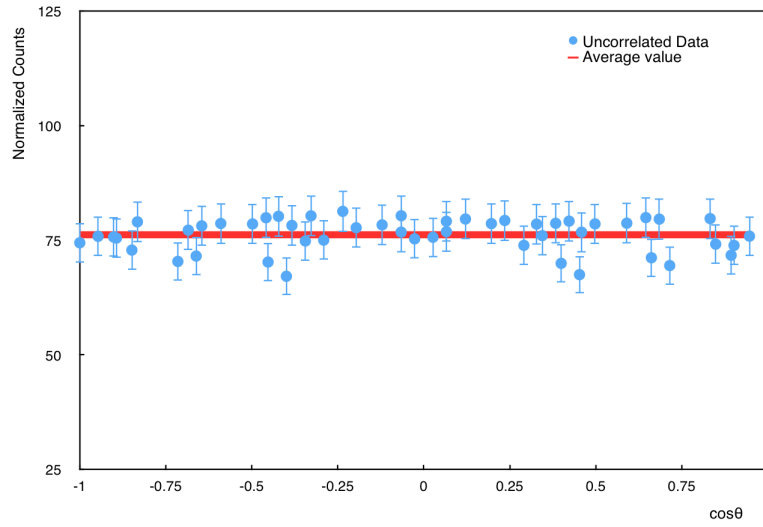


Figure 3.34: The angular correlation from the event-mixed data which is expected to be isotropic.

Finally, the experimental angular correlations were extracted and compared with the Geant4 template for a  $4^+ \rightarrow 2^+ \rightarrow 0^+$  cascade. Using the goodness-of-fit test to compare the template and the data, an extracted  $\chi^2/\nu = 0.93$  was determined. The simulated template and the experimental data are in excellent agreement, as shown in Figure 3.35.

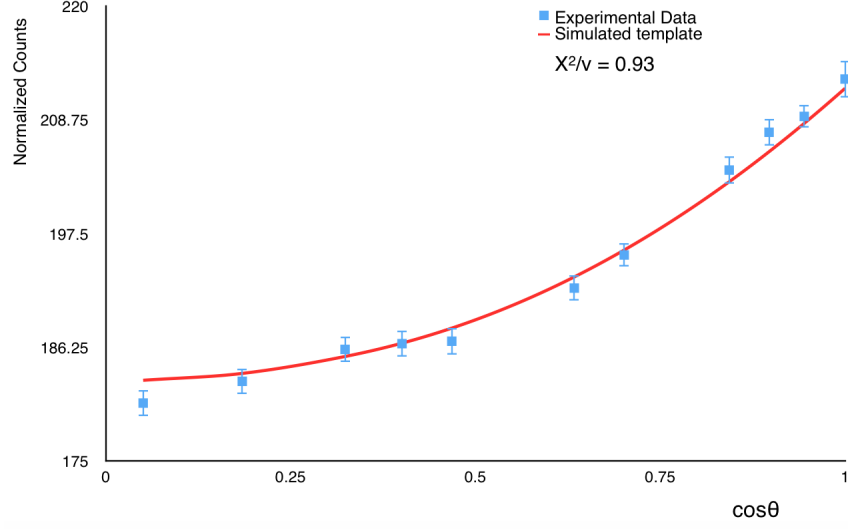


Figure 3.35: Experimental angular correlation measured for  $^{60}\text{Co}$  with all background subtractions and using the efficiency corrections from the event-mixing technique.

To ensure that other cascades do not also present good agreement with the data, many other templates were compared to the measured angular correlation. For a  $2^+ \rightarrow 2^+ \rightarrow 0^+$  cascade a wide range of mixing ratios were simulated in the vicinity of the degeneracy seen in Figure 3.11.

In Figure 3.36, which uses clover addback, when the mixing ratio has a value of  $\delta = 0.18(1)$  the  $2^+ \rightarrow 2^+ \rightarrow 0^+$  cascade cannot be distinguished from a  $4^+ \rightarrow 2^+ \rightarrow 0^+$  cascade strictly with the use of angular correlations. This is completely consistent with the result found using the simulated  $^{60}\text{Co}$  decay. Again, the next step can be to look at the polarization of the  $\gamma$ -rays in order to determine if the transition is purely an E2 or a mixed E2/M1 transition. With the use of the Klein-Nishina formula this will be studied further in the future by using the GRIFFIN clovers as Compton polarimeters to detect the  $\gamma$ -rays scattering between neighbouring crystals.

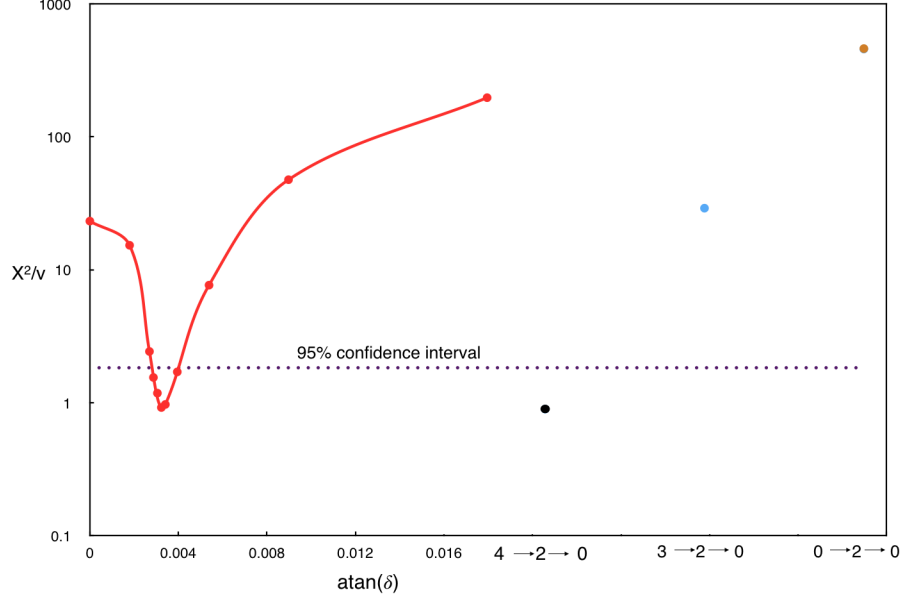


Figure 3.36:  $\chi^2/\nu$  versus  $\text{atan}(\delta)$  for experimental  $^{60}\text{Co}$  data with a range of mixing ratios used for the  $2^+ \rightarrow 2^+ \rightarrow 0^+$  cascade (red), and individual points for the  $4^+ \rightarrow 2^+ \rightarrow 0^+$ ,  $3^+ \rightarrow 2^+ \rightarrow 0^+$  and  $0^+ \rightarrow 2^+ \rightarrow 0^+$  cascades.

### 3.2.3 $^{66}\text{Ga}$ Source Data

With the angular correlation methodology established, a radioactive beam of  $^{66}\text{Ga}$  was used in order to look at cascades involving different nuclear spins and mixing ratios. With a  $\beta$ -decay Q-value of  $5.2 \text{ MeV}$ , a wide range of  $\gamma$ -ray energies from the population of many different excited states in the daughter nucleus  $^{66}\text{Zn}$  are emitted following  $^{66}\text{Ga}$   $\beta^+/\text{EC}$  decay.  $^{66}\text{Ga}$ , having a half-life of 9.5 hours, was used to create a source at the centre of GRIFFIN by implanting the radioactive beam on the aluminized mylar tape system. With a beam rate of  $9 \times 10^8/\text{s}$ , only a short implantation time of a few seconds was required. After this, the source was allowed to decay for five days, or about 12.5 half-lives.

One of the correlations studied was the 1333-1039  $\text{keV}$  cascade, which is a known

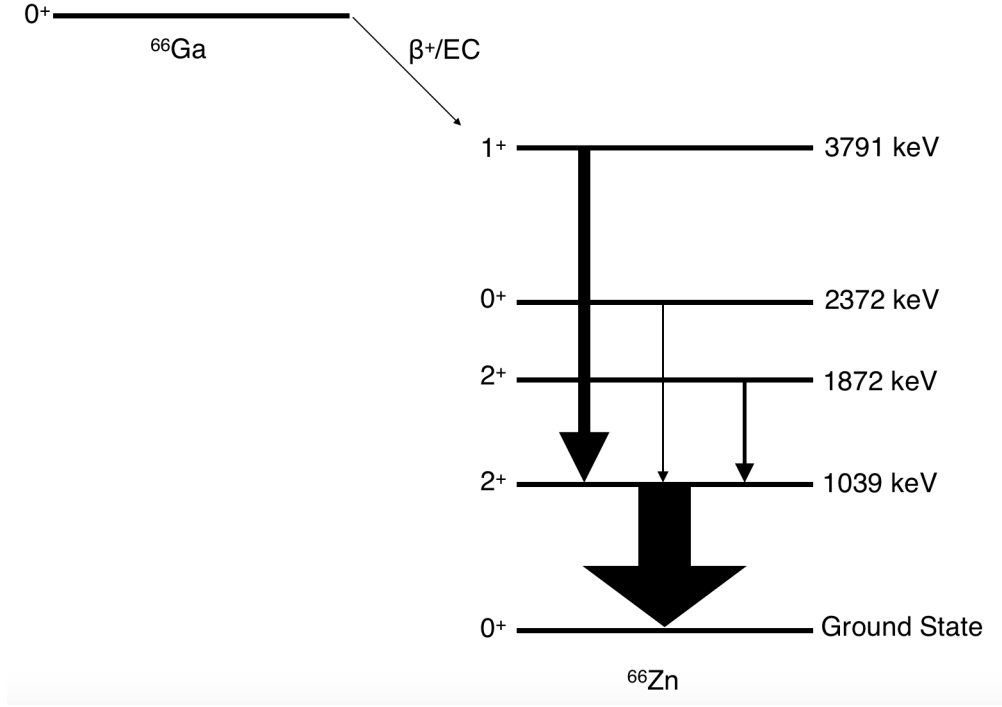


Figure 3.37: Image of levels studied in the decay of  $^{66}\text{Ga}$  to  $^{66}\text{Zn}$ . This is only a partial decay scheme highlighting the  $\gamma - \gamma$  angular correlations studied in this work.

$0^+ \rightarrow 2^+ \rightarrow 0^+$ . This is an important cascade, as it has a large anisotropy and is generally easily distinguishable from other correlations. The intensity of the 1333 *keV*  $\gamma$ -ray is reported to be 1.17(6)% [38] per  $\beta^+/\text{EC}$  decay. It feeds the 1039 *keV* state, which then decays to the ground state. With the 2372 *keV* state being a  $0^+$  state, there is no direct transition via  $\gamma$  decay to the ground state. The second cascade analyzed was the 833-1039 *keV* cascade, which is a known  $2^+ \rightarrow 2^+ \rightarrow 0^+$  having a mixing ratio reported to be  $\delta = -1.9(3)$  [44]. An intensity of 5.9(3)% is reported [38] for this transition, which then decays to 1039 *keV* level. Although there is a direct transition to the ground state, it is very weak, with an intensity of only 0.0229(19)% [38]. This cascade was used to test the measurements of a known mixing ratio with GRIFFIN. The final correlation studied was the 2752-1039 *keV* cascade, being a  $1^+ \rightarrow 2^+ \rightarrow 0^+$  cascade, the measurement of the mixing ratio

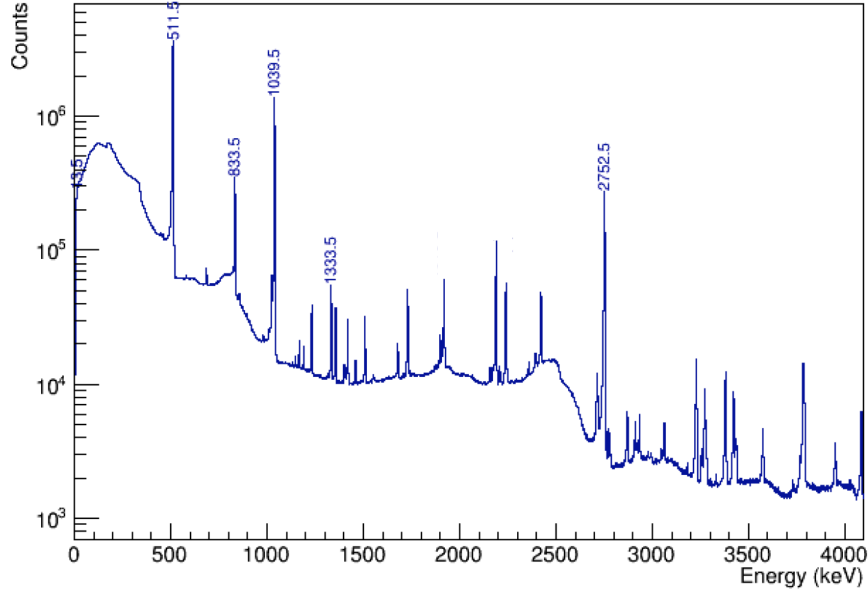


Figure 3.38:  $\gamma$ -ray spectrum from  $^{66}\text{Ga}$  decay with peaks used in the angular correlation analysis labelled.

was completed without any previous knowledge of the reported value. With a large intensity of 22.7(12)% [38] per  $\beta^+$ /EC decay, there were ample statistics to measure this mixing ratio with GRIFFIN.

For the  $^{66}\text{Ga}$  data set there are many  $\gamma$ -rays in the spectrum, as seen in Figure 3.37. The nucleus decays to  $^{66}\text{Zn}$  via the emission of a  $\beta^+$  and electron capture. The  $\beta^+$  will annihilate and produce two 511 keV  $\gamma$ -rays producing a strong peak at 511 keV in Figure 3.38. Labelled in this spectrum are the  $\gamma$ -rays utilized in the angular correlation measurements, as well as the annihilation peak.

### 833-1039 keV Cascade

This cascade was intended to test mixing ratio measurements with GRIFFIN, having a known mixing ratio,  $\delta = -1.9(3)$  [44]. Following the procedure previously described, a

$\gamma - \gamma$  matrix was made for each opening angle in the GRIFFIN geometry. An example, for  $\theta = 60.15^\circ$ , is shown in Figure 3.39. In Figure 3.40, the spectrum is shown with a gate on the 833 keV  $\gamma$ -ray. Again, this is quite a busy spectra, compared to  $^{60}\text{Co}$ , giving many other  $\gamma$ -rays in coincidence over a large energy range.

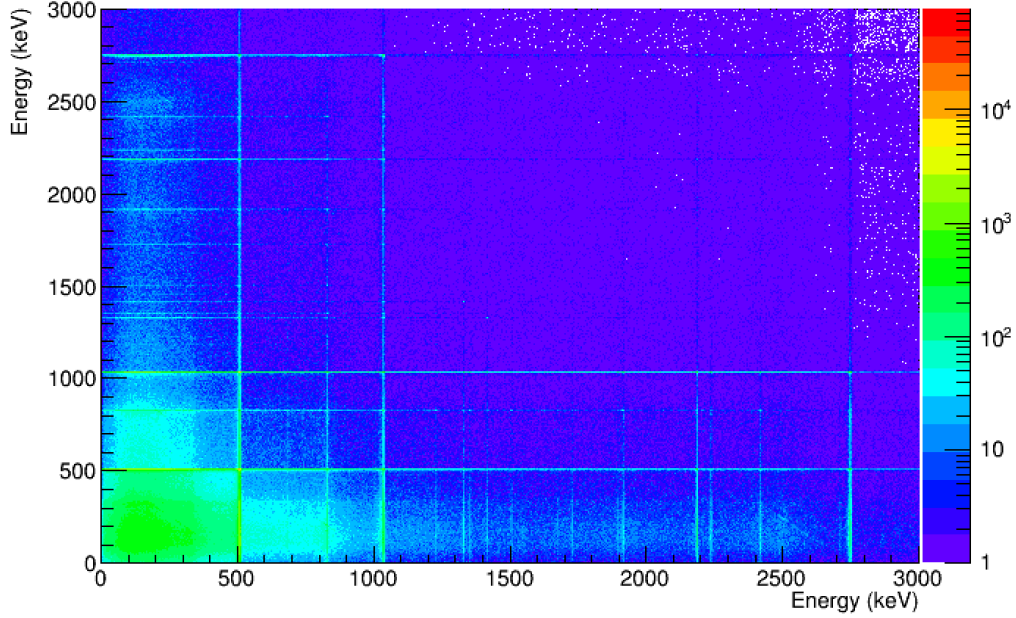


Figure 3.39:  $\gamma - \gamma$  matrix for  $^{66}\text{Ga}$  decay with the two  $\gamma$ -rays detected in GRIFFIN detectors separated by  $\theta = 60.15^\circ$ .

Once all background subtractions and corrections were made, the angular correlations were extracted, as shown in Figure 3.41. The best fitting template is shown here with a mixing ratio of  $-2.1$  producing a  $\chi^2/\nu = 0.85$ . By comparing the data to other Geant4 templates, centralized around the range of the previously reported mixing ratio, a  $\chi^2/\nu$  versus  $\text{atan}(\delta)$  was produced to determine the uncertainty of the mixing ratio. From Figure 3.42, the value for the mixing ratio obtained with GRIFFIN is  $\delta = -2.1(2)$ , assuming the sign convention of Steffen and Krane [17]. This agrees with the previously reported measurement, with slightly improved precision provided by the GRIFFIN data.

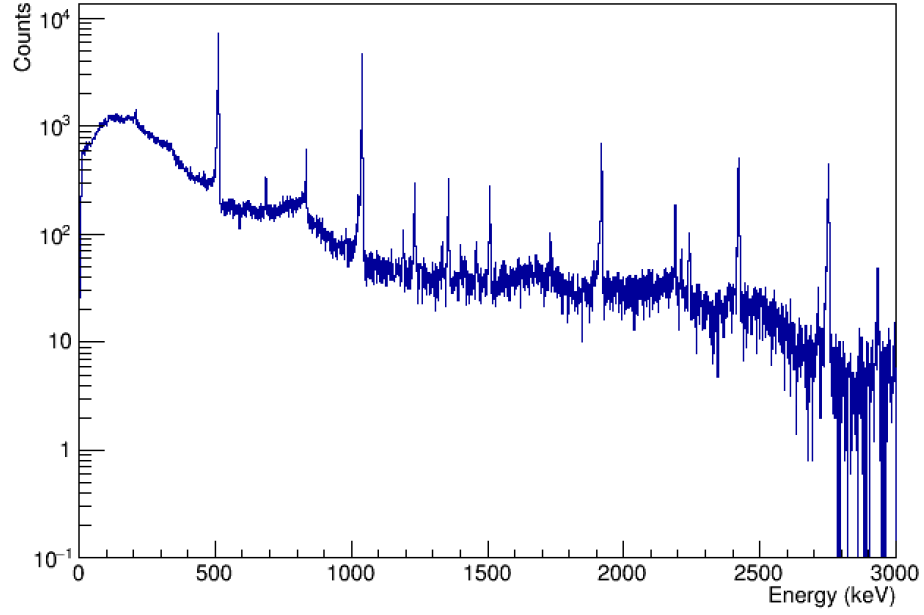


Figure 3.40: Projection of the  $^{66}\text{Ga}$   $\gamma - \gamma$  matrix gated on the 833  $\text{keV}$  photopeak.

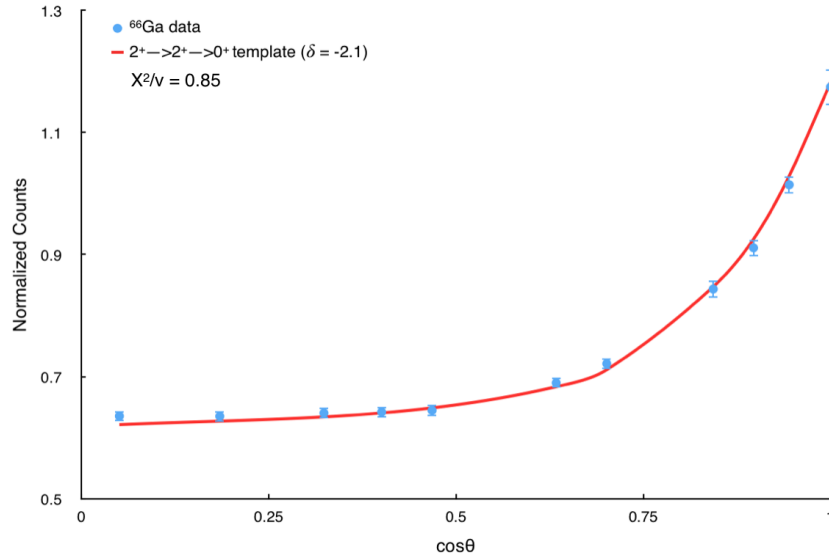


Figure 3.41: Angular correlation measured for the 833-1039  $\text{keV}$   $\gamma - \gamma$  cascade in  $^{66}\text{Ga}$  decay.

### 1333-1039 $\text{keV}$ Cascade

The next cascade was the  $0^+ \rightarrow 2^+ \rightarrow 0^+$  cascade involving the 1333-1039  $\text{keV}$   $\gamma$ -rays. The coincident  $\gamma - \gamma$  matrix was projected with a gate on the 1333  $\text{keV}$  photopeak, as shown in



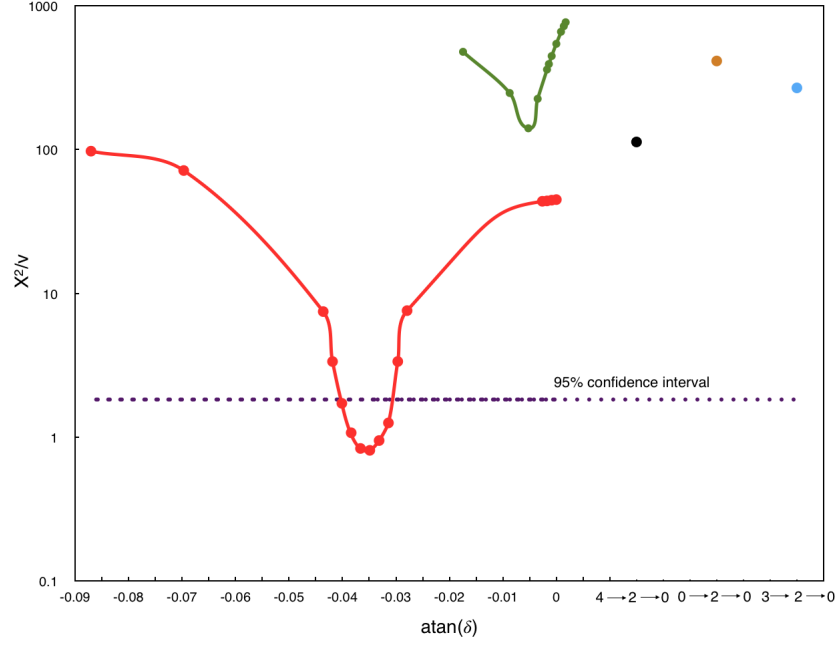


Figure 3.42:  $\chi^2/\nu$  for the data in Figure 3.41 compared with Geant4 generated templates. The  $2^+ \rightarrow 2^+ \rightarrow 0^+$  (red) and  $1^+ \rightarrow 2^+ \rightarrow 0^+$  (green) comparisons are performed over a range of mixing ratios,  $\delta$ .

Figure 3.43.

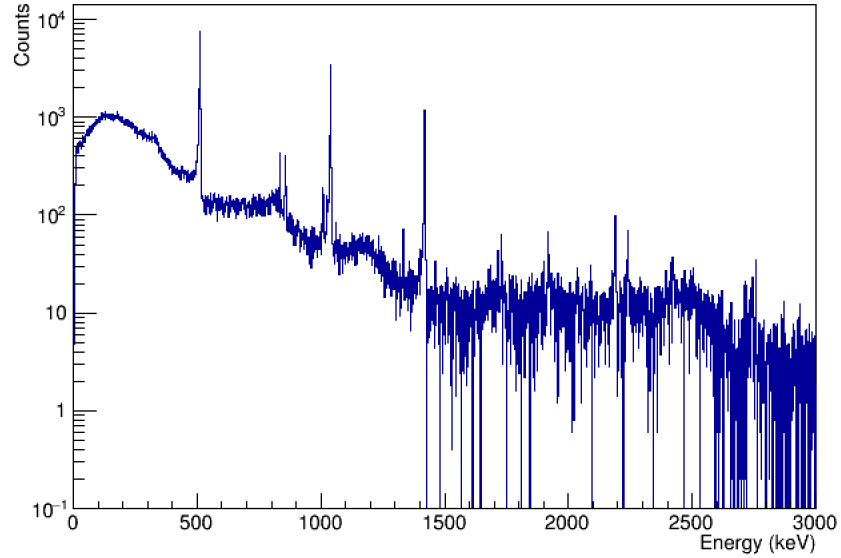


Figure 3.43: Projection of the  $^{66}\text{Ga}$   $\gamma - \gamma$  matrix gated on the 1333 keV photopeak.

The 1039 *keV*  $\gamma$ -ray was then fit for each opening angle after time-random events were subtracted and a Compton background spectrum generated using a gate just above the 1333 *keV* photopeak was subtracted. The angular correlation from mixed events was used to correct for crystal efficiency differences. The angular correlation is shown in Figure 3.44, and compared to a range of Geant4 templates. A  $\chi^2/\nu$  versus  $\text{atan}(\delta)$  plot confirms that this is a  $0^+ \rightarrow 2^+ \rightarrow 0^+$  cascade with  $\chi^2/\nu = 0.96$ . All other cascades of different spins and varying mixing ratio can be clearly eliminated as they produced  $\chi^2/\nu \geq 100$ . The ability

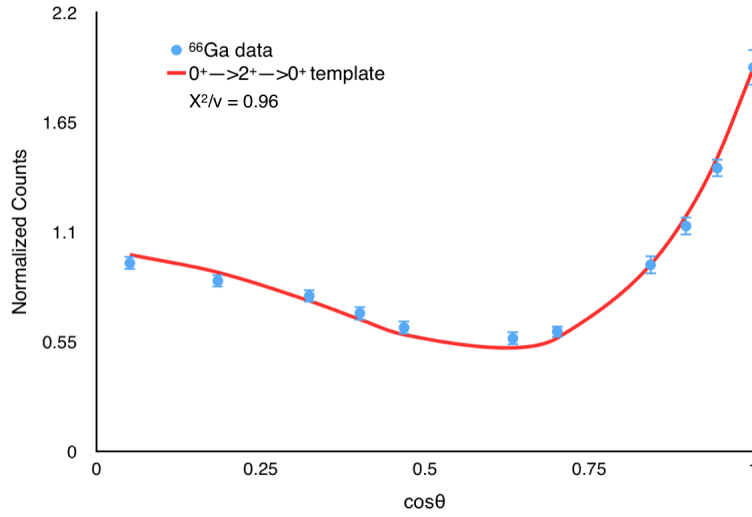


Figure 3.44:  $0^+ \rightarrow 2^+ \rightarrow 0^+$  cascade involving the 1333-1039 *keV* transitions in  $^{66}\text{Zn}$  compared with a Geant4 generated template.

to discern a  $0^+ \rightarrow 2^+ \rightarrow 0^+$  cascade is one of great importance that will be seen later in this thesis. Also, it being one of the most pronounced angular correlations, it serves as a baseline requirement for discerning nuclear spins.

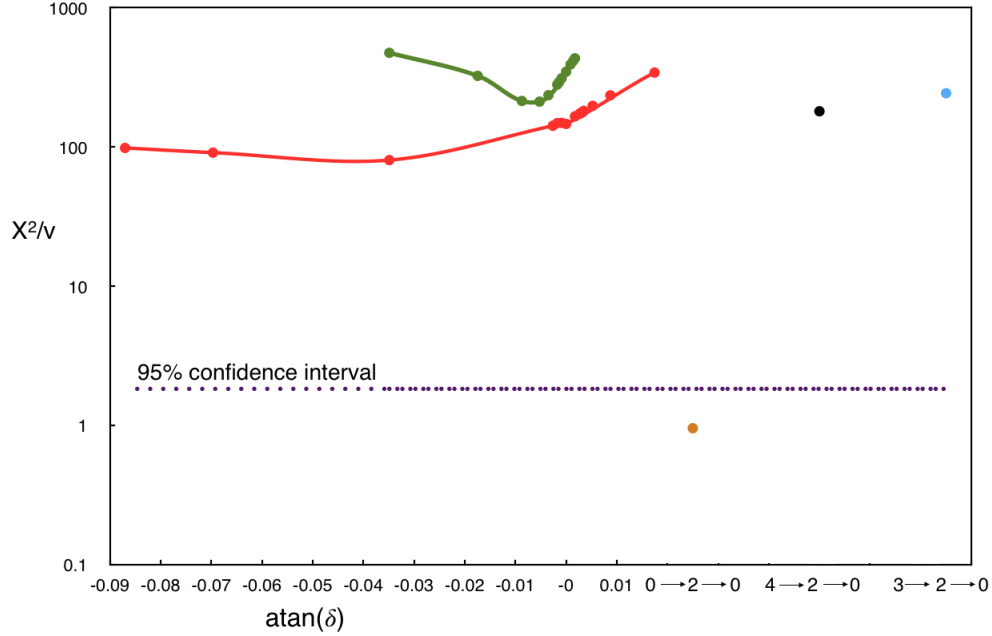


Figure 3.45:  $\chi^2/\nu$  versus  $\text{atan}(\delta)$  for the 1333-1039  $keV$  cascade, with the  $2^+ \rightarrow 2^+ \rightarrow 0^+$  (red) and the  $1^+ \rightarrow 2^+ \rightarrow 0^+$  (green) being tested for a range of mixing ratios. This cascade is definitively confirmed as a  $0^+ \rightarrow 2^+ \rightarrow 0^+$

### 2752-1039 $keV$ Cascade

The final test with  $^{66}\text{Ga}$  was to determine a mixing ratio for the 2752-1039  $keV$  cascade. In Figure 3.50, the projection of the  $\gamma - \gamma$  matrix is seen with a gate on the 2752  $keV$  photopeak. The peaks were fit and the angular correlation extracted as shown in Figure 3.48.

In order to define a range of mixing ratios to examine in the Geant4 simulations, theoretical values were investigated. Using a wide range of mixing ratios, a broad set of theoretical  $a_2$  and  $a_4$  coefficients were calculated that encompassed the correlation characteristics similar to the one seen experimentally. It was determined that the mixing ratio, under the assumption of accepted spins [45] giving a  $1^+ \rightarrow 2^+ \rightarrow 0^+$  cascade, was  $\delta = -0.08(3)$  with  $\chi^2/\nu = 0.92$ .

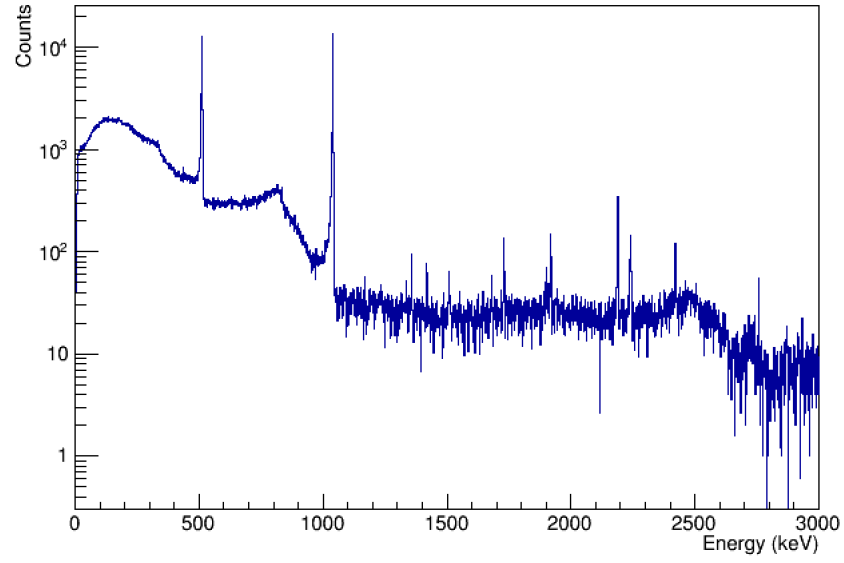


Figure 3.46: Projection of the  $^{66}\text{Ga}$   $\gamma - \gamma$  matrix gated on the 2752  $\text{keV}$  photopeak.

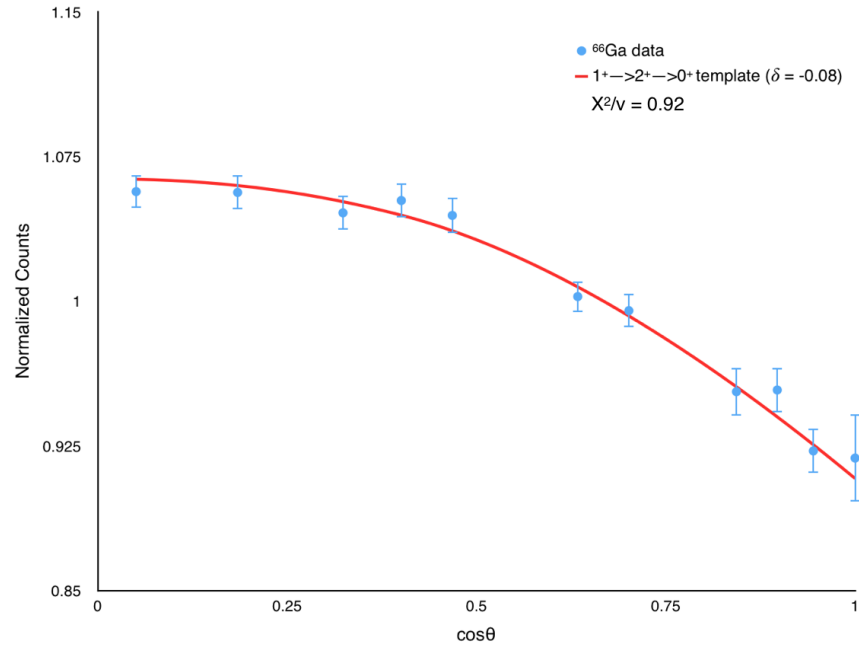


Figure 3.47: Plot of the angular correlation for the 2752-1039  $\text{keV}$  cascade fit with a Geant4 template (red) with  $\delta = -0.08$ .

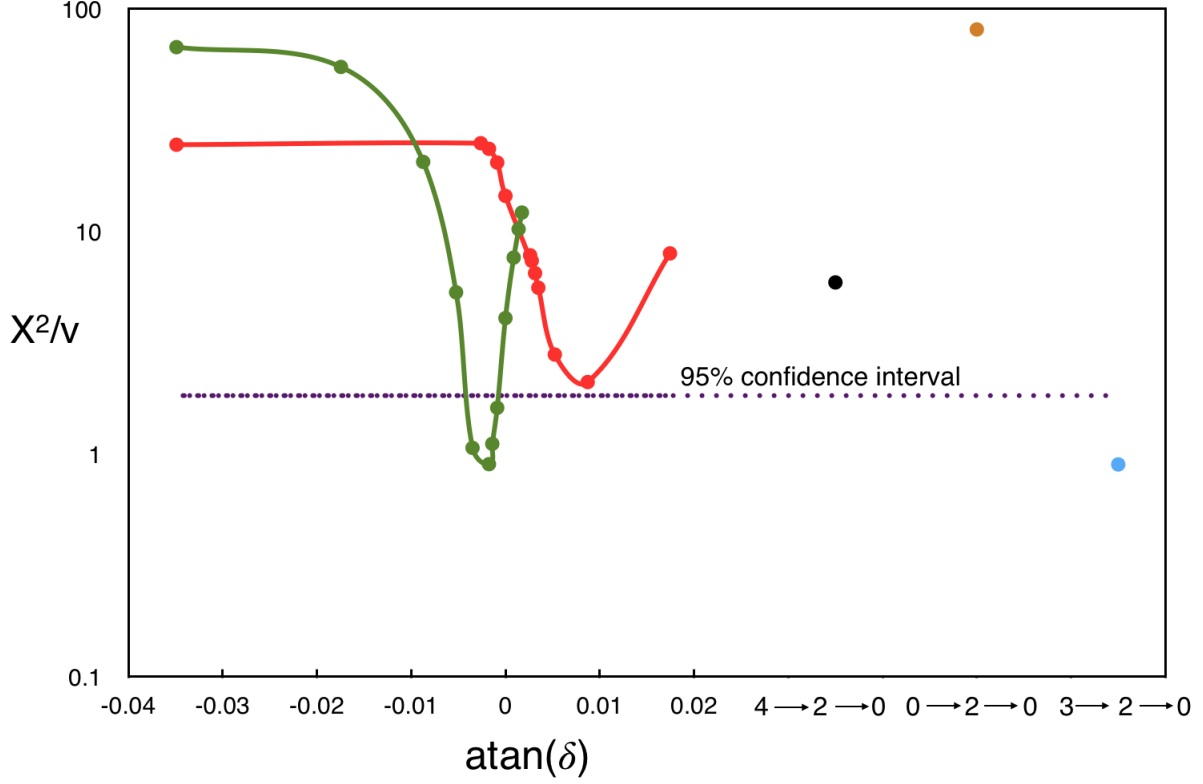


Figure 3.48: Plot of  $\chi^2/\nu$  vs  $\text{atan}(\delta)$  for the  $1^+ \rightarrow 2^+ \rightarrow 0^+$  (green), and the  $2^+ \rightarrow 2^+ \rightarrow 0^+$  (red), being evaluated for a range of mixing ratios.

Unfortunately, this angular correlation has another that is very similar in shape causing a degeneracy. A  $3^+ \rightarrow 2^+ \rightarrow 0^+$  cascade with  $\delta = 0$  also agrees with the data, yielding  $\chi^2/\nu = 0.92$ . It is expected that there is a range of possible  $\delta$  values for a  $3^+ \rightarrow 2^+ \rightarrow 0^+$  that would match this correlation as there is a possibility of E2/M1 mixing with this cascade also. Templates for the  $3^+ \rightarrow 2^+ \rightarrow 0^+$  utilizing different mixing ratios have not been generated but would be interesting to investigate as the overlap between these cascades is significant as shown in Figure 1.11. If this is indeed a  $1^+ \rightarrow 2^+ \rightarrow 0^+$  cascade, then it is expected that there would be a direct M1 transition from the 3791 *keV* level to the ground state. This would not be the case for a  $3^+ \rightarrow 2^+ \rightarrow 0^+$  cascade where direct M3 decay to the ground

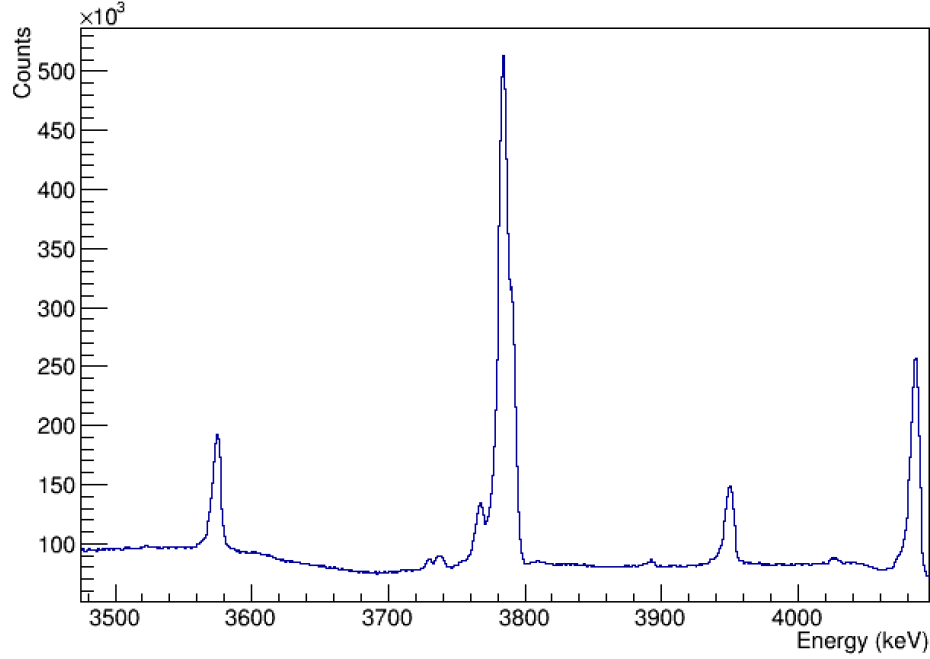


Figure 3.49:  $\gamma$ -ray spectrum from  $^{66}\text{Ga}$  decay showing the direct transition from the 3791  $keV$  level to the ground state.

state would not be expected to compete with the 2752  $keV$  M1/E2 due to the extra angular momentum needed to be carried by the  $\gamma$ -ray.

The 3791  $keV$  peak is seen quite clearly in Figure 3.49, with  $(4821 \pm 3) \times 10^3$  counts in the photopeak. Even though some of these may be from a sum peak, the angular correlations are symmetric about  $90^\circ$  so the sum peak counts should be equal to the area of the coincidence peak in the detectors separated by  $180^\circ$ . In the  $180^\circ$  coincidence peak there are approximately 60,000 counts, which represents only 1.2% of the counts in the 3791  $keV$  photopeak. These considerations allow for a definite assignment of the 2752-1039  $keV$  cascade as a  $1^+ \rightarrow 2^+ \rightarrow 0^+$  cascade with  $\delta = -0.08(3)$ . The similarity of the  $1^+ \rightarrow 2^+ \rightarrow 0^+$  and  $3^+ \rightarrow 2^+ \rightarrow 0^+$  cascades does, however, bring forth the issue of distinguishing cascades that

both have mixing ratios. In this case, the polarization of the  $\gamma$ -rays may not be enough to discern them, and other methods may be necessary, such as the observation or non-observation of cross-over transitions as discussed above.

With these measurements completed, many of the capabilities of GRIFFIN have been demonstrated for angular correlations. The final step was to test GRIFFIN by measuring an unknown or challenged spin assignment. This is discussed in the following section on  $^{62}\text{Ga}$  decay.

### 3.2.4 $^{62}\text{Ga}$ Data

$^{62}\text{Ga}$  is a nucleus of special importance as it is a superallowed Fermi  $\beta$  emitter. This means that it has a dominant  $\beta$  decay transition from its  $0^+$  ground state to the  $0^+$  isobaric analogue state of  $^{62}\text{Zn}$ . This is important because high-precision measurements of the  $ft$  values for such decays are used to validate the Conserved Vector Current (CVC) hypothesis, and provide the most precise value for the  $V_{ud}$  element of the Cabibbo-Kobayashi-Maskawa (CKM) quark mixing matrix [27, 46–49]. An  $ft$  value is comprised of the phase space integral,  $f$ , requiring precise Q-value measurements, and also the partial half-life,  $t$ , which is dependent on the half-life,  $t_{1/2}$ , the branching ratio and the probability of electron capture. In this thesis, there will not be much detail describing superallowed Fermi  $\beta$  emitters, but what is important to this discussion is a correction factor applied to the  $ft$  values.  $ft$  values for all superallowed  $\beta$  decays between states with isospin  $T = 1$  should in general be constant. This is almost true, with there being around a 2% variance for nuclei between  $^{10}\text{C}$  and  $^{74}\text{Rb}$ . These require corrections to the  $ft$  value as follows [50]:

$$\mathcal{F}t = ft(1 + \delta_R)(1 - \delta_C) = \frac{2\pi^3 \hbar^7 \ln(2)}{2G_v m_e^5 c^4 (1 + \Delta_R)} \quad (3.7)$$

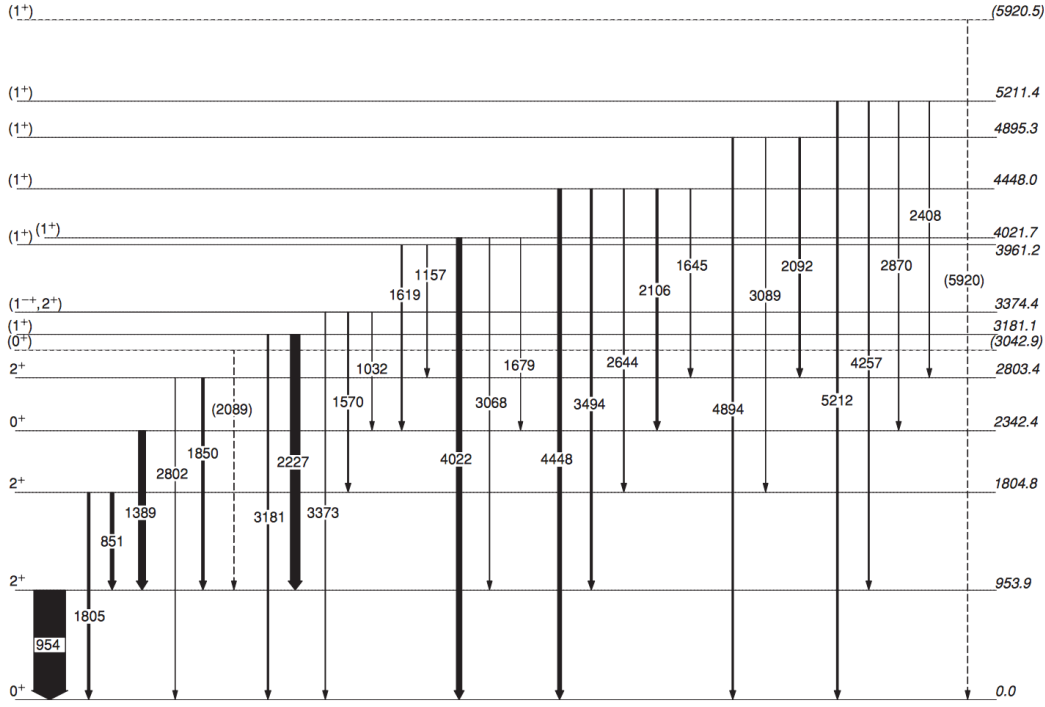


Figure 3.50: Level scheme of  $^{62}\text{Zn}$  populated by the  $\beta$  decay of  $^{62}\text{Ga}$ . The thickness of the lines correspond to the relative intensities of the  $\gamma$ -rays. Dashed lines are tentative transitions [51].

with  $\delta_R$  being a transition-dependent radiative correction,  $\Delta_R$  a transition-independent radiative correction, and  $\delta_C$  a nucleus-dependent isospin-symmetry-breaking (ISB) correction. The correction factor relevant to this work is the ISB correction,  $\delta_C$ . It can be further broken up into portions related to configuration mixing,  $\delta_{C1}$ , and imperfect radial overlap between the initial and final spatial nuclear wave functions,  $\delta_{C2}$  [52]. The configuration mixing, and hence the value of  $\delta_{C1}$ , is sensitive to the spectrum of  $0^+$  excited states in  $^{62}\text{Zn}$ .

Recently, the spin of what had previously been assigned as the first excited  $0^+$  state in  $^{62}\text{Zn}$  has been called into question. The first excited  $0^+$  state was previously reported at 2.34 MeV from a study of angular correlations in the  $^{61}\text{Ni}(^3\text{He}, 2n\gamma)$  reaction at the



Cologne Tandem accelerator with the HORUS spectrometer [53]. Another study, using a  $^{64}\text{Zn}(\text{p},\text{t})^{62}\text{Zn}$  reaction with the Q3D magnetic spectrograph at the Technical University of Munich assigned the 2.34 *MeV* state as  $2^+$  [52]. The consequences of the labelling of this state produces a factor of two difference in the ISB correction  $\delta_{C1}$  for  $^{62}\text{Ga}$  superallowed decay.

To attempt to resolve the discrepancy in the spin assignment for the 2342 *keV* excited state of  $^{62}\text{Zn}$ , an experiment was preformed at TRIUMF using a zirconium-carbide (ZrC) target paired with the TRIUMF Resonant Ionization Laser Ion Source (TRILIS) [54]. A beam rate of 8000  $^{62}\text{Ga}$  ions per second was expected, as was obtained in previous experiments with this nucleus [51]. However, due to issues with an extraction electrode, as well as transmission losses, the beam rate observed was an average of only 1250 ions per second, a reduction by a factor of 6.4. Even with the lower beam rate, in comparison to a previous  $^{62}\text{Ga}$  experiment with the  $8\pi$  spectrometer [51], the efficiency of GRIFFIN allowed for a measurement to be attempted. In Figure 3.51, a comparison is made between the GRIFFIN data set and the data set collected with the  $8\pi$  spectrometer. The  $8\pi$  data set had a beam rate of  $\sim 8000$  ions/s and a total of  $6 \times 10^8$  detected events, while the GRIFFIN experiment recorded approximately half that number at  $3 \times 10^8$  events.

Due to the lower than expected beam rate in this experiment, it was run with clover addback mode in order to maximize the number of counts in the photopeak. During the experiment, 1077(36) coincidence events between the 954 *keV* photopeak and the 1388 *keV* were observed, which is populated in only 0.0191% of the  $^{62}\text{Ga}$   $\beta$  decays [38]. This was preformed by using  $\beta - \gamma - \gamma$  coincidences with the tagging of the  $\beta$  particle with SCEPTAR [33], which was running at an efficiency of 74(5)%. With the  $\beta - \gamma - \gamma$  coincidences, the room background is strongly suppressed and a cleaner spectrum is produced. In Figure

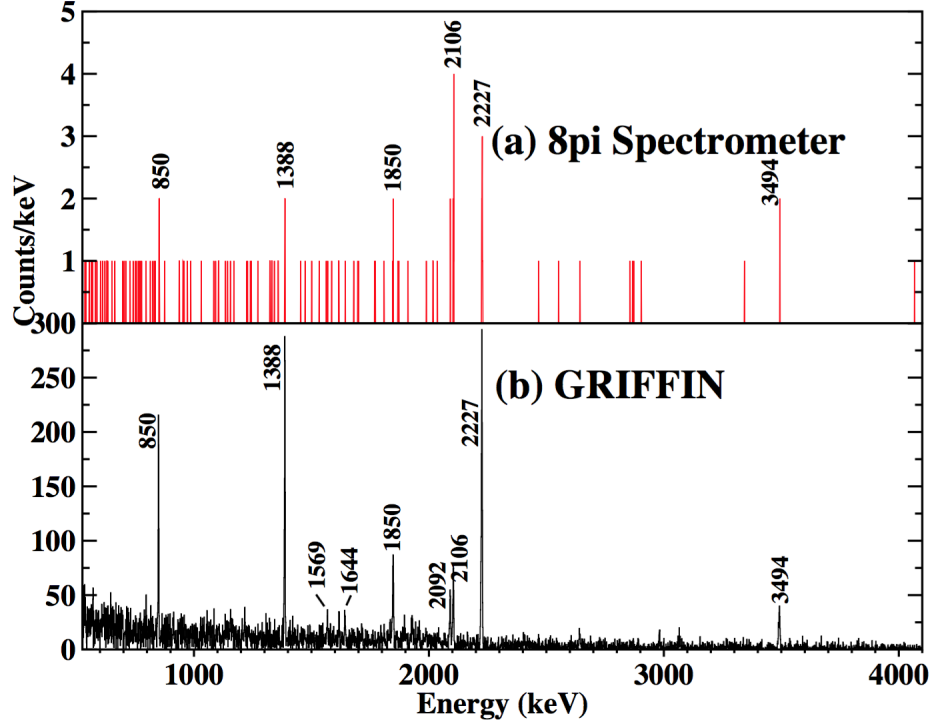


Figure 3.51: Comparison of  $^{62}\text{Ga}$  spectra collected with the  $8\pi$  (top) and GRIFFIN (bottom). In each case a coincidence gate has been placed on the  $954\text{ keV}$   $\gamma$  ray.

3.52, the  $\beta - \gamma$  spectrum is shown and in the top right corner of this image is the projection of the  $\beta - \gamma - \gamma$  spectrum showing the  $954\text{ keV}$  photopeak with a gate set on the  $1388\text{ keV}$   $\gamma$ -ray.

One clue that could assist in the determination of whether the  $2.34\text{ MeV}$  state should be assigned as  $2^+$  or a  $0^+$  is the possibility of a  $\gamma$ -ray transition to the ground state at  $2.34\text{ MeV}$ . If this is a  $2^+$  state, there could be a measurable direct transition to the ground state, but if it is a  $0^+$  state, then no  $\gamma$ -ray should be seen at this energy. The method for searching was as follows:

- Find a peak close to  $2.34\text{ MeV}$  and use TPeak in order to determine the FWHM expected.

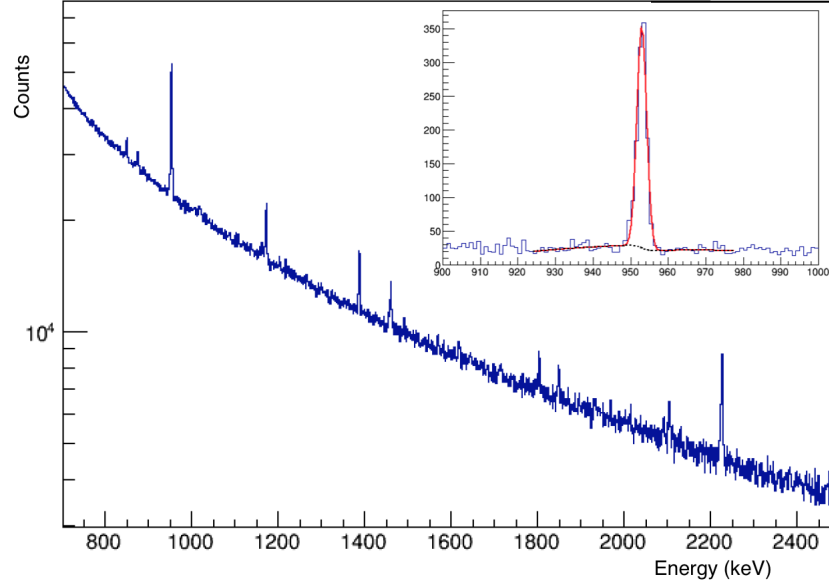


Figure 3.52:  $\beta - \gamma$  spectrum for  $^{62}\text{Ga}$  with the top right image being a projection of the  $\beta - \gamma - \gamma$  coincidence spectrum gated on the 1388  $\text{keV}$   $\gamma$ -ray.

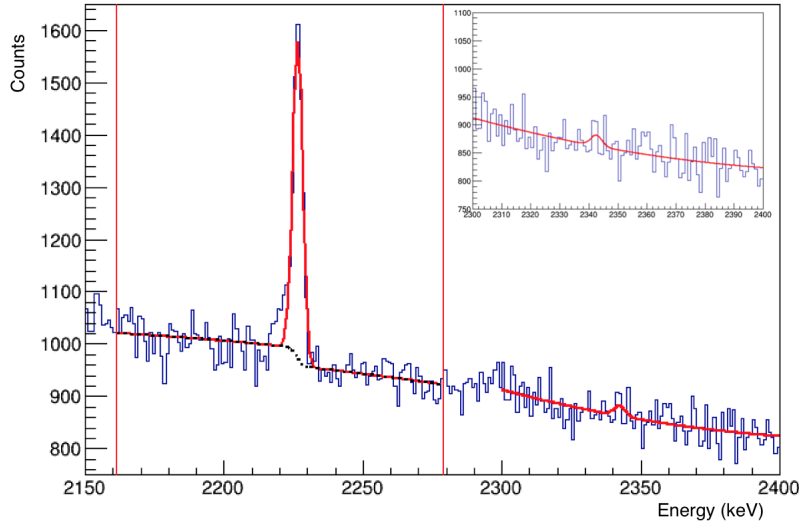


Figure 3.53: Peak fit at 2342.2  $\text{keV}$  with the neighbouring peak, at 2226.2  $\text{keV}$ , used for the determination of the FWHM.

- Fix the centroid to the known  $\gamma$ -ray energy and use the FWHM from the previous fit.

- Once fit, check the integrated counts to see if they are consistent with zero.

An issue with this method is that the spectrum may not be perfectly gain matched at this energy, as there are not many peaks to gain match on. When fitting the larger peak in figure 3.53, the centroid was found to be at  $2226.2 \text{ keV}$ , while the centroid from the National Nuclear Data Centre is quoted at  $2227.2 \text{ keV}$  [38]. Due to this offset, in the search for the  $2342 \text{ keV}$   $\gamma$ -ray, the centroid was varied by  $\pm 2 \text{ keV}$ . The results can be seen in Table 3.3. Although some fits give counts which are above zero at the  $1.1\sigma$  level, this does not give any clear evidence for the existence of a direct  $2342 \text{ keV}$  transition to the ground state.

Centroid	Counts
2340.2	212(193)
2341.2	94(98)
2342.2	97(96)
2343.2	261(289)
2344.2	414(372)

Table 3.3: Limit on counts in the  $2342 \text{ keV}$  transition in  $^{62}\text{Ga}$  as a function of the assumed centroid position.

The angular correlation measurement was studied using all 51 opening angle combinations, grouping angles and folding about ninety degrees. With the low statistics, it is seen that there is quite a large relative uncertainty on each of the data points in Figure 3.54. Using addback, and without a sum peak, there are 49 unique angle pairs. After grouping, there are 20 angular bins. The angular correlation for the grouped angles is shown in Figure 3.55. Finally, the data is folded about ninety degrees and yields 11 angles, as shown in Figure 3.56. All of these are compared with a  $0^+ \rightarrow 2^+ \rightarrow 0^+$  cascade as well as a  $2^+ \rightarrow 2^+ \rightarrow 0^+$  cascade with a mixing ratio of  $\delta = -2$ . A range of mixing ratios was used for the  $2^+ \rightarrow 2^+ \rightarrow 0^+$  to see the comparison between the data and the  $2^+ \rightarrow 2^+ \rightarrow 0^+$  cascade.

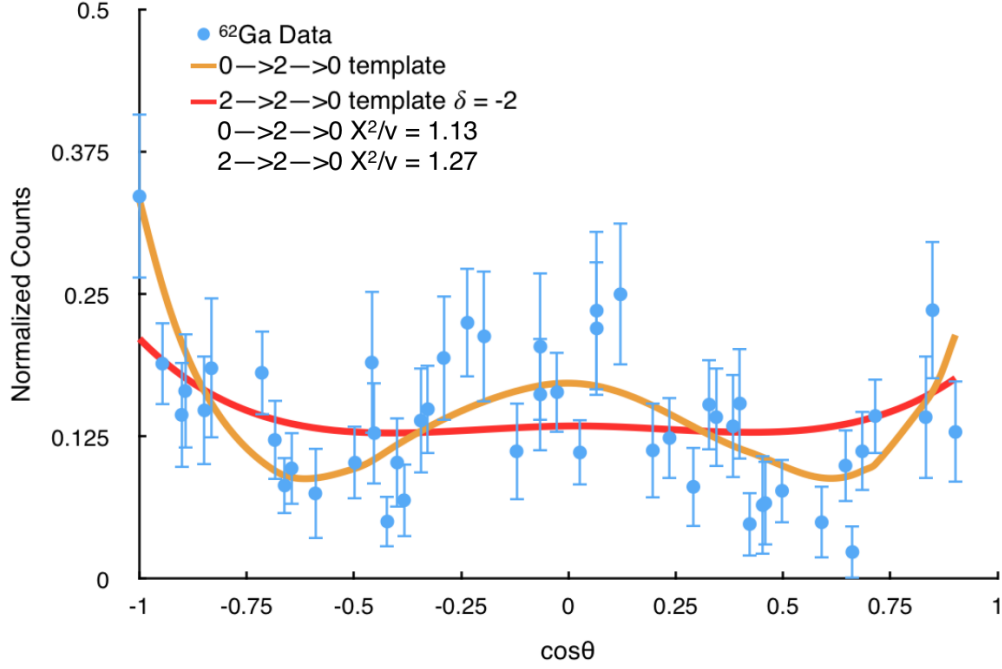


Figure 3.54: Angular correlation using all angles for the 1388-954 *keV* cascade in  $^{62}\text{Ga}$  fit with a  $0^+ \rightarrow 2^+ \rightarrow 0^+$  (orange) and a  $2^+ \rightarrow 2^+ \rightarrow 0^+$  template with a  $\delta = -2$  (red).

With the range of templates, a  $\chi^2/\nu$  versus  $\arctan(\delta)$  plot was made for these comparisons for each of the angular correlation plots including all angles, grouped angles, and grouped and folded. These are shown in Figure 3.57, 3.58 and 3.59 respectively. By keeping more angles and not grouping or folding the data, there are more degrees of freedom when considering the  $\chi^2/\nu$ . The  $\chi^2/\nu$  for these plots do vary, however. In figure 3.57, the  $\chi^2/\nu$  for the  $0^+ \rightarrow 2^+ \rightarrow 0^+$  template is 1.13, and the minimum for a  $2^+ \rightarrow 2^+ \rightarrow 0^+$  cascade is 1.27. After grouping the data, the  $\chi^2/\nu$  value for the  $0^+ \rightarrow 2^+ \rightarrow 0^+$  cascade is 0.81 and for the  $2^+ \rightarrow 2^+ \rightarrow 0^+$  the minimum is 1.13. Finally, for the grouped and folded data, the  $\chi^2/\nu$  for the  $0^+ \rightarrow 2^+ \rightarrow 0^+$  template is 0.75, while for the  $2^+ \rightarrow 2^+ \rightarrow 0^+$  the minimum is 1.10.

The shape is consistent with that seen in Figure 3.45 for a  $0^+ \rightarrow 2^+ \rightarrow 0^+$ , but because of the limited statistics in this experiment, the relative errors are too large to definitively

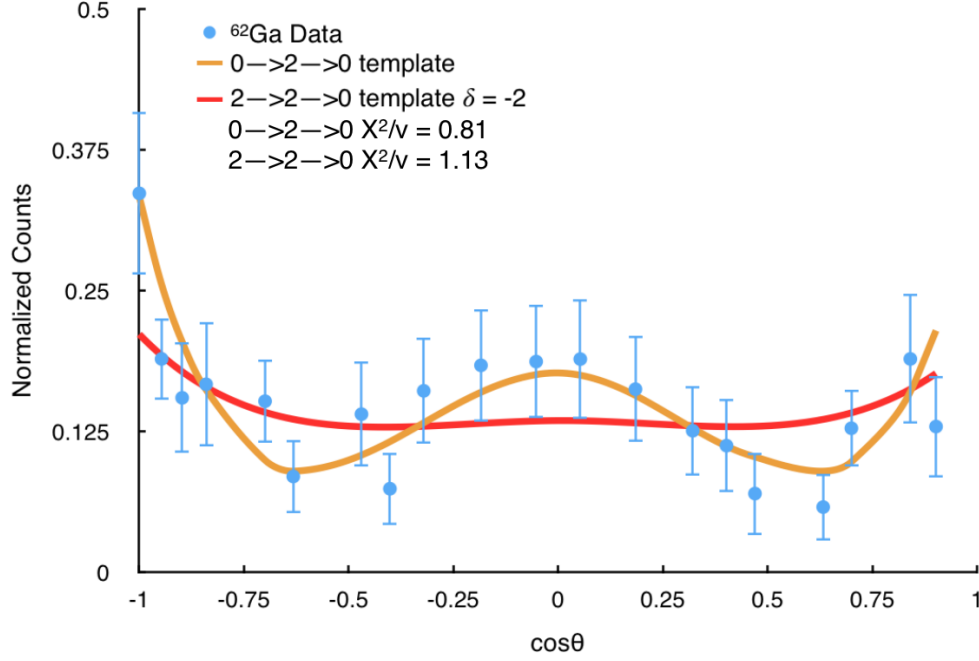


Figure 3.55: Angular correlation for the 1388-954 *keV* cascade in  $^{62}\text{Ga}$  with angles grouped and fit with a  $0^+ \rightarrow 2^+ \rightarrow 0^+$  (orange) and a  $2^+ \rightarrow 2^+ \rightarrow 0^+$  template with a  $\delta = -2$  (red).

distinguish between the two possible spin assignments. In the case where all angles are considered a mixing ratio of  $\delta \leq -1$  was accepted. This is only an upper limit as the values converge for large negative values of mixing ratios. Mixing ratios up to  $\delta = -10$  were simulated in this work. In the case of grouping the angles, the accepted mixing ratio range is found to be  $\delta \leq -0.25$  and for the case of grouping and folding the angles the range is  $\delta \leq -0.1$ .

In order to estimate a beam rate, or the number of events needed to successfully complete this experiment, Geant4 simulations were run comparing  $0^+ \rightarrow 2^+ \rightarrow 0^+$  cascade simulations of different number of events to the templates. Only comparisons between the  $0^+ \rightarrow 2^+ \rightarrow 0^+$  and  $2^+ \rightarrow 2^+ \rightarrow 0^+$  template with a mixing ratio of  $\delta = -2$  were studied.

From these simulations, it is determined that a minimum of  $3 \times 10^5$  simulated events are

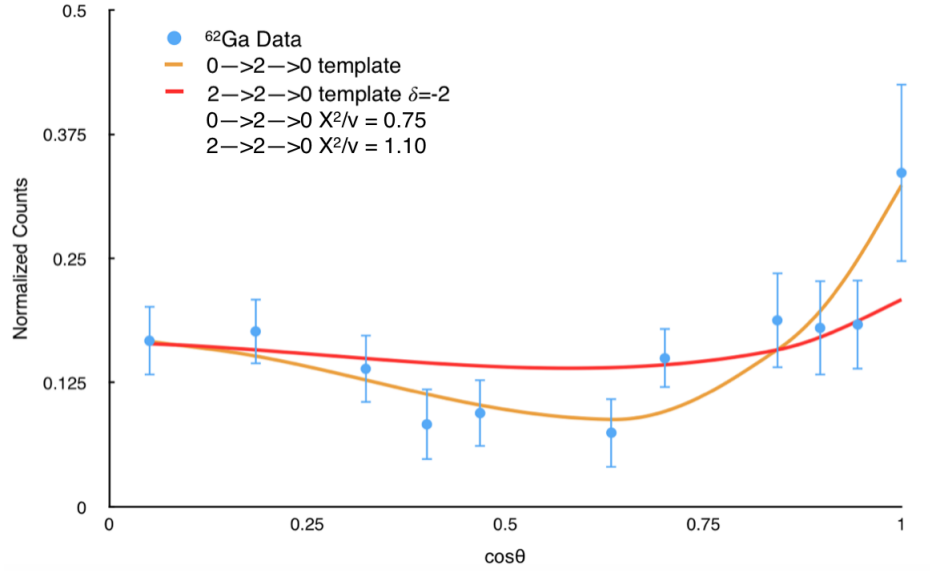


Figure 3.56: Angular correlation for the 1388-954  $keV$  cascade in  $^{62}\text{Ga}$  fit with a  $0^+ \rightarrow 2^+ \rightarrow 0^+$  (orange) and a  $2^+ \rightarrow 2^+ \rightarrow 0^+$  template with a  $\delta = -2$  (red).

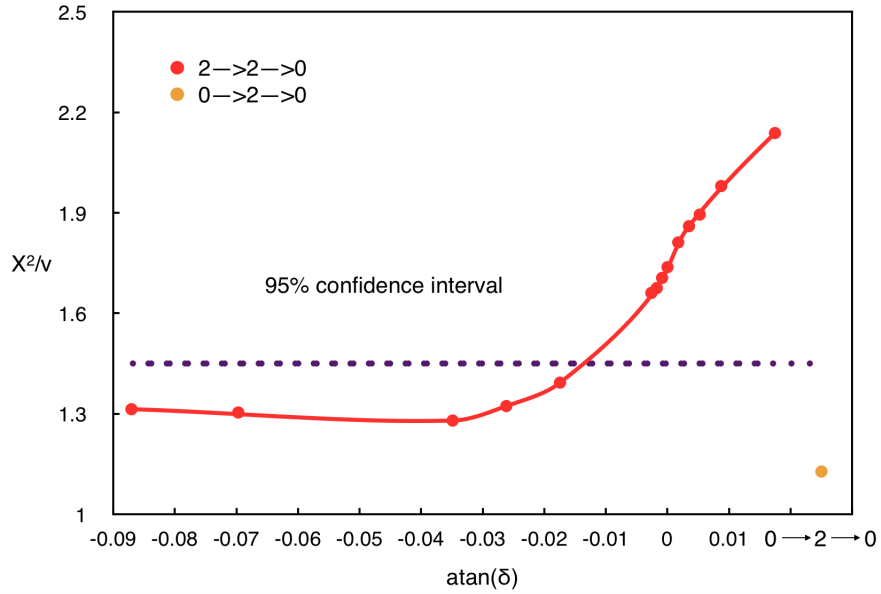


Figure 3.57:  $\chi^2/\nu$  vs  $\text{atan}(\delta)$  with the  $0^+ \rightarrow 2^+ \rightarrow 0^+$  (orange) and a  $2^+ \rightarrow 2^+ \rightarrow 0^+$  with the range of templates (red) using all angles in GRIFFIN.

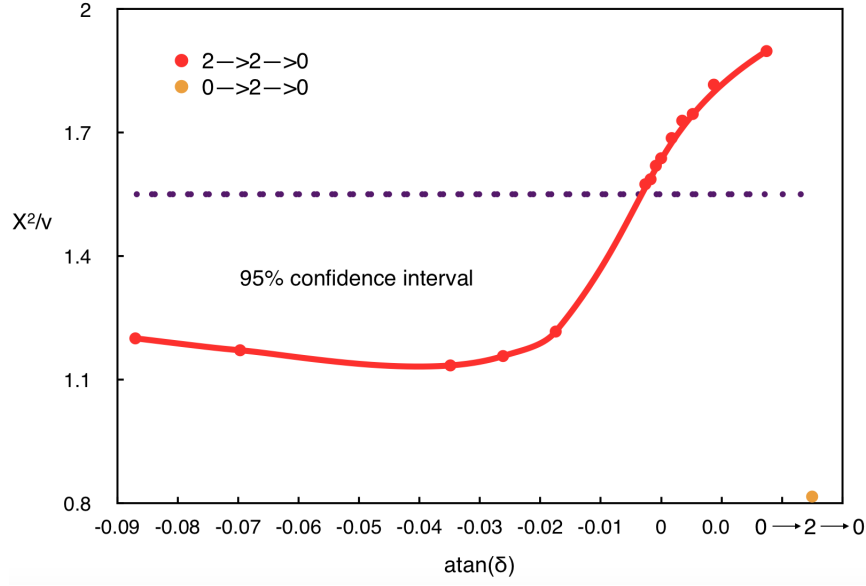


Figure 3.58:  $\chi^2/\nu$  vs  $\text{atan}(\delta)$  with the  $0^+ \rightarrow 2^+ \rightarrow 0^+$  (orange) and a  $2^+ \rightarrow 2^+ \rightarrow 0^+$  with the range of templates (red) after grouping similar angles in GRIFFIN.

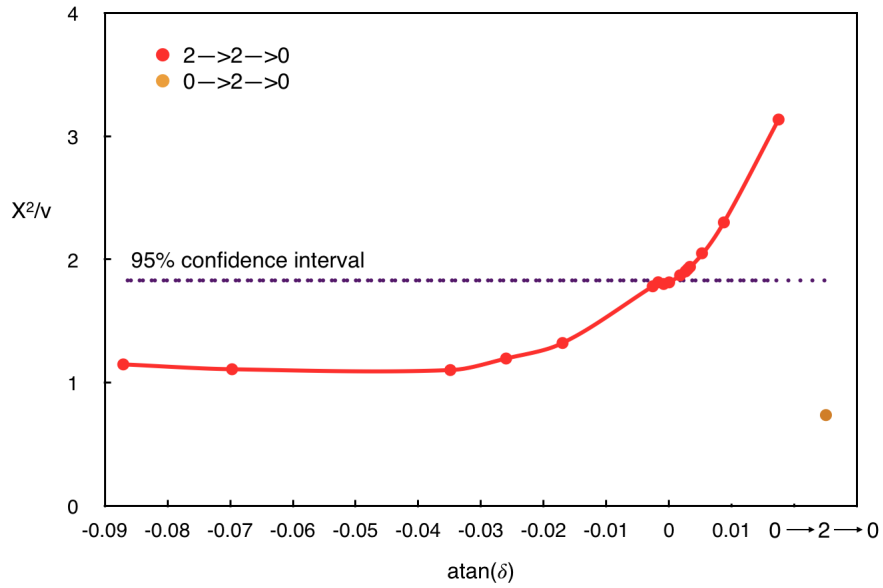


Figure 3.59:  $\chi^2/\nu$  vs  $\text{atan}(\delta)$  with the  $0^+ \rightarrow 2^+ \rightarrow 0^+$  (orange) and a  $2^+ \rightarrow 2^+ \rightarrow 0^+$  with the range of templates (red) after both grouping and folding angles in GRIFFIN.



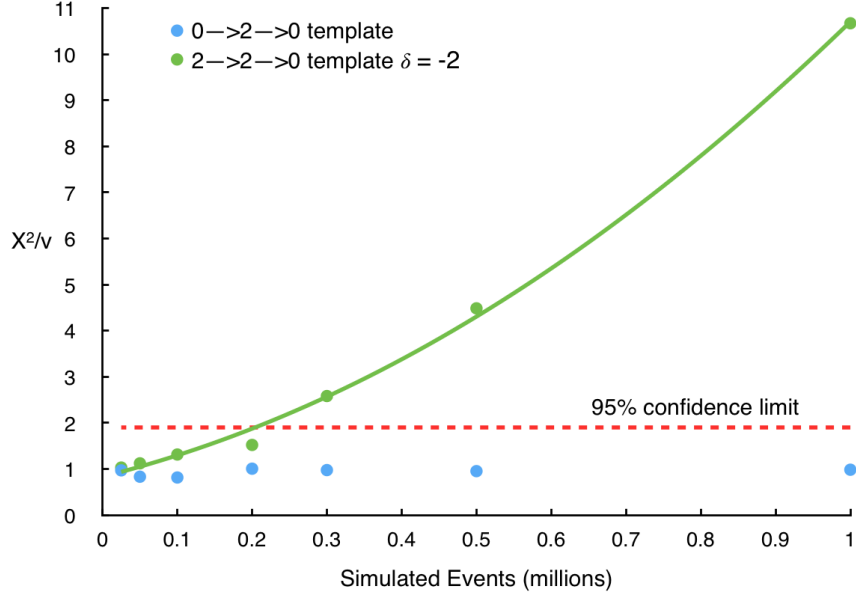


Figure 3.60:  $\chi^2/\nu$  for a  $0^+ \rightarrow 2^+ \rightarrow 0^+$  cascade for different numbers of simulated events, compared to a  $2^+ \rightarrow 2^+ \rightarrow 0^+$  with  $\delta = -2$  after both grouping and folding angles in GRIF-FIN.

needed to go through this cascade in order to distinguish between the  $0^+ \rightarrow 2^+ \rightarrow 0^+$  and  $2^+ \rightarrow 2^+ \rightarrow 0^+$  cascade at a 95% confidence level. Note that these are simulated events not detected events and the analysis assumes that the efficiency is approximately the same between simulation and experiment. The total number of  $\beta$  decays that must be detected is given by:

$$A_{total} = \frac{E_{cascade}}{I \times C}. \quad (3.8)$$

Here  $A_{total}$  is the total number of detected  $\beta$  decays needed for the experiment,  $E_{cascade}$  is the number of events passing through the cascade of interest and  $I$  is the branching ratio to the level 0.0191% [38]. Finally,  $C$  is a correction for both  $\gamma$ -rays being detected in the same clover, equivalent to 15/16 for the number of clovers. From Figure 3.60, the limit of events

through this cascade is seen to be between  $2\text{--}3 \times 10^5$ . Using  $3 \times 10^5$  events, the total number of detected  $\beta$  decays required is  $1.67 \times 10^9$ . With the total time used for this experiment, twelve shifts or six days, a beam-on duty factor of  $\approx 90\%$  and a  $\beta$  detection efficiency of  $\approx 75\%$  this leads to a beam rate of  $\approx 5000/\text{s}$  or a factor of almost 4 more than measured in this experiment. This rate should be achievable as this  $^{62}\text{Ga}$  beam intensity has been delivered in previous experiments.

# Chapter 4

## Conclusions

Two high-statistic measurements were performed to establish a methodology to classify spins of nuclear excited states through  $\gamma - \gamma$  angular correlation measurements with the new GRIFFIN  $\gamma$ -ray spectrometer at TRIUMF. The first measurements used a  $^{60}\text{Co}$  source which undergoes a  $\beta^-$  decay to  $^{60}\text{Ni}$ . This  $\beta^-$  decay is followed by a  $4^+ \rightarrow 2^+ \rightarrow 0^+$   $\gamma - \gamma$  cascade involving 1.17 and 1.33 *MeV*  $\gamma$ -rays. The second nuclear decay studied was the  $^{66}\text{Ga}$   $\beta^+/\text{EC}$  decay to  $^{66}\text{Zn}$ . In this decay three  $\gamma - \gamma$  cascades were studied. The first is a 833-1039 *keV* cascade which is a known  $2^+ \rightarrow 2^+ \rightarrow 0^+$  cascade having a previously reported mixing ratio of  $\delta = -1.9(3)$ . The second cascade was the 1333-1039 *keV* cascade which is a known  $0^+ \rightarrow 2^+ \rightarrow 0^+$ . The final measurement was for a 2752-1039 *keV* cascade in  $^{66}\text{Zn}$  which is a known  $1^+ \rightarrow 2^+ \rightarrow 0^+$  cascade, but with no previously mixing ratio.

These two data sets provided ample statistics to test the sensitivity of the GRIFFIN spectrometer to  $\gamma - \gamma$  angular correlations. With GRIFFIN, the ability to measure the spins of the nuclear excited states was confirmed and the measured  $\gamma - \gamma$  angular correlations were consistent with all previously known spin assignments. In some cases, as in the  $4^+ \rightarrow 2^+ \rightarrow 0^+$

cascade in  $^{60}\text{Co}$  decay, additional methods would be needed to definitively assign spins as the angular correlation is effectively indistinguishable for a  $2^+ \rightarrow 2^+ \rightarrow 0^+$  cascade with a particular mixing ratio of  $\delta = 0.18(1)$ . For the  $2^+ \rightarrow 2^+ \rightarrow 0^+$  cascade involving the 833-1039  $keV$   $\gamma$  rays in  $^{66}\text{Zn}$  a mixing ratio of  $\delta = -2.1(2)$  was measured, in complete agreement with, and slightly more precise than, the previously reported value of  $\delta = -1.9(3)$  [44]. The  $1^+ \rightarrow 2^+ \rightarrow 0^+$  cascade for the 2752-1039  $keV$   $\gamma$  rays in  $^{66}\text{Zn}$  was measured to have a mixing ratio of  $\delta = -0.08(3)$ . Here the observation of the direct transition from the 3791  $keV$  state to the  $0^+$  ground state confirmed the  $1^+ \rightarrow 2^+ \rightarrow 0^+$  cascade and eliminated the possibility of  $3^+ \rightarrow 2^+ \rightarrow 0^+$ , which was also consistent with angular correlation. Due to the angular momentum transferred in a  $3^+ \rightarrow 0^+$  M3 transition, this transition would not have been observed with a  $3^+$  assignment to the 3791  $keV$  state. For the 1333-1039  $keV$  cascade in  $^{66}\text{Zn}$  the known spin sequence of  $0^+ \rightarrow 2^+ \rightarrow 0^+$  was definitively confirmed, with all other spins eliminated due to the  $\chi^2/\nu \geq 100$  for the measured angular correlation.

The third measurement was an initial attempt to determine a recently challenged spin assignment in the decay of the superallowed  $\beta^+$  decay of  $^{62}\text{Ga}$  to  $^{62}\text{Zn}$  [52]. The implications of the spin assignment for this excited state, located at 2.34  $MeV$ , changes the isospin symmetry breaking correction for  $^{62}\text{Ga}$  superallowed decay by a factor of 2. While our angular correlation measurements with GRIFFIN were fully consistent with, and favoured the previous spin assignment of  $0^+$  for the 2.34  $MeV$  state in  $^{62}\text{Zn}$  [53], unfortunately the reduction in the expected beam rate, due to a faulty extraction electrode for this experiment did not provide the statistics required for a definitive spin assignment to this state. From the measured angular correlations, a limit was set on the mixing ratios if this state was a  $2^+ \rightarrow 2^+ \rightarrow 0^+$  cascade. With all 51 opening angles in the GRIFFIN geometry the limit of the mixing ratio was found to be  $\delta \leq -1$  at a 95% confidence interval, after grouping angles the

mixing ratio was  $\delta \leq -0.25$  at 95% confidence and after grouping and folding the data the limits was  $\delta \leq -0.1$  at 95% confidence. With the use of Geant4 an estimation was made for the minimum beam rate, or number of events, necessary to definitively assign a spin to this state. It was established that a factor of 4 increase, from 1250 ions per second to  $\approx 5000$  ions per second over 12 shifts (6 days), would be required for the measurement. This increase is entirely feasible as rates of 5000 ions per second has been produced for  $^{62}\text{Ga}$  in previous experiments at the ISAC facility [51].

The use of  $\gamma-\gamma$  angular correlation measurements provides a powerful means to elucidate the structure of nuclei. By establishing a methodology for angular correlation measurements, and investigating the sensitivity of the GRIFFIN spectrometer to such measurements, future experiments with GRIFFIN will assign unknown spins and parities of excited nuclear states. This will allow for the advancement of nuclear structure studies and the refinement of theoretical models.

## 4.1 Future Work

Future work to be preformed includes the investigation of using GRIFFIN's clover detectors as Compton polarimeters to measure the polarization of the  $\gamma$  rays. This would require the use of the full polarization-dependent Klein-Nishina equation to be implemented in the radioactive decay module in Geant4, allowing for polarization simulations to be run for decaying nuclei. The difference in the scattering direction of Compton scattered  $\gamma$  rays, either perpendicular or parallel to the direction of polarization, allows one to investigate the electric and magnetic characteristics. In the case of  $^{60}\text{Co}$  decay this is important as a  $4^+ \rightarrow 2^+ \rightarrow 0^+$  cascade has pure E2 transitions while this  $2^+ \rightarrow 2^+ \rightarrow 0^+$  cascade that gives

an effective indistinguishable angular correlation has  $\delta = 1.8(1)$  and thus involves a mixed E2/M1 transition. This could be one way of discerning the differences in this cascade [55].

Experimental data from the  $\beta^+$  decay of  $^{62}\text{Ga}$  was recorded. Although the primary reason for this was the angular correlation measurement relevant to the assignment of the 2.34 *MeV* excited state, a full analysis of these data will be completed. With the efficiency of the GRIFFIN spectrometer the data collected has two orders of magnitude more statistics in  $\gamma - \gamma$  coincidences than the previous experiment performed with the  $8\pi$  spectrometer. A complete analysis could also be performed on the  $^{66}\text{Ga}$  source data as this was a very high statistic measurement and numerous other angular correlations could be measured in this decay.

# Bibliography

- [1] C. E. Svensson, *Collectivity in  $A \approx 60$  Nuclei: Superdeformed and Smoothly Terminating Rotational Bands*, Ph.D. Thesis, McMaster University (1998).
- [2] K. Krane, *Modern Physics*, 3<sup>rd</sup> ed. (John Wiley & Sons, 1996).
- [3] R. D. Woods and D. S. Saxon, Phys.Rev. **95**, 557 (1954).
- [4] R. F. Casten and B. M. Sherrill, Progress in Particle and Nuclear Physics **45**, S171 (2000).
- [5] K. Heyde, *Basic Ideas and Concepts in Nuclear Physics*, 3<sup>rd</sup> ed. (Institute of Physics Publishing, 2004).
- [6] K. S. Krane, *Introductory Nuclear Physics*, 3<sup>rd</sup> ed. (John Wiley & Sons, 1987).
- [7] W. G. V. Rosser, *An Alternative to Maxwell's Equations Classical Electromagnetism Via Relativity*, 1<sup>st</sup> ed. (Butterworth & Co. Ltd., 1968).
- [8] P. J. Mohr, *Solutions of the Maxwell Equations and Photon Wavefunctions*.
- [9] J. M. Blatt and V. F. Weisskopf, *Theoretical Nuclear Physics*, 4<sup>th</sup> ed. (John Wiley & Sons, 1991).

- [10] G. Goertzel, Angular Correlation of Gamma-Rays **70** (1946).
- [11] T. Yamazaki, Table of Coefficients for Angular Distribution of Gamma Rays From Aligned Nuclei (1967).
- [12] H. J. Rose and B. D. M., Angular Distributions of Gamma Rays in Terms of Phase-Defined Reduced Matrix Elements (1967).
- [13] H. Frauenfelder and S. R. M., *Alpha-, Beta-, and Gamma-Ray Spectroscopy*, 5<sup>th</sup> ed. (North-Holland Publishing Company, 1979).
- [14] E. L. Brady and M. Deutsch, Angular Correlation of Successive Gamma-Rays **78** (1950).
- [15] D. Williams, *Methods of Experimental Physics* (Academic Press Inc., 1976).
- [16] A. Messiah, *Quantum Mechanics*, 2<sup>nd</sup> ed. (Dover Publications, Inc., 1995).
- [17] K. S. Krane, R. M. Steffen, and R. M. Wheeler, Nuclear Data Tables **11**, 351 (1973).
- [18] N. Pietralla *et al.*, Spin and Parity Assignments to Dipole Excitations of the Odd-Mass Nucleus  $^{207}\text{Pb}$  from Nuclear Resonance Fluorescence Experiments with Linearly-Polarized  $\gamma$ -ray Beams **205** (2010).
- [19] E. T. Rand, *Geant4 Simulations For The Radon Electric Dipole Moment Search At TRIUMF*, Master's Thesis, University of Guelph (2011).
- [20] S. J. Robinson, Nuclear Instruments and Methods **A292**, 386 (1990).
- [21] N. Pietralla *et al.*, *ANGULAR CORRELATIONS OF PROMPT GAMMA-RAYS FROM THE SPONTANEOUS FISSION OF  $^{252}\text{Cf}$* , Ph.D. Thesis, Vanderbilt University (2008).



- [22] A. Aquili, R. Cesareo, and M. Giannini, Gamma-Ray Transitions and Gamma-Gamma Angular Correlations in  $^{152}\text{Sm}$  **LXII** (1968).
- [23] R. Avida *et al.*, Nuclear Instruments and Methods **46**, 350 (1966).
- [24] “TRIUMF History,” <http://www.triumf.ca/home/about-triumf/history>.
- [25] “TRIUMF Research Facilities,” <http://www.triumf.ca/research-program/research-facilities/isac-facilities>.
- [26] A. Perez-Andujar and L. Pibida, Elsevier **60**, 41 (2003).
- [27] R. Dunlop, *High-Precision Branching-Ratio Measurement for the Superalloyed  $\beta^+$  Emitter  $^{74}\text{Rb}$* , Master’s Thesis, University of Guelph (2012).
- [28] R. D. Evans, The Atomic Nucleus (1982).
- [29] G. F. Knoll, *Radiation Detection and Measurement*, 4<sup>th</sup> ed. (John Wiley & Sons, 2010).
- [30] C. E. Svensson and A. B. Garnsworthy, Hyperfine Interactions **225**, 127 (2014).
- [31] A. B. Garnsworthy and P. E. Garrett, Hyperfine Interactions **225**, 121 (2014).
- [32] C. E. Svensson *et al.*, Nucl. Instrum. Methods Phys. Res. B **204**, 660 (2003).
- [33] G. C. Ball *et al.*, J. Phys. G **31**, S1491 (2005).
- [34] P. E. Garrett, Hyperfine Interactions **225**, 137 (2014).
- [35] G. Hackman and C. E. Svensson, Hyper. Int **225**, 241 (2014).
- [36] S. Agostinelli *et al.*, Nuclear Instruments and Methods **A** (2003).

- [37] E. T. Rand, <https://github.com/GRIFFINCollaboration/Geant4GammaGammaAngularCorrelations10.01.p01> (2014).
- [38] A. Sonzogni, <http://www.nndc.bnl.gov/chart> (1977).
- [39] P. C. Bender, R. D. Dunlop, V. Bildstein, J. K. Smith, and D. Miller, <https://github.com/GRIFFINCollaboration/GRSISort>, (2013).
- [40] B. Jigmeddorj, *Nuclear Structure Study of Cd-110 through Internal Conversion Electrons*, Master's Thesis, University of Guelph (2012).
- [41] G. Gilmore, *Practical Gamma-Ray Spectrometry*, 2<sup>nd</sup> ed. (John Wiley & Sons, 2008).
- [42] F. A. Souza *et al.*, Nuclear Instruments and Methods **612**, 196 (2009).
- [43] J. K. Smith, *Angular Correlations - Theoretical derivation of the Event-Mixing Technique*.
- [44] R. B. Firestone, *Table of Isotopes*, 8<sup>th</sup> ed. (John Wiley & Sons, 1996).
- [45] P. M. Endt and C. Alderliesten, Nuclear Physics A **575**, 297 (1993).
- [46] G. F. Grinyer, *High-Precision Half-Life Measurements for Superalloyed Fermi  $\beta$  Emitters*, Ph.D. Thesis, University of Guelph (2008).
- [47] P. E. J. Finlay, *High-Precision Half-Life and Branching-Ratio Measurements for the Superalloyed  $\beta^+$  Emitter  $^{26}\text{Al}^m$* , Ph.D. Thesis, University of Guelph (2012).
- [48] K. G. Leach, *High-Precision Measurement of the Superalloyed  $\beta$ -Decay Branching Ratio of  $^{38m}\text{K}$* , Ph.D. Thesis, University of Guelph (2008).

- [49] A. T. Laffoley, *High-Precision Half-Life Measurement for the Superaligned Fermi  $\beta$  Emitters  $^{14}\text{O}$  and  $^{18}\text{Ne}$* , Ph.D. Thesis, University of Guelph (2008).
- [50] I. S. Towner and J. C. Hardy, Rep. Prog. Phys. **73**, 046301 (2010).
- [51] P. Finlay *et al.*, Phys. Rev. C **78**, 025502 (2008).
- [52] K. G. Leach *et al.*, Phys. Rev. Lett. **96**, 032002 (2013).
- [53] M. Albers *et al.*, Nuc. Phys. **847**, 180 (2010).
- [54] <http://www.triumf.ca/rilis-laser-ion-source> (2013).
- [55] K. Starosta *et al.*, Nuclear Instruments and Methods **423**, 16 (1999).